ROYAL AIRCRAFT ESTABLISHMENT
BEDFORD

MINISTRY OF SUPPLY

AERONAUTICAL RESEARCH COUNCIL
REPORTS AND MEMORANDA

The Estimation of Shock Pressure Recovery and External Drag of Conical Centre-Body Intakes at Supersonic Speeds

By

E. L. GOLDSMITH and C. F. GRIGGS

The Estimation of Shock Pressure Recovery and External Drag of Conical Centre-Body Intakes at Supersonic Speeds

By

E. L. Goldsmith and C. F. Griggs

Communicated by the Director General of Scientific Research (Air)
Ministry of Supply

Summary.—Methods of predicting shock pressure recovery and external drag at all mass flows have been developed for conical centre-body intakes at supersonic speeds. Comparison with wind-tunnel measurements shows that the method for predicting the shock pressure recovery gives the correct variation for the shock losses as the shock configuration changes with mass-flow ratio. Agreement near full mass flow is not so good when the losses other than shock losses are probably changing rapidly and the shock configuration remains unchanged. Results of drag tests show that reasonable agreement with theory is obtained for the rise in drag which occurs when the intake is spilling and for the drag at full mass flow. Curves are included to assist in the calculation of the drag rise and the associated reduction in pressure recovery.

1. *Introduction.*—It has been shown[1,2] that conical centre-body air intakes fulfil the requirements of high recovery of free-stream total pressure and low external drag over a useful range of Mach number and mass flow.

In the interests of maximum propulsive efficiency it may be necessary to operate a long-range ram jet at its critical point (full mass flow, near maximum pressure recovery and minimum drag) over the whole of its flight range, in which case some variable-geometry arrangement will have to be used.

On the other hand, a fixed-geometry guided missile launched at a Mach number of $1 \cdot 4$ or $1 \cdot 6$ and having a maximum Mach number in the region of $2 \cdot 2$ at altitude may be required to operate initially at 80 to 90 per cent of full mass flow. Thus it is important to develop methods of estimating drag and pressure recovery under conditions of reduced mass flow.

Methods for estimating these two quantities are presented in this report and the results are compared with experimental values. Some of the results are taken from experimental work conducted in the Royal Aircraft Establishment 9 in. $\times$ 9 in. and the No. 4 $5\frac{1}{2}$ in. $\times$ $5\frac{1}{2}$ in. Supersonic Tunnels.

Charts have been added at the end of this note by means of which the methods of estimation of pressure recovery and drag can be reduced to simple semi-graphical processes.

2. *Estimation of Pressure Recovery.*—Typical pressure-recovery–mass-flow curves are shown in Fig. 2 for the two conditions (*a*) $\theta_l < \theta_w$ and (*b*) $\theta_l > \theta_w$. The notation is given fully at the end of the text and is illustrated in Fig. 1.

(a) $\theta_l < \theta_w$

At (A), as shown, part of the entering stream tube passes through the efficient two-shock system (conical shock followed by a ' second ' shock approximately normal to the cone surface) and part solely through the ' third ' nearly normal shock. The final pressure recovery at the entry to the combustion chamber is a mean value resulting from the mixing of the two streams. At point (B) the maximum pressure recovery is obtained before the full mass-flow condition is reached. In this state the position of the streamline separating the external and internal flows coincides with the position of the point of intersection of the three-shock system (i.e., $r_i = r_\infty$ (Fig. 60)) and all the mass flow is entering through the efficient two-shock system. On further reducing the back pressure, the critical point (C) is reached. At this point the mass flow has achieved its maximum value and the pressure recovery has dropped off slightly from its value at (B). This drop is presumably caused by the curving of the centre body that must occur inside the cowl for any practical design. Part of the second shock is then occurring at a higher Mach number and is therefore less efficient.

(b) $\theta_l > \theta_w$

For point (A) conditions are identical to case (a) just considered. In the region (B), r_i is still less than r_∞, and the pressure recovery continues to rise until, finally, the full mass-flow condition is reached at the critical point (C). The maximum pressure recovery in this condition will then be smaller than for case (a), as there is now less isentropic conical compression, the expansion of the flow inside the lip will probably have an adverse effect and there is shock-boundary-layer interaction both on the centre body and on the under surface of the cowl.

Thus in order to estimate the pressure-recovery-mass-flow curve we require to know:
    (i) the angle of the third shock to the free stream
    (ii) the variation of r_i with mass flow for $r_i \leqslant r_\infty$
    (iii) the position of the second shock along the centre body (this can be found approximately from condition (ii) when $r_i < r_\infty$)
    (iv) the mixing and internal and external boundary-layer losses associated with the internal flow.

At the intersection of three shocks with resultant subsonic flow the system is defined and the angle of the third shock can be found (see Appendix I). The variation of r_i with mass flow for $r_i < r_\infty$ has been derived by extending the work of W. E. Moeckel[3] for detached shocks as in Appendix II and the method of estimating the drop in pressure recovery from (B) to (C) is presented in Appendix III.

The residual losses (i.e., those other than the shock losses) are the subsonic diffusion losses. They result from the effects of skin friction and mixing in the subsonic diffuser and are probably considerably influenced by the shock-boundary-layer interaction on the cone surface just in front of the duct entry. These losses will vary with mass flow and with Reynolds number and no attempt has been made to calculate or measure them.

3. *The Estimation of External Drag.*— 3.1. *External Drag when Spilling.*—As is usual for intake work at the R.A.E., we define the external drag coefficient (excluding skin friction) at any mass flow as $C_{D\,\text{ext}} = C_{D\,\text{cowl}} + C_{D\,\text{pre-entry}}$.

Now since we know the position of the external shock system (Appendices II and III) relative to the inlet, it should be possible to sum the external pressures acting on the stream-tube boundary AC (some weighted mean between the static pressure at B and the stagnation pressure at C would have to be used for the portion BC (Fig. 1)) to give the pre-entry drag $C_{D\,\text{pre}}$. At the same time as $C_{D\,\text{pre}}$ is increasing the pressures acting on the external surface of the cowl are decreasing. It is, however, difficult to predict the decrease in $C_{D\,\text{cowl}}$ when spilling, because the subsonic flow at the lip rapidly expands to supersonic velocities, and separation regions followed by shocks on the cowl result.

2

We therefore apply the method developed for Pitot intakes[4]. This cannot be justified in the same way, but nevertheless the cases can be considered analogous. When $r_i > r_\infty$ we split the spillage drag into two parts. Along AB the external pressures can be summed from a knowledge of conical flow to obtain $C_{\text{pre 1}}$. For BC we take the drag due to spillage as the product of the projected area A_{BC} and the relative static pressure behind the 'second' shock. When $r_i < r_\infty$, $C_{D\,\text{pre 1}}$ is zero, and the spillage drag becomes the product of the 'spillage area' A_{AC} and the relative static pressure behind the 'third' shock, i.e., for $r_i > r_\infty$:

$$C_{D\,\text{ext}} = C_{D\,\text{cowl 0}} + \frac{\left(\dfrac{p_A + p_B}{2} - p_\infty\right)A_{AB}}{q_\infty A_{\max}} + \frac{(p_{w\,2} - p_\infty)A_{BC}}{q_\infty A_{\max}}$$

where $C_{D\,\text{cowl 0}}$ = cowl drag at full mass flow.

For $r < r_\infty$:

$$C_{D\,\text{ext}} = C_{D\,\text{cowl 0}} + \frac{(p_{w\,3} - p_\infty)A_{AC}}{q_\infty A_{\max}}.$$

This then gives a non-linear characteristic for the drag rise, the slope changing discontinuously at the mass flow where $r_i = r_\infty$.

3.2. *Cowl Drag at Full Mass Flow*.—There are two linear theories[5, 6] by which the drag at full mass flow of a Pitot intake (or what is equivalent, a centre-body intake with the nose shock inside the cowl lip) can be calculated. One is a slender-body theory (which assumes the radius of the cowl at any point to be small compared with the overall length) and the other is a quasi-cylinder theory (which assumes the radius to be nearly constant). Neither theory is strictly applicable to the models used here but it has been shown[7] that results from the two theories agree remarkably well for bodies which are neither particularly slender nor good approximations to cylinders. The method used here has been to calculate the pressure coefficient at points on the cowl by quasi-cylinder theory and then to integrate them numerically. In Appendix IV the details of this process are given extended to the case when the cone shock is outside the cowl lip so that it can no longer be treated exactly as a simple Pitot.

3.3. *Lip Drag*.—In addition to the cowl and pre-entry drag at full mass flow there is probably an appreciable lip drag owing to the finite thickness of the rim of the model cowls. This is illustrated in Fig. 3 which shows the drag for a lip radius of 0·0053 in. ($r_{\text{lip}}/r_{en} = 0\cdot0053$) calculated from the results of a limited experimental investigation by Fraenkel[8] of the lip drag of Pitot intakes.

The use of Fraenkel's empirical relationship (derived from tests at Mach numbers of 1·4 and 1·8) at Mach numbers up to 3·3 probably requires further experimental justification.

3.4. *Pre-Entry Drag at Full Mass Flow*.—Pre-entry drag can be calculated exactly by use of the conical flow tables of Ref. 9. This has been done for a range of cone and lip position angles and the collected results are given in Ref. 10.

4. *Models*.—The experimental work was planned with two main objectives:

(a) To collect pressure-recovery and drag data from models having variations of cone angle θ_c, lip-position angle θ_l and cowl shape, so as to obtain comparisons between experimental and predicted results over as wide a range of conditions as possible.

(b) To obtain drag data for models which have realistic values for the ratio $A_{\text{entry}}/A_{\text{combustion chamber}}$. This entails the use of a rather larger tunnel than has hitherto

3

been used for intake work ($5\frac{1}{2}$ in. $\times$ $5\frac{1}{2}$ in.). Some drag tests have been done therefore in the R.A.E. 9 in. $\times$ 9 in. Supersonic Tunnel over the Mach number range 1·5 to 1·9.

It is convenient to discuss the models under the headings of the two tunnels in which they were tested.

4.1. $5\frac{1}{2}$ *in.* $\times$ $5\frac{1}{2}$ *in. Tunnel Models.*—Variations of cowl shape and lip-position angle have been investigated by testing models ST0, ST3, ST4, SD2, SD3 and SD6 (Figs. 4a and 4b). The first three models have the same cone angle ($\theta_c = 30$ deg) and cowl, and have lip-position angles such as the cone shock falls on the cowl rim ($\theta_w = \theta_l$) at Mach numbers of 2·08, 2·35 and 2·90 respectively. The three curved cowl models also have the same cone angle ($\theta_c = 30$ deg) and have the cone shock on the rim at Mach numbers of 2·35 (SD2), 1·86 (SD3) and 2·9 (SD6). It is desirable that the second shock should be attached to the cowl rim at full mass flow. This is not possible for the ST models owing to the large turning angle demanded at the entry (from angles corresponding to supersonic flow around a 30 deg cone to horizontal inside the cowl) but cowls SD2 and SD3 are designed for an attached second shock at 1·86 and cowl SD6 for an attached shock at 2·14.

To obtain more variation of M_{ul}, some of the models were tested with their centre bodies moved either fore or aft relative to the cowl (away from their design position). In these cases the model has been specified by a designation such as ST3 ($-$ 0·05 in.) or SD6 ($-$ 0·05 in.) etc., which indicates that the centre body has been moved back 0·05 in. relative to the cowl.

Some models with a 35-deg cone semi-angle have also been tested in combination with the cowls originally designed for the 30-deg conical centre bodies. The 35-deg centre body co-ordinates are also given in Fig. 4.

4.2. 9 *in.* $\times$ 9 *in. Tunnel Models.*—These models (Figs. 5 and 6) are based on designs whose drag characteristics at full mass flow were investigated theoretically in Ref. 11. The investigations led to the conclusion that the optimum cone angle for maximum net thrust (gross thrust minus external drag) was probably considerably below 30 deg. It may be noted that since the models were made, attention has been re-directed to cone angles in the region of 30 deg because of unstable flow conditions which are obtained at very small amounts of spillage with the smaller cone angles.

As mentioned earlier, these models have realistic values of $A_{entry}/A_{combustion\ chamber}$. In other words, for the Mach number range considered (1·5 to 2·0 for $\theta_c = 15$ deg and 22·5 deg and 1·6 to 2·4 for $\theta_c = 30$ deg), the designs will run as ram jets near critical flow conditions with maximum heat input.

The models were designed to be fitted with two alternative rear cowlings (Fig. 6), thus enabling the ratio A_{entry}/A_{max} to be changed. By testing both the arrangements, it was hoped to prove that the drag rise when spilling was not seriously affected by such a change and, therefore, that results which perforce had to be obtained with the parallel rear cowl because of reflected shock difficulties, could also be applied to the tapered-cowl models with only minor errors.

5. *Apparatus and Experimental Procedure.*—5.1. *Pressure Recovery Measurements.*—The model was screwed to a fixed sting and the exit area was controlled by a sliding cone which could be operated while the tunnel was running (Fig. 7). Three rakes of five Pitots each projected through the cone to measure the total pressure at the end of the subsonic diffuser. The apparatus (with nine Pitots instead of fifteen) is described and illustrated more fully in Ref. 11.

Measurements of total head before and after diffusion were made at zero incidence at Mach numbers of 1·86, 2·14, 2·48, 2·90 and 3·27 in the $5\frac{1}{2}$ in. $\times$ $5\frac{1}{2}$ in. Tunnel and at Mach numbers of 1·51, 1·62, 1·81 and 1·91 in the 9 in. $\times$ 9 in. Tunnel for various values of model exit area covering the subcritical and supercritical regimes of flow.

4

Schlieren photographs of the shock-configuration were taken and those with the inlet at full mass flow are presented.

5.2. *Drag Measurements.*—The method of obtaining external diffuser drag was to measure the total drag force on the model with a strain-gauge drag balance, and then the internal drag, base drag, sting force* and calculated skin-friction drag were subtracted.

The strain-gauge balance is shown in Figs. 8 and 9. It was found desirable when operating the balance in the tunnel to keep the temperature approximately constant, wind off and wind on. To ensure this a thermo-couple (copper-constantan junction) was installed.

Three rakes of seven Pitots each, spaced at 120-deg intervals, spanned the rear of the model. The inner tubes measured the pressure recovery of the internal flow and the outer tubes measured the base pressure.

The force acting on the rear of the support sting was determined by measuring the pressure in the balance housing.

All the tests were made at atmospheric stagnation pressure. The balance was calibrated before and after every run, the temperature in the balance housing being kept approximately constant throughout the running and calibrating period.

The flow was observed with a two-mirror schlieren system and some of the photographs taken are presented.

(a) *Internal drag.*—The internal drag coefficient is defined by:

$$C_{D\,\text{int}} = \frac{1}{q_\infty A_{\text{max}}} \{\rho_\infty V_\infty^2 A_\infty - (p_e - p_\infty + \rho_e V_e^2)A_e\}$$

and can be calculated from the measurement of mean total pressure recovery at the exit. It is assumed the pressure ratio across the exit is such that it is always choked. Details of the calculation are given in Ref. 3.

(b) *Base drag.*—As in some cases the reflected shock strikes the wake from the rear of the model at a position very near to the base, it was necesssry to check the base pressure (as recorded by the base Pitot-tubes) by making separate runs with base plugs containing static pressure holes. This check revealed errors of appreciable magnitude at some mass flows. However, by ensuring that the ends of all the tubes were in one plane and by reducing the gap between the base and the ends of the tubes to a minimum, reasonable agreement was eventually obtained.

(c) *Skin-friction drag.*—The external skin-friction drag has been calculated using values for skin-friction coefficient C_f for laminar and turbulent flow given in Ref. 12. As skin-friction drag is between a third and a half of the total drag at full mass flow and the ratio $C_{f\,\text{laminar}}/C_{f\,\text{turbulent}}$ is approximately one third, the percentage accuracy of the result would be considerably affected by whether fully laminar or turbulent flow was assumed. To determine the state of the boundary layer over the models, some transition points were observed using a chemical indicator. From these tests it was apparent that at full mass flow the boundary layer was laminar over the whole model except for wedges of turbulence emanating from small dents in the cowl rim and from the heads of three sets of screws joining the centre body to the cowl. In the calculations a value of C_f intermediate between the laminar and turbulent values (appropriate to the approximate amounts of laminar and turbulent flow) has been taken.

At reduced mass flow it was found that, in general, the boundary layer became turbulent just downstream of the cowl rim (presumably due to the presence of the 'over-expansion' shock on the cowl). Hence in the calculations the boundary layer has been taken as fully turbulent at all mass flows below the maximum.

---

* From the action of the internal balance pressure on the rear end of the sting.

6. *Discussion of Results.*—6.1. *Pressure Recovery.*—As has been seen (section 2) the main variation of pressure recovery with mass flow (the decrease with decreasing mass flow in the subcritical flow condition) is effected by the variation of r_i (the radius of the three-shock intersection point) with respect to the position of the streamline dividing the internal and external flows, r_α. A comparison of values of r_i/r_{cn} measured off Schlieren photographs with values calculated from equation (19), Appendix II, is shown in Figs. 10 to 14. The theoretical results can be calculated only when $r_i < r_\alpha$.

The comparison between estimated and experimental variation of pressure recovery with mass flow in the two sets of tests are shown in Figs. 15 to 43 and Figs. 45 to 52. The theoretical curves are calculated from equation (22), Appendix II, and therefore they do not include any allowance for the subsonic diffusion losses. As can be seen, the mass flow at which the pressure recovery begins to fall off (*i.e.*, when $r_i = r_\alpha$) and the initial slope of the curve are predicted reasonably well by the theory. As mass flow is reduced (and more of the subsonic diffusion is accomplished in front of the duct entry), it is to be expected that the subsonic diffusion loss will be decreased and hence the predicted and experimental curves should converge. This can be seen in some cases (Figs. 16, 46 and 51). In other cases, however, the opposite is true. This is probably explained by an overriding effect of the gradual divergence of measured and calculated r_i as shown in Figs. 12, 13 and 14.

When r_i is greater than r_α the theory (Appendix III) gives the pressure recovery as being solely a function of the position of the second shock on the centre body and the slope of the centre body at this position. Thus it is to be expected that agreement between the predicted and actual fall-off in pressure recovery near full mass flow will be best if, at the position of the second shock on the centre body, the slope of the surface is near to the original cone angle (*i.e.*, so that the amount of assumed two-dimensional expansion is small).

Studies of the flow at the corner such as is shown in Fig. 53 suggest that the shock loss and viscous effects cannot be separated in the manner suggested in Appendix III. In actual fact the boundary layer usually breaks away from the centre-body surface in the vicinity of the corner and the flow does not approximate to the expansion-shock process outlined in the Appendix. The increased loss experienced near to full mass flow is then largely the result of the subsonic mixing that occurs behind the separation resulting from the shock-boundary-layer interaction. Thus the agreement achieved is not particularly good in many cases (Figs. 26, 32 and 34).

When θ_w is smaller than θ_t and the cone shock can be reflected regularly inside the cowl at full mass flow, the problem of predicting pressure recovery in this condition becomes more difficult. No satisfactory method has been evolved and therefore for model SD3 at $M_\infty = 1 \cdot 86$, $2 \cdot 14$ and $2 \cdot 48$ and for model SD2 at $M_\alpha = 2 \cdot 48$ it has been assumed that the cone shock is not reflected, so that a Mach reflection is formed at the cowl lip just as for the ST series of cowls at full mass flow.

For models SD6 and ST3 at $M_\alpha = 2 \cdot 14$ and $2 \cdot 48$ and for the $\theta_c = 15$-deg model at $M_\infty = 1 \cdot 51$, r_i is greater than r_α at all mass flows (Figs. 10 to 12), and so theoretically the pressure recovery remains constant. For the $\theta_c = 22 \cdot 5$-deg drag model at $M = 1 \cdot 91$ a three-shock system cannot form (Fig. 57) and therefore the drop-off in pressure recovery cannot be predicted by the theory.

6.2. *External Drag.*—The results are shown in Figs. 21 to 43 and 45 to 52. Theoretical drags at full mass flow (cowl drag calculated by the method of Appendix IV, pre-entry drag from Ref. 10 and cowl-lip drag by the method of Ref. 8) in general compare well with the measured results. Where discrepancies do occur they are probably due to:

(a) Uncertainties in external mean-skin-friction drag coefficient due to separation of the external boundary layer under the influence of the reflected nose shock (Fig. 44a). This probably accounts for the low drags measured for SD6 at full mass flow at $M_\alpha = 3 \cdot 27$ (Fig. 24)

(b) The existence of detached shocks at the cowl lip at full mass flow.

6

These can occur for either of two reasons:

(i) Because the angle through which the entering flow is required to turn is larger than the maximum deflection angle for shocks at the cone flow Mach number

(ii) Choking of the internal duct due to excessive internal contraction. This condition may be aggravated due to boundary-layer breakaway at the shoulder of the centre body. For the ST3 (— 0·05 in.) and 35-deg III models the mass flow never reaches its theoretical maximum value at the lower Mach numbers due to choking at the minimum area section of the internal duct and due to the consequent detached shock at the cowl lip at full mass flow the drag is higher than predicted (Figs. 31 and 32 and 34 to 40). The variation of the maximum mass flow with Mach number for the 35-deg III model is rather haphazard and may be due to changing breakaway conditions at the duct throat (Figs. 34 to 37).

The slope of the drag versus mass-flow curve seems to be reasonably well predicted by the methods given in Appendix V. The mass flow at which the vortex sheet from the three-shock intersection point impinges upon the cowl lip (*i.e.*, when $r_i = r_\infty$) also seems to be well predicted except for SD6 (— 0·05 in.) at $M_\infty = 2·48$ (Fig. 26). This is a case where r_i is very nearly equal to r_∞ over a large range of mass flow (Fig. 54). Hence any small error in the prediction of r_i results in a large error in the estimation of the intersection points of the two curves.

Fig. 55 shows a comparison of drag measurements obtained at $M_\infty = 1·82$ with tapered and parallel rear cowls for $\theta_c = 30$ deg and 22·5 deg. As can be seen, the difference in drag between the two configurations at all mass flows is small. No conclusion can be drawn as to the relative rates of drag rise as the scatter of the results on repeat tests ($\pm 0·005$ of $C_{D\,\text{ext}}$) is roughly of the same order as the change in drag due to the change in model geometry.

7. *Conclusions.*—(*a*) The method (due to W. E. Moeckel) for predicting the position of the detached shock wave in front of a Pitot intake can be extended to the case of the conical centre-body intake and thus reasonable results for the fall-off in pressure recovery at reduced mass flow can be obtained.

(*b*) A crude but simple method (to take into account the curving of the centre body) for predicting the pressure recovery near full mass flow gives fair results for most practical designs.

(*c*) A method for predicting the rise in drag at reduced mass flow analogous to that developed in Ref. 3 for Pitot intakes gives quite good agreement with experimental results.

(*d*) The cowl drag of centre-body intakes at full mass flow can be satisfactorily predicted by linearised theory as developed for quasi-cylinders in Ref. 6.

7

LIST OF SYMBOLS

A Cross-sectional area

$$B = \frac{P_\infty}{P_s} \times \left(\frac{A^*}{A}\right)_\infty$$

$C_{D\,cowl}$ Cowl drag coefficient

$$= \frac{1}{q_\infty A_{max}} \int_C^E (p - p_\infty) 2\pi r \, dr$$

$C_{D\,ext}$ External diffuser drag coefficient

$$= C_{D\,cowl} + C_{D\,pre}$$

$C_{D\,int}$ Internal diffuser drag coefficient

$$= \frac{1}{q_\infty A_{max}} \{\rho_\infty V_\infty^2 A_\infty - (p_e - p_\infty + \rho_e V_e^2 A_e)\}$$

$C_{D\,pre}$ Pre-entry drag coefficient

$$= \frac{1}{q_\infty A_{max}} \int_A^C (p - p_\infty) 2\pi r \, dr$$

$$C_{D\,pre} = C_{D\,pre\,1} \left\{ = \frac{1}{q_\infty A_{max}} \int_A^B (p - p_\infty) 2\pi r \, dr \right\} + C_{D\,pre\,2} = \left\{ \frac{1}{q_\infty A_{max}} \int_B^C (p - p_\infty) 2\pi r \, dr \right\}$$

$\left.\begin{array}{l} C_{D\,pre} \\ C_{D\,cowl} \\ C_{D\,ext\,0} \end{array}\right\}$ Drag coefficients at full mass flow

$$C_{D\,spill} = C_{D\,cowl} - C_{D\,cowl\,0} + C_{D\,pre}$$

C_f Skin-friction drag coefficient

C_p Pressure coefficient $(p - p_\infty)/q_\infty$

L Distance of detached shock in front of intake

L_N Distance of tip of conical nose in front of intake

L_{SH} Distance of second shock in front of intake

M Mach number

M_{wl} Free-stream Mach number at which $\theta_w = \theta_l$

p Static pressure

P Total pressure

q Dynamic pressure $\frac{1}{2}\rho V^2$

Q Mass flow of a sonic stream

8

r		Radial co-ordinate
T		Total temperature
V		Velocity
x, s		Axial co-ordinates
α		Mach angle $\sin^{-1}\dfrac{1}{M}$
β	$=$	$\cot\alpha = \sqrt{(M^2 - 1)}$
ε	$=$	$\tan^{-1}\dfrac{1 - (r_{i\,max}/r_i)}{L_{i\,max}/r_{en}}$
η		Inclination of the sonic line
θ		Angle with respect to the diffuser axis of a line through the cone vertex
λ		Inclination of a streamline to the free-stream direction
ξ	$=$	dr/ds
ρ		Density
ϕ		Inclination of the 'third' shock to the free-stream direction
$(\ )_c$		On the cone surface
$(\ )_e$		At the exit
$(\ )_{en}$		At the entry
$(\ )_f$		At the final section of the subsonic diffuser
$(\ )_i$		At the three-shock intersection point
$(\ )_l$		At the cowl lip
$(\ )_\infty$		In the free stream
$(\ )^* (\ )_s$		Sonic conditions
$(\ )_m$		Mean value
$(\ )_0$		Co-ordinates of the vertex of the hyperbola

9

REFERENCES

No.	Author	Title, etc.
1	A. Ferri and L. M. Nucci	Theoretical and experimental analysis of low-drag supersonic inlets having a circular cross-section and a central body at Mach numbers of $3\cdot30$, $2\cdot75$ and $2\cdot45$. N.A.C.A. Report 1189. 1954.
2	E. L. Goldsmith, L. E. Fraenkel and C. F. Griggs	The performance of some centre body diffusers at supersonic speeds. R,A.E. Report Aero. 2372. A.R.C. 13,540.
3	W. E. Moeckel	Approximate method for predicting form and location of detached shock waves ahead of plane or axially symmetric bodies. N.A.C.A. Tech. Note 1921.
4	L. E. Fraenkel	The external drag of some Pitot-type intakes at supersonic speeds. Part I. R.A.E. Report Aero. 2380. A.R.C. 13,537. June, 1950.
5	M. J. Lighthill	Supersonic flow past bodies of revolution the slope of whose meridian section is discontinuous. *Quart. J. Mech. App. Math.* Vol. I, Part 1. March, 1948.
6	G. N. Ward	The approximate external and internal flow past a quasi-cylindrical tube moving at supersonic speeds. *Quart. J. Mech. App. Math.* Vol. I, Part 2. June, 1948.
7	L. E. Fraenkel	The theoretical wave drag of some bodies of revolution. R. & M. 2842. May, 1951.
8	L. E. Fraenkel	The external drag of some Pitot-type intakes at supersonic speeds. Part II R.A.E. Report Aero. 2422. A.R.C. 14,289. June, 1951.
9	Z. Kopal	Tables of supersonic flow around cones. MIT Tech. Report No. 1.
10	L. E. Fraenkel	Some curves for calculation of the performance of conical centre-body intakes at supersonic speeds and maximum mass flow. C.P. 108. December, 1951.
11	L. E. Fraenkel and E. L. Goldsmith	A preliminary investigation of the performance of conical supersonic diffusers. R.A.E. Tech Note Aero. 200. A.R.C. 12,582. June, 1949.
12	R. J. Monaghan and J. E. Johnson	The measurement of heat transfer and skin friction at supersonic speeds. Part II. C.P. 64. December, 1949.

APPENDIX I

Calculation of the Conditions at the Intersection Point of Three Shocks wiht Resultant Subsonic Flow

For the intersection of three shocks at a point to be possible the flow behind the single third shock and the flow behind the two shocks must both have the same static pressure and direction.

The graph of stream direction θ versus static-pressure ratio, p/p_∞, is drawn for the flow behind oblique shock waves occurring at the free-stream Mach number (Fig. 56 is a typical example for a 30-deg cone semi-angle at $M_\infty = 1 \cdot 86$). The point a is defined by the conical shock and forms the origin for the second graph shown superimposed for oblique shocks occurring in the flow immediately behind the conical shock. The intersection point b', c of these two graphs gives the static-pressure and flow-direction conditions downstream of the shocks necessary for the system to exist.

It is found that for small cone angles at high free-stream Mach numbers, the intersection point b', c can give negative values for the deflection of the free stream through the third shock. It seems unlikely that this is a physically possible three-shock system. Photographs taken of these configurations show that a four-shock system forms in these cases, the additional shock coming from a boundary-layer thickening, occurring between the first and second shocks (Fig. 57). Such a four-shock system with resultant subsonic flow is not uniquely determined as is the three shock arrangement, and hence when these conditions obtain no attempt has been made to calculate pressure recovery or drag rise. A graph can be plotted (Fig. 58) of cone angle against limiting Mach number M_{lim} above which a three-shock system is no longer possible (i.e., M_{lim} is the Mach number at which $\theta_{w\,3} = 90$ deg and $\delta_{b',c} = 0$).

APPENDIX II

The Method of Estimating the Position of the Detached Shock Wave in Front of Pitot and Centre-Body Intakes at Any Mass Flow

The method derived by Moeckel[3] for calculating the position of the detached shock in front of a Pitot entry for any given mass flow below the maximum value, has been applied to conical centre-body inlets for mass flows such that the entering stream-tube radius r_∞ is greater than the radius of the three-shock intersection point r_i.

It is convenient to reproduce here the method as given for Pitot intakes. The modifications necessary when applying the method to centre-body inlets can then be more clearly presented.

(*a*) *Pitot Entry.*—It is assumed that the detached wave is of hyperbolic form asymptotic to the free-stream Mach angle, and the intersection of the stagnation streamline (which separates the interior from the exterior flow) with the detached shock is assumed to be the vertex of the hyperbola (Fig. 59). It is further assumed that the sonic body point S_{en} is located at the lip of the cowl and that the sonic line SS_{en} is straight. A continuity relationship can then be established to locate the hyperbola axially with respect to the inlet.

From Fig. 59, the distance L of the detached wave in front of the entry is given by:

$$L = x_{en} - x_0 \qquad \cdots \qquad \cdots \qquad \cdots \qquad \cdots \qquad \cdots \qquad (1)$$

where

$$x_{en} = x_s + (r_s - r_{en}) \tan \eta , \quad \cdots \qquad \cdots \qquad \cdots \qquad \cdots \qquad (2)$$

and where the distances x are measured from the origin of the hyperbola.

r_{en} is known and an approximate value can be assigned to the inclination of the sonic line η.

The quantities x_s and x_0 can be obtained in terms of r_s from the equation of the hyperbola:

$$r - r_\infty = \sqrt{(x^2 - x_0^2)} \tan \alpha \qquad \cdots \qquad \cdots \qquad \cdots \qquad \cdots \qquad (3)$$

where α is the Mach angle.

Differentiating:

$$\frac{dr}{dx} = \tan \phi = \frac{\left[\sqrt{\{(r - r_\infty)^2 \cot^2 \alpha + x_0^2\}} \right]}{(r - r_x)} \tan^2 \alpha . \quad \cdots \qquad \cdots \qquad \cdots \qquad (4)$$

Hence at the point S on the shock wave where the inclination of the shock ϕ_s is known, we have:

$$\tan \phi_s = \frac{\left[\sqrt{\{(r_s - r_\infty)^2 \cot^2 \alpha + x_0^2\}} \right] \tan^2 \alpha}{r_s - r_\infty} . \qquad \cdots \qquad \cdots \qquad \cdots \qquad \cdots \qquad (5)$$

Also from equation (3):

$$x_s = \sqrt{\{(x_0^2 + (r_s - r_\infty)^2 \cot^2 \alpha\}} , \qquad \cdots \qquad \cdots \qquad \cdots \qquad \cdots \qquad \cdots \qquad (6)$$

and so from equations (5) and (6):

$$x_s = \frac{(r_s - r_\infty) \tan \phi_s}{\tan^2 \alpha} . \qquad \cdots \qquad \cdots \qquad \cdots \qquad \cdots \qquad \cdots \qquad \cdots \qquad (7)$$

Finally we can apply a continuity condition to determine r_s. The mass flow Q of a sonic stream is given by $Q = PA^* f(T_\infty)$.

T_∞ is constant across a shock wave, thus equating the mass flows in the sonic stream BS, and the sonic stream from which the free-stream flow A_0 isentropically expands:

$$P_s A_s = P_\infty A_0^* \text{ (Fig. 59),}$$

or

$$\frac{P_s}{P_\infty} \left(\frac{A}{A^*} \right)_0 = \frac{A_0}{A_s} , \qquad \cdots \qquad \cdots \qquad \cdots \qquad \cdots \qquad \cdots \qquad \cdots \qquad \cdots \qquad \cdots \qquad (8)$$

so that

$$\frac{A_s}{\pi} = \frac{r_s^2 - r_{en}^2}{\cos \eta} = \frac{P_\infty}{P_s} \left(\frac{A^*}{A} \right)_0 \left(r_s^2 - r_\infty^2 \right) ,$$

and

$$\frac{r_s}{r_{en}} = \left\{ \frac{1 - B \cos \eta \, (r_\infty/r_{en})^2}{1 - B \cos \eta} \right\}^{1/2} \qquad \cdots \qquad \cdots \qquad \cdots \qquad \cdots \qquad \cdots \qquad (9)$$

where

$$B = \frac{P_\infty}{P_s} \times \left(\frac{A^*}{A} \right)_0 . \qquad \cdots \qquad \cdots \qquad \cdots \qquad \cdots \qquad \cdots \qquad \cdots \qquad \cdots \qquad (10)$$

P_∞/P_s varies across the sonic stream; an appropriate average value is that existing along the streamline which contains the centre of gravity of the fluid passing the sonic line. This centroid

12

streamline enters the shock wave between $r = (r_s + r_\infty)/2$ and $r = (2r_s + r_\infty)/3$ being nearer to the former value at small spillages and nearer to the latter at large spillages. The inclination of the shock wave (and hence P_∞/P_s) at these two values of r can be obtained from equations (4), (6) and (7) (This has been done in Ref. 3, where a graph (Fig. 5) is presented of P_∞/P_s against Mach number for the two cases).

At S, the inclination of the flow λ_s is known. At B the inclination is assumed to be the angle for shock detachment.

Thus a mean value is taken for η:

$$\eta = \frac{\lambda_s + \lambda_d}{2} \text{ (plane flow)}$$

$$\eta = \frac{\lambda_s + \theta_d}{2} \text{ (axially symmetric flow)}.$$

As λ_s differs only slightly from λ_d the inclination of the sonic line for plane flow is assumed to be $\eta = \lambda_s$. These two values for η are presented in Fig. 4, Ref. 3.

Thus finally:

$$L = x_s + (r_s - r_{en}) \tan \eta - x_0 \qquad .. \qquad .. \qquad .. \qquad .. \qquad .. \qquad (11)$$

and from equations (5) and (7):

$$\frac{L}{r_{en}} = \frac{\left(\dfrac{r_s}{r_{en}} - \dfrac{r_\infty}{r_{en}}\right) \tan \phi_s}{\tan^2 \alpha} + \left(\frac{r_s}{r_{en}} - 1\right) \tan \eta - \frac{\left(\dfrac{r_s}{r_{en}} - \dfrac{r_\infty}{r_{en}}\right)}{\tan^2 \alpha} \sqrt{(\tan^2 \phi_s - \tan^2 \alpha)} . \qquad .. \qquad (12)$$

(b) *Conical Centre-Body Intakes.*—This case is illustrated in Fig. 60. So long as $r_\infty > r_i$ a similar procedure to that given for the Pitot intake can be adopted. A slope condition now replaces the original assumption that the hyperbola has its vertex on the stagnation streamline. It is assumed that the third shock is straight and inclined at the angle ϕ (as determined from the three-shock intersection calculations) from the point of intersection to the stagnation streamline.

Thus for the hyperbola:

$$r - r_0 = \sqrt{(x^2 - x_0^2)} \tan \alpha , \qquad .. \qquad .. \qquad .. \qquad .. \qquad .. \qquad .. \qquad (13)$$

$$\frac{dr}{dx} = \tan \phi = \frac{[\sqrt{\{(r - r_0)^2 \cot^2 \alpha + x_0^2\}}] \tan^2 \alpha}{(r - r_0)} . \qquad .. \qquad .. \qquad .. \qquad (14)$$

We now have the condition $dr/dx = \tan \phi_\infty$ when $r = r_\infty$, where ϕ_∞ is the angle of the third shock with respect to the free-stream direction.

Hence, on substituting this and the original condition $dr/dx = \tan \phi_s$ when $r = r_s$ and re-arranging we obtain:

$$x_0 = \frac{r_s - r_\infty}{\tan \alpha \left\{\left(\dfrac{\tan^2 \phi_s}{\tan^2 \alpha} - 1\right)^{-1/2} - \left(\dfrac{\tan^2 \phi_\infty}{\tan^2 \alpha} - 1\right)^{-1/2}\right\}} \qquad .. \qquad .. \qquad (15)$$

and

$$r_0 = r_\infty - \frac{x_0 \tan \alpha}{\left(\dfrac{\tan^2 \phi_s}{\tan^2 \alpha} - 1\right)^{1/2}} . \qquad .. \qquad .. \qquad .. \qquad .. \qquad .. \qquad (16)$$

13

The procedure is then exactly as before for the Pitot intake and we finally obtain:

$$\frac{L}{r_{en}} = \left[\frac{(r_s/r_{en}) - (r_\infty/r_{en})}{\tan \alpha \left\{ \left(\frac{\tan^2 \phi_s}{\tan^2 \alpha} - 1\right)^{-1/2} - \left(\frac{\tan^2 \phi_\infty}{\tan^2 \alpha} - 1\right)^{-1/2} \right\}}\right]$$

$$\left[\frac{\tan \phi_s}{(\tan^2 \phi_s - \tan^2 \alpha)^{1/2}} - \frac{\tan \phi_\infty}{(\tan^2 \phi_\infty - \tan^2 \alpha)^{1/2}}\right] + \left(\frac{r_s}{r_{en}} - 1\right) \tan \eta \quad .. \quad (17)$$

where, as before:
$$\frac{r_s}{r_{en}} = \left\{\frac{1 - B \cos \eta \, (r_\infty/r_{en})^2}{1 - B \cos \eta}\right\}^{1/2} . \qquad .. \qquad .. \qquad .. \qquad .. \qquad .. \qquad (18)$$

The results obtained for the shock position ahead of the entry from the above expression agree better with experimental measurements from photographs if two-dimensional values for η and P_s/P_∞ are taken for all mass flows (In Ref. 3 a similar recommendation is made for small spillages).

Having determined L, we then have (Fig. 60):

$$\frac{r_i}{r_{en}} = \frac{\dfrac{r_\infty}{r_{en}} - \left(\dfrac{L_N - L}{r_{en}}\right) \tan \phi_\infty}{1 - \cot \theta_w \tan \phi} \qquad .. \qquad .. \qquad .. \qquad .. \qquad .. \qquad (19)$$

and
$$\frac{L_i}{r_{en}} = \frac{L_N}{r_{en}} - \frac{r_i}{r_{en}} \cot \theta_w . \qquad .. \qquad .. \qquad .. \qquad .. \qquad .. \qquad .. \qquad (20)$$

Thus from equation (19) we can determine at any mass flow the proportion of the entering stream-tube air which passes through the two-shock system (the rest passing through the single third shock).

The pressure recovery through the two shocks can be determined if we assume that the second shock is normal to the mean flow direction between the cone shock and the cone surface and occurs at a mean Mach number:

$$M = \frac{M_w + M_c}{2} . \qquad .. \qquad .. \qquad .. \qquad .. \qquad .. \qquad (21)$$

The pressure recovery through the third shock is also determined as we know its direction to the free stream from the three-shock - intersection calculations.

Thus finally an area mean of these two streams of differing total head gives the predicted pressure recovery at any mass flow, $i.e.$,

$$\frac{P_{en}}{P_\infty} = \frac{\left(\dfrac{P}{P_\infty}\right)_{\text{3rd shock}} \times \left(\dfrac{r_\infty^2}{r_{en}^2} - \dfrac{r_i^2}{r_{en}^2}\right) + \left(\dfrac{P}{P_\infty}\right)_{\text{cone shock + normal shock}} \times \left(\dfrac{r_i^2}{r_{en}^2}\right)}{(r_\infty^2/r_{en}^2)} \qquad .. \qquad .. \qquad (22)$$

This method for calculating the shock pressure recovery is rather tedious to apply and its application has been facilitated by the addition of some graphs (Figs. 62 to 78) at the end of the report.

In Figs. 62 to 65 L/r_{en} (equation (17)) has been plotted against free-stream Mach number M_∞ for a range of mass-flow ratios A_∞/A_{en} for cone angles of 15, 20, 22·5, 25, 30 and 35 deg.

If the cowl-lip position angle θ_l is known, r_i/r_{en} can be calculated from equation (19) and Fig. 66 (θ_w vs. M_∞) and Fig. 67 (ϕ_∞ vs. M_∞).

Finally P_{en}/P_∞ is calculated from equation (22) with the aid of graphs of $P/P_\infty)_{\text{cone + normal shock}}$ vs. M_∞ (Figs. 68 to 70) and $(P/P_\infty)_{\text{3rd shock}}$ vs. M_∞ (Figs. 71 and 72).

14

APPENDIX III

A Method for Calculating the Pressure Recovery
when r_i is Greater than r_∞

We require to extend the pressure-recovery mass-flow curve from the mass flow at which $r_i = r_\infty$ up to full mass flow. In this region the pressure recovery will, in general, begin to drop off slightly due to expansion effects around the centre body. These effects can be calculated if the position of the second shock along the centre body is known. As the flow field in front of the shock is non-uniform and three-dimensional, the true form of the shock can only be determined by characteristic methods. However, a simplified approach may lead to useful results.

We assume (Fig. 61) that the shock is plane extending from the limiting entry streamline to the centre-body surface and inclined normal to the mean stream direction λ_m (*i.e.*, normal to the flow at $\bar\theta = (\theta + \theta_c)/2$. It is also assumed that the expansion round the centre body is two-dimensional so that the mean free-stream Mach number, $\bar M = (M_c + M_\theta)/2$, at which the normal shock is assumed to occur, is easily determined. The position of the shock at any mass flow is found by extending the curve of L_i/r_{en} versus mass flow already obtained (up to the point where $r_i = r_\infty$). This is done by fairing in a curve of parabolic form having the same slope at the point where $r_i = r_\infty$ and becoming zero at full mass flow (Fig. 14).

From Fig. 61 we have:

$$\theta = \tan^{-1}\left\{\frac{r_{i\,\max} + \tan \varepsilon\,(L_{i\,\max} - L_{SH})}{L_N - L_{SN}}\right\}$$

where

$$\varepsilon = \tan^{-1}\frac{1 - \dfrac{r_{i\,\max}}{r_{en}}}{\dfrac{L_{i\,\max}}{r_{en}}}$$

and finally

$$x_c \simeq \frac{\{r_{i\,\max} + \tan \varepsilon\,(L_{i\,\max} - L_{SH})\}\cos(\theta - \lambda_m)\cos\theta_c}{\sin\theta\,\cos(\lambda_m - \theta_c)}.$$

Hence the local slope of the centre body can be calculated and finally (by the use of cone flow tables) the mean Mach number, $\bar M = (M_c + M_\theta)/2$, at which the normal shock occurs.

APPENDIX IV

The Method of Calculating Cowl Drag at Full Mass Flow

The pressure coefficient C_p at a point x from the lip of the cowl is given by[5,7]:

$$\frac{\beta C_p}{2} = \int_0^z U(z - s)\,d\xi(s),$$

which is a Stieltje's integral,

where $\beta = \sqrt{(M^2 - 1)}$

$z = x/\beta r_m$

r_m is a mean value of r

$\xi(s) = dr/dx$, the slope of the cowl at $s\beta r_m$

U is a function tabulated in Ref. **5**.

If the initial slope of the cowl is zero and there are no discontinuities of slope, the integral reduces to the ordinary Riemann integral:

$$\int_0^z U(z - s)\, \xi'(s)\, ds,$$

but otherwise it must be written as:

$$\frac{\beta C_p}{2} = \int_0^z U(z - s)\, \xi'(s)\, ds + U(z)\, \xi(o) + \sum_1^i U(z - z_i)\, \Delta\xi_i$$

where there are i discontinuities occurring in the interval $(0,x)$ at the points $x_1 \ldots \ldots x_i$ with increments of slope $\Delta\xi_1 \ldots \ldots \Delta\xi_i$ and $z_1 = x_1/\alpha r_m$, etc.

For a conical centre-body diffuser with the cone shock outside the lip, there are several ways in which the linear theory may be used to give the cowl drag. The method adopted has been to determine the point at which the streamline bounding the entering flow crosses the cone shock by exact conical flow data[9], then to join this point to the cowl lip and regard this line as an extension of the cowl, thus reducing the problem to that of a Pitot intake. The pressure coefficient C_p on the physical cowl at a point x from the lip of the extended cowl of one of the drag models is given by $\beta C_p/2 = U(z)\xi_0 + U(z - z_1)(\xi_1 - \xi_0) + U(z - z_2)(\xi_2 - \xi_1)$ where ξ_0, ξ_1 and ξ_2 are the three slopes, as these models have constant slope but for one discontinuity. This can be integrated over the physical cowl to give the drag coefficient.

$$C_D = \frac{1}{\pi R_{\max}^2} \int_{x1}^{x3} C_p 2\pi r\xi\, dx.$$

In the development of the theory it is assumed that the radius takes on some mean value at each point. We have, therefore, for the sake of consistency and simplicity, replaced r by a mean value r_m. The mean chosen has been the arithmetic one of the maximum and entry radii of the extended cowl:

$$C_D = 4\left(\frac{r_m}{r_{\max}}\right)^2\left[\xi_1^2\, U_1(z_2 - z_1) + \xi_2^2\, U_1(z_3 - z_2)\right.$$

$$+ \xi_1\xi_2\{U_1(z_3 - z_1) - U_1(z_3 - z_2) - U_1(z_2 - z_1)\}$$

$$+ \xi_2\xi_0\{U_1(z_3) + U_1(z_2 - z_1) - U_1(z_2) - U_1(z_3 - z_1)\}$$

$$\left.+ \xi_0\xi_1\{U_1(z_2) - U_1(z_1) - U_1(z_2 - z_1)\}\right],$$

where $U_1(z) = \int_0^z U(z)\, dz$ and is tabulated in Ref. **7**.

It is possible to calculate the pressure coefficient at the lip of the models by calculating the pressure in the conical flow field and assuming that the flow expands two-dimensionally around the lip. A comparison of these exact figures and those obtained by linear theory is given in Table 1.

16

APPENDIX V

The Calculation of External Drag Coefficient, $C_{D\,ext}$, under Spillage Conditions

The calculation of the non-linear drag-rise characteristic discussed in section 3.1 can be considerably simplified if it is assumed that the variation of drag is linear between full mass flow $(A_\infty/A_{en})_{max}$ and the mass flow $(A_\infty/A_{en})_{r\,i\,=\,r\,\infty}$ at which the vortex sheet from the three-shock intersection point becomes the stagnation streamline dividing the internal and external flows.

Thus the drag in this position $(r_i = r_\infty)$ is given by:

$$C_{D\,ext} = C_{D\,cowl\,0} + \frac{\left(\frac{p_{w\,3}}{p_\infty} - 1\right)\left\{1 - \left(\frac{A_\infty}{A_{en}}\right)_{r\,i\,=\,r\,\infty}\right\}}{\frac{q_\infty}{p_\infty}\left(\frac{A_{max}}{A_{en}}\right)} \qquad .. \qquad .. \qquad (1)$$

and the drag at any lower mass flow $(A_\infty/A_{en})_{r\,i\,<\,r\,\infty}$ is similarly given by:

$$C_{D\,ext} = C_{D\,cowl\,0} + \frac{\left(\frac{p_{w\,3}}{p_\infty} - 1\right)\left\{1 - \left(\frac{A_\infty}{A_{en}}\right)_{r\,i\,<\,r\,\infty}\right\}}{\frac{q_\infty}{p_\infty}\left(\frac{A_{max}}{A_{en}}\right)} . \qquad .. \qquad .. \qquad (2)$$

Curves of $(A_\infty/A_{en})_{r\,i\,=\,r\,\infty}$ and $(A_\infty/A_{\infty\,max})_{r\,i\,=\,r\,\infty}$ against M_∞ for a range of θ_l have been plotted (Figs. 73 to 78), which should facilitate the above calculation. They should also help to indicate (at least for cone-surface Mach numbers below 1·35) the relative mass flow at which oscillation will commence due to the impinging of the vortex sheet from the three-shock intersection on the cowl lip (Ferri's criterion[1]).

Now, as we saw in section 6.1, for a given cowl angle and free-stream Mach number, a minimum lip-position angle θ_l may exist below which the shock intersection point will always remain in the external flow (i.e., r_i is always greater than r_∞). To apply similar methods as those used above for calculating the drag when spilling, it is now necessary to know the position of the second shock.

As in section 3.1 the drag in this condition is considered to be:

$$C_{D\,ext} = C_{D\,pre\,1} + C_{D\,pre\,2} + \Delta C_{D\,cowl} + C_{D\,cowl\,0} \qquad .. \qquad .. \qquad .. \qquad (3)$$

where

$$C_{D\,pre\,1} = \frac{1}{q_\infty A_{max}} \int_A^B (p - p_\infty) 2\pi r\, dr, \qquad .. \qquad .. \qquad .. \qquad .. \qquad (4)$$

and

$$C_{D\,pre\,2} + \Delta C_{D\,cowl} = \frac{1}{q_\infty A_{max}} (p_{w\,2} - p_\infty)(A_{en} - A_{w\,2}) . \qquad .. \qquad .. \qquad (5)$$

The second shock is assumed to be attached to the cowl lip at maximum mass flow and its position at zero mass flow is calculated according to the method of Ref. 3, treating the intake as a closed body. A linear movement with variation of mass flow is assumed between these two limits.

It is difficult to evaluate equations (4) and (5) without making some approximations. In the present calculations it has been assumed that the streamline ABC (Fig. 79) is straight and that its slope λ is the same at all mass flows.

$$\lambda = \tan^{-1} \frac{1 - \sqrt{\left(\frac{A_\infty}{A_{en}}\right)_{max}}}{\cot \theta_l - \sqrt{\left(\frac{A_\infty}{A_{en}}\right)_{max}} \cot \theta_w}, \qquad .. \qquad .. \qquad .. \qquad (6)$$

where $(A_\infty/A_{en})_{max}$ is plotted (as A_∞/A_i) against M_∞ for a range of θ_l and θ_c in Ref. 10.

TABLE 1

Comparison of Cowl-Lip Pressure Coefficients as
Calculated by Linearised and Exact Theories

Model (deg)	Mach number	Exact $C_{p\,\text{lip}}$	Linear $C_{p\,\text{lip}}$
15	1·51	0·251	0·227
22·5	1·51	0·203	0·205
	1·61	0·208	0·195
	1·82	0·212	0·176
	1·91	0·199	0·170
30	1·82	0·141	0·152
	1·91	0·149	0·148
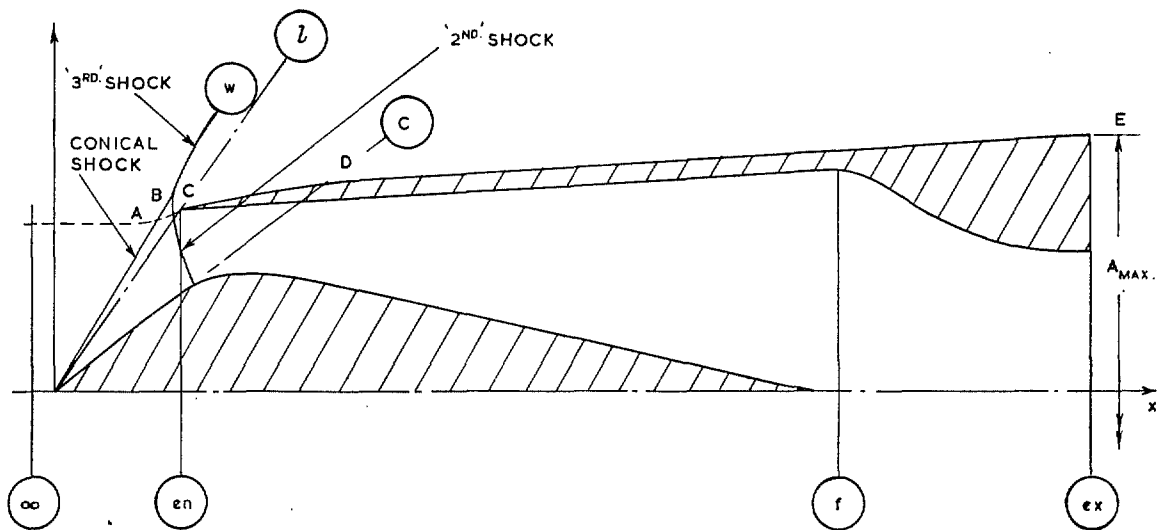
FIG. 1.   Suffix notation.

(a) $\theta_l < \theta_w$ (b) $\theta_l > \theta_w$
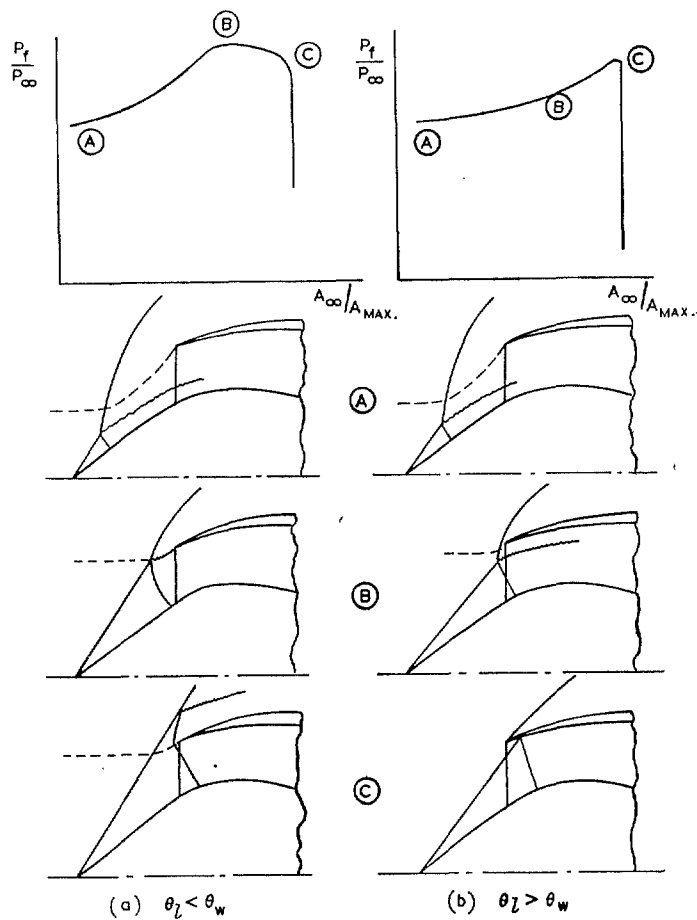
FIGS. 2a and 2b.   Pressure recovery at reduced mass flow.

19
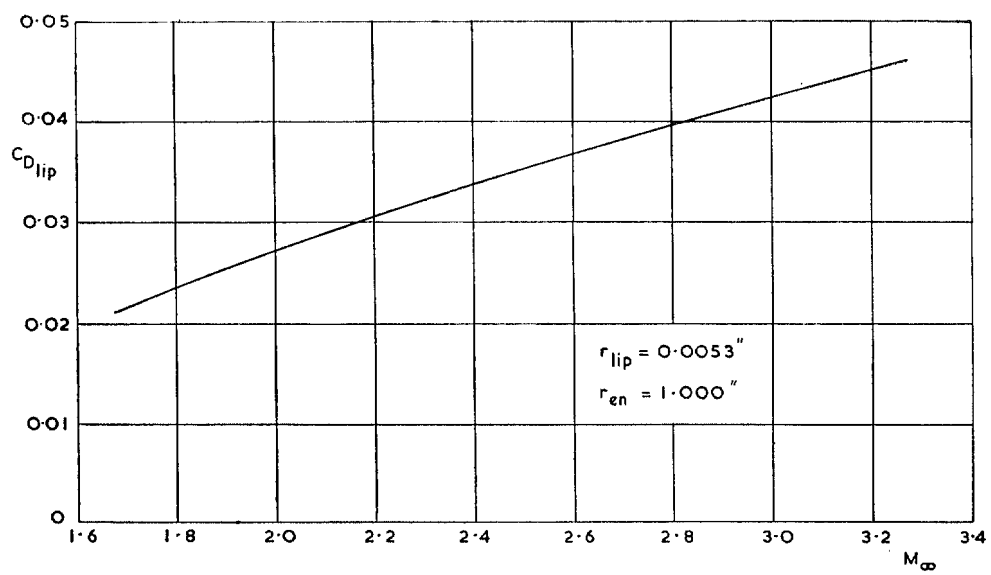
FIG. 3. Cowl-lip drag coefficient ($C_{D\,lip}$).

CENTRE BODY	35°III	30°ST0	30°ST3	30°ST4
x	DIA.y	DIA.y	DIA.y	DIA.y
O	O	O	O	O
0.80		0.927	0.940	0.940
0.90		1.038	1.063	1.049
1.00	1.384	1.118	1.175	1.149
1.10		1.152	1.290	1.222
1.20	1.420	1.151	1.360	1.245
1.30		1.150	1.390	1.248
1.40	1.404	1.146	1.395	1.246
1.50		1.128	1.392	1.240
1.60	1.390		1.390	
1.70			1.388	
1.80	1.372		1.385	1.220
2.00	1.356		1.365	1.203
2.20	1.338		1.350	1.177
2.40	1.312		1.330	1.150
2.60	1.294		1.305	
2.80	1.252			
3.277				0.997

(FROM 1.50 TAPER ANGLE=2°12')
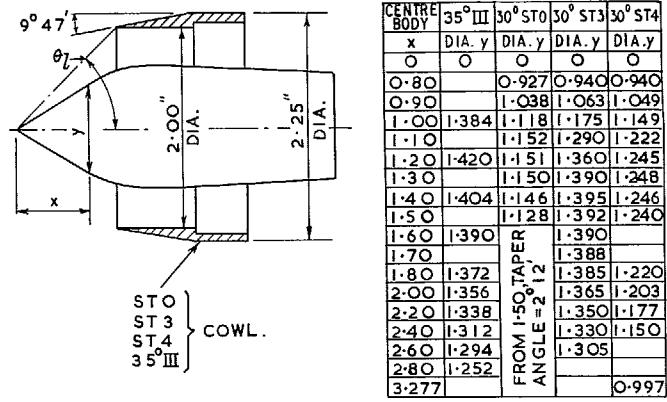
CONFIGURATION	C.B. POSITION (FROM DESIGN POSITION)	θ_l	M_{wl}
35° - III	0"	46.2	2.90
35° - III	-0.05"	47.1	2.62
30° -STO	0"	44	2.35
30° -ST3	0"	40.3	2.90
30° -ST3	-0.05"	41.6	2.66
30° -ST4	0"	47°	2.08

CENTRE BODY SD3-30		SD3 COWL		
x	DIA.y	x	DIA.yo	DIA.yi
0.00	0.004	0.00	1.897	1.885
0.70	0.811	0.10	1.947	1.923
0.80	0.923	0.20	1.993	1.955
0.90	1.013	0.30	2.030	1.979
1.00	1.077	0.40	2.069	1.990
1.20	1.144	0.50	2.100	1.998
1.40	1.155	0.60	2.130	2.000
1.60	1.140	0.80	2.173	2.000
1.80	1.120	1.00	2.207	2.000
2.00	1.099	1.20	2.231	2.000
2.80	1.019	1.40	2.244	2.000
2.00	1.009	1.60	2.250	2.000

CONFIGURATION	C.B. POSITION (FROM DESIGN POSITION)	θ_l	M_{wl}
30°-SD3	0"	50.7	1.86

CENTRE BODY	35°I	30°SD2	SD2 COWL		
x	DIA.y	DIA.y	xc	DIA.yo	DIA.yi
O	0.010	O	O	1.820	1.800
0.70	0.819		0.10	1.893	1.853
0.80	0.934		0.20	1.963	1.906
0.90		1.260	0.30	2.023	1.946
1.00	1.149	1.366	0.40	2.080	1.976
1.20	1.313	1.486	0.50	2.128	1.993
1.40	1.392	1.534	0.60	2.175	1.999
1.60	1.402	1.542	0.70	2.202	1.999
1.80	1.392	1.538	0.80	2.226	1.999
2.00	1.367	1.530	0.90	2.241	1.999
2.20	1.339	1.520	1.00	2.245	1.999
2.40		1.510	1.10	2.248	1.999
2.60		1.496			
2.80		1.478			
3.00	1.225				
3.10	1.229				

CONFIGURATION	C.B. POSITION (FROM DESIGN POSITION)	θ_l	M_{wl}
35°I - SD 2	0"	46.2	2.90
30° - SD 2	0"	44.1	2.34

DIMENSIONS ARE IN INCHES
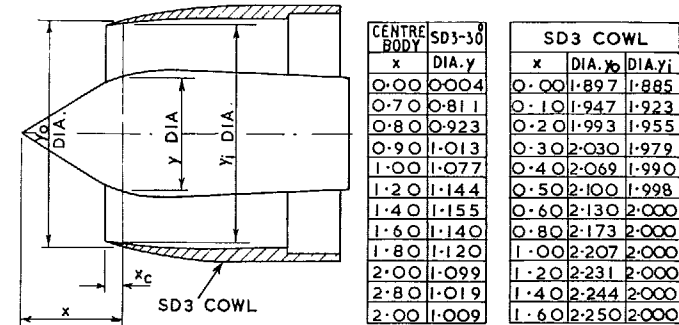
CENTRE BODY SD6-30		SD6 COWL		
x	DIA.y	x	DIA.yi	DIA.yo
O	0.007	O	1.915	1.905
1.00	1.158	1.10	1.959	1.920
1.20	1.372	0.20	2.002	1.950
1.40	1.483	0.30	2.041	1.972
1.60	1.512	0.40	2.080	1.990
1.80	1.510	0.50	2.112	1.995
2.00	1.503	0.60	2.145	1.998
2.20	1.490	0.70	2.171	1.998
2.40	1.477	0.80	2.196	1.998
2.60	1.456	1.00	2.232	1.998
2.80	1.427	1.10	2.243	1.998
2.90	1.408	1.30	2.250	1.998
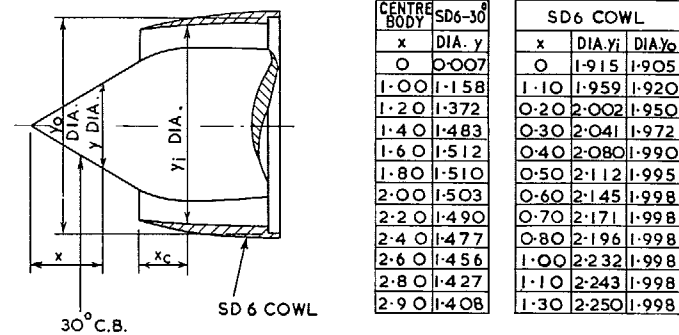
CONFIGURATION	C.B. POSITION (FROM DESIGN POSITION)	θ_l	M_{wl}
SD6 - 30°	0"	40.0	2.94
	-0.05"	42.7	2.51

DIMENSIONS ARE IN INCHES.

FIGS. 4a and 4b. Model details and dimensions (5½ in. × 5½ in. Tunnel tests).

9" x 9" TUNNEL MODELS

15°   22·5°   30°

SD2

SD3

SD6

STO   ST4   ST3

5¼" x 5¼" TUNNEL MODELS
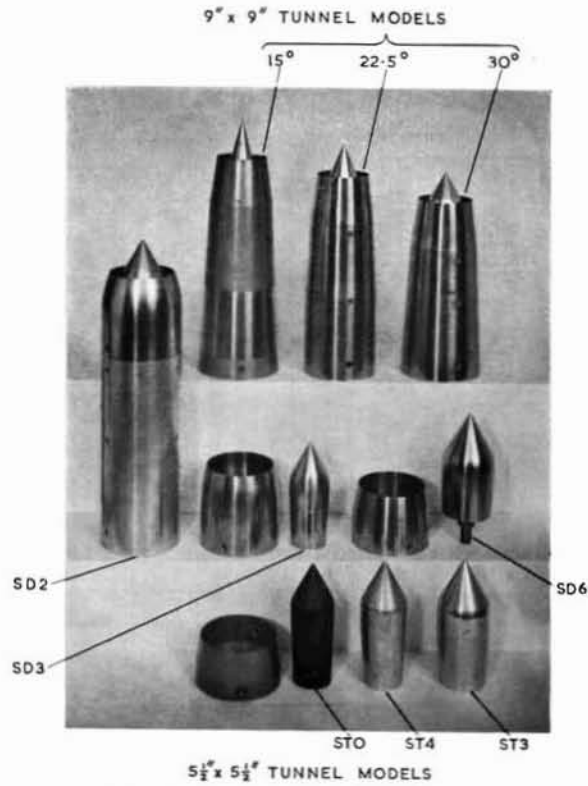
FIG. 5.   General view of models.

5°

3°

32° 47'

1·527 DIA.

1·23 RAD

2·00

15° DRAG MODEL

ALTERNATIVE
PARALLEL REAR
COWL

39° 38'

1·570 DIA.

0·70 DIA

22·5 DRAG MODEL

DETACHABLE
PLUG

44° 56'

1·651 DIA.

30° DRAG MODEL
SHOWING METHOD OF ATTACHMENT OF CENTRE BODY.
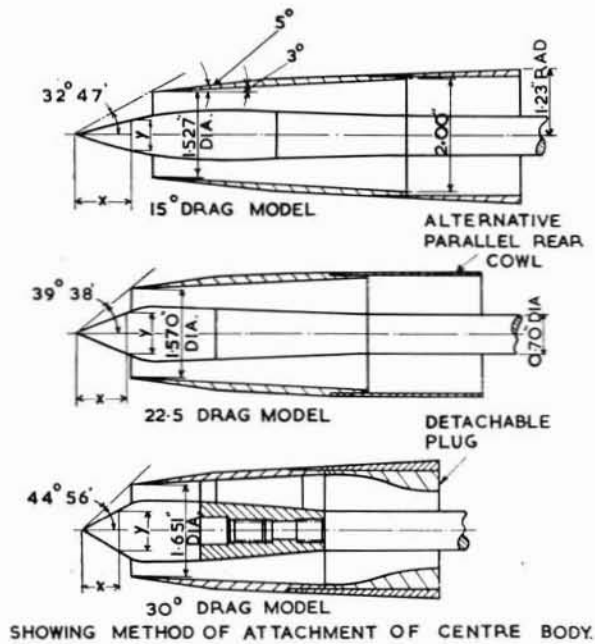
x	DIA. 'y'
0	0
0·90	0·763
1·00	0·844
1·10	0·915
1·20	0·948
1·30	0·965
1·40	0·975
1·50	0·981
1·60	0·980
1·70	0·975
1·80	0·970
1·90	0·965
2·00	0·955

x	DIA. 'y'
0	0
1·20	0·655
1·30	0·700
1·40	0·735
1·50	0·760
1·60	0·785
1·70	0·805
1·95	0·840
2·20	0·860
2·45	0·880
2·95	0·860
3·20	0·850
3·485	0·825

x	DIA. 'y'
0	0
0·80	0·940
0·90	1·025
1·00	1·064
1·10	1·085
1·20	1·100
1·30	1·115
1·40	1·120
1·50	1·125
1·60	1·130
1·70	1·131
1·80	1·128
1·90	1·124

FIG. 6.   Model details and dimensions (9 in. × 9 in. Tunnel tests).

22
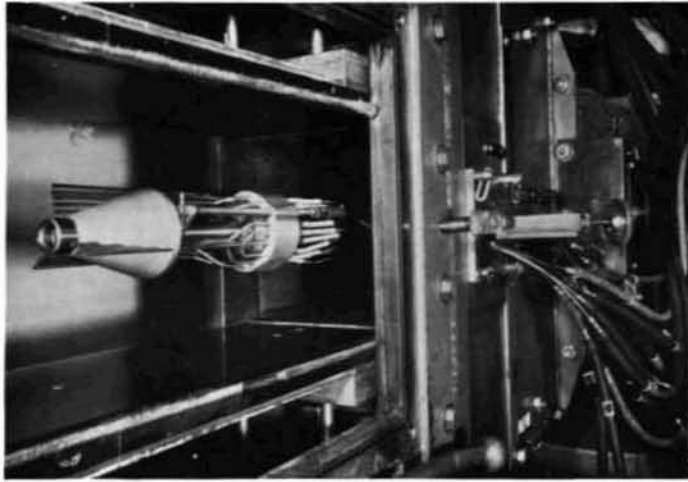
FIG. 7. Pressure-recovery–measurement test rig installation in R.A.E. No. 4(5½ in. × 5½ in.) Supersonic Tunnel.

BASE PRESSURE PITOT RACK

EXIT FLOW PITOT RACK

STING
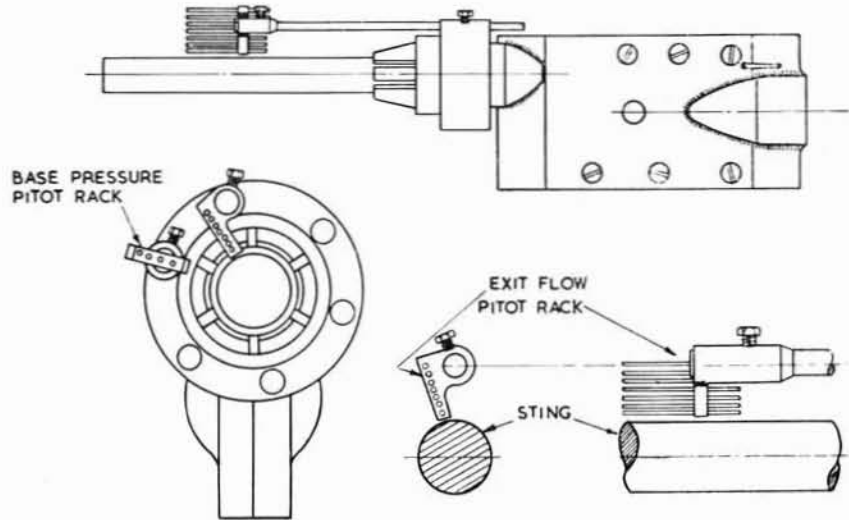
FIG. 8. Strain-gauge drag balance.
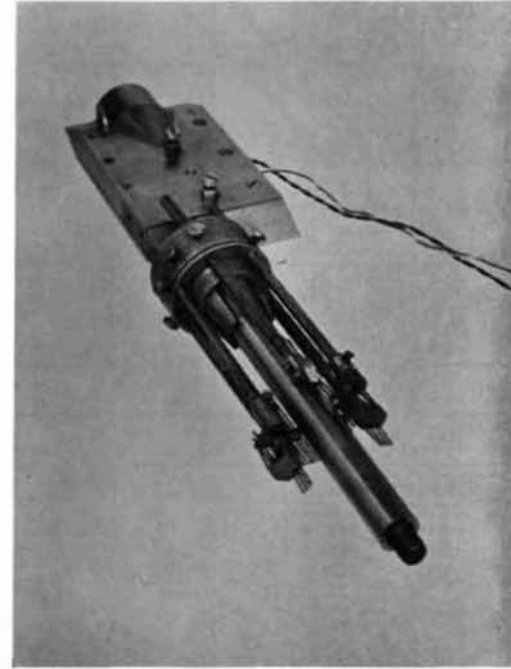
FIG. 9. Strain-gauge drag balance with exit flow and base-pressure Pitot-tube racks.
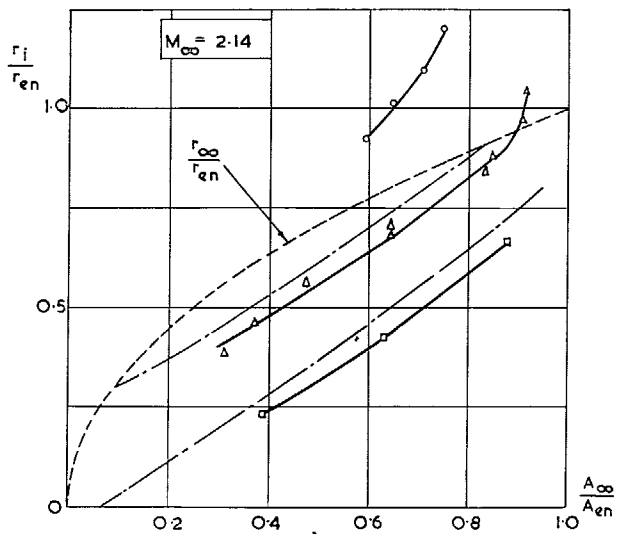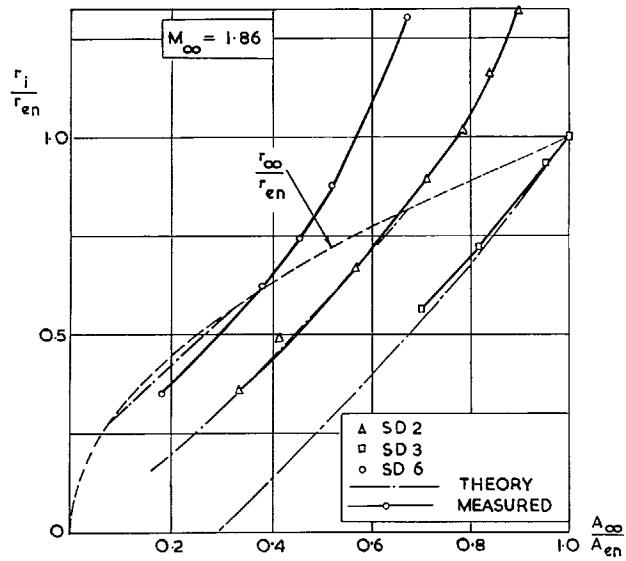
FIG. 10.   Comparison of measured and theoretical
values for r_i/r_{en}.
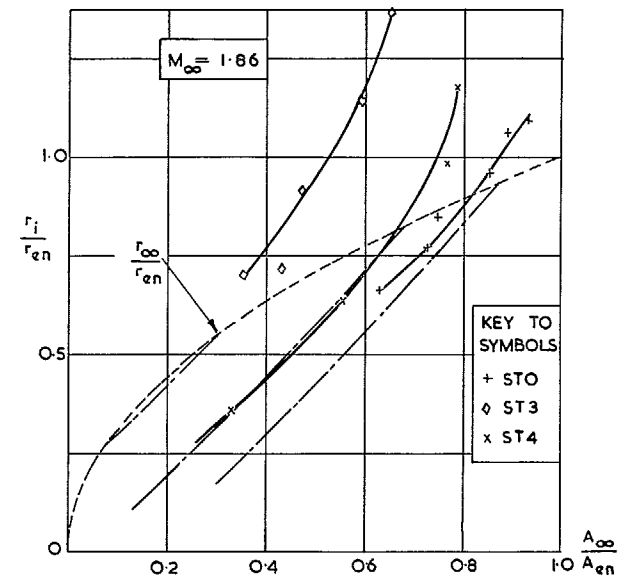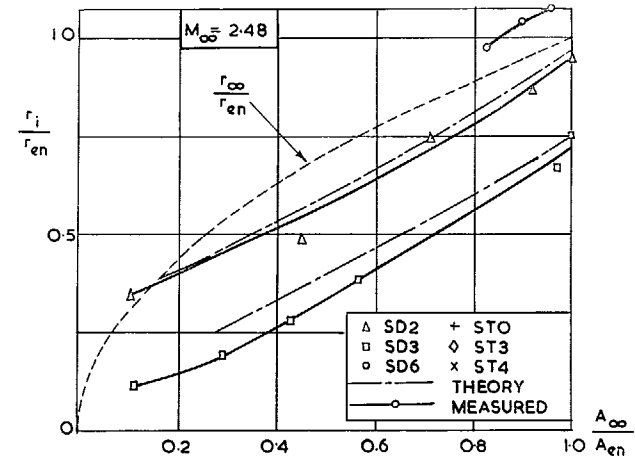
FIG. 11.   Comparison of measured and theoretical
values for r_i/r_{en}.
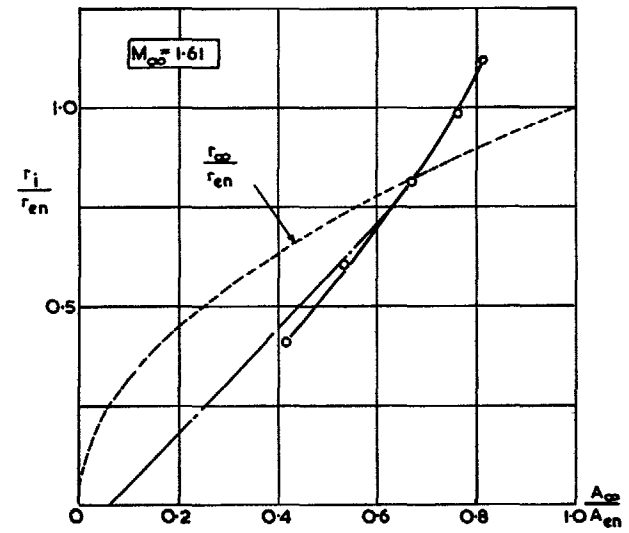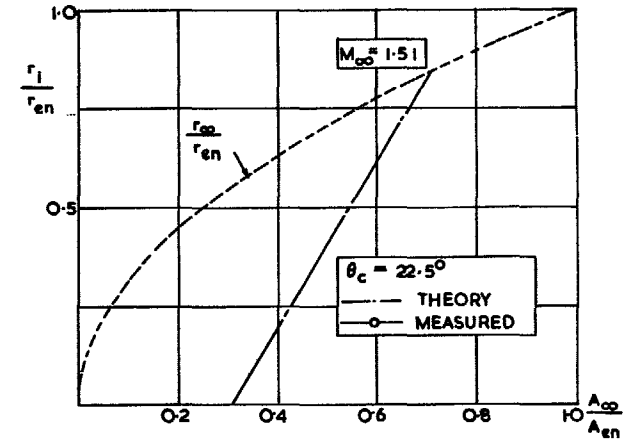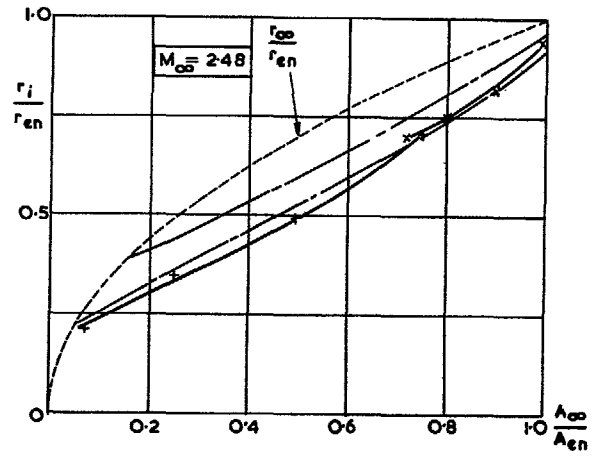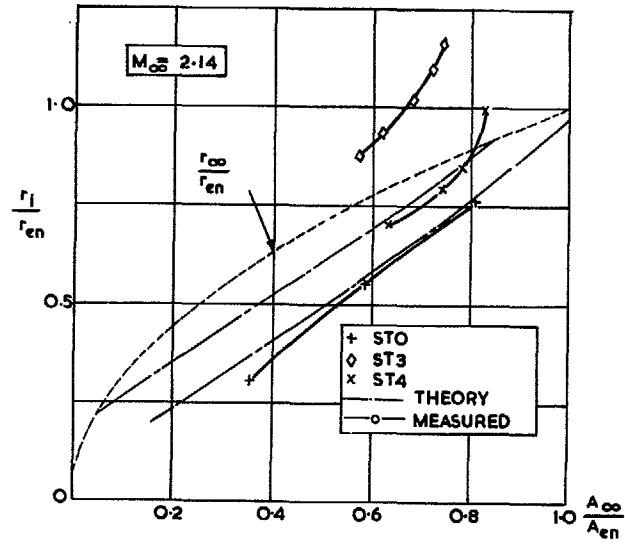
Fig. 12. Comparison of measured and theoretical values for r_i/r_{en}.

Fig. 13. Comparison of measured and theoretical values for r_i/r_{en}.
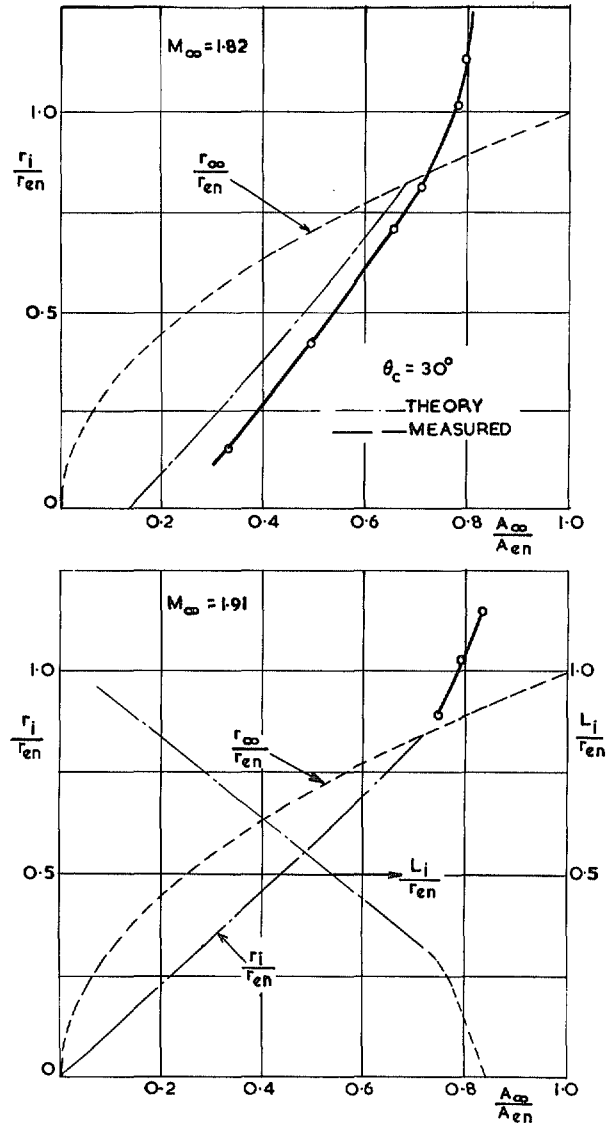
FIG. 14. Comparison of measured and theoretical values for r_i/r_{en}.
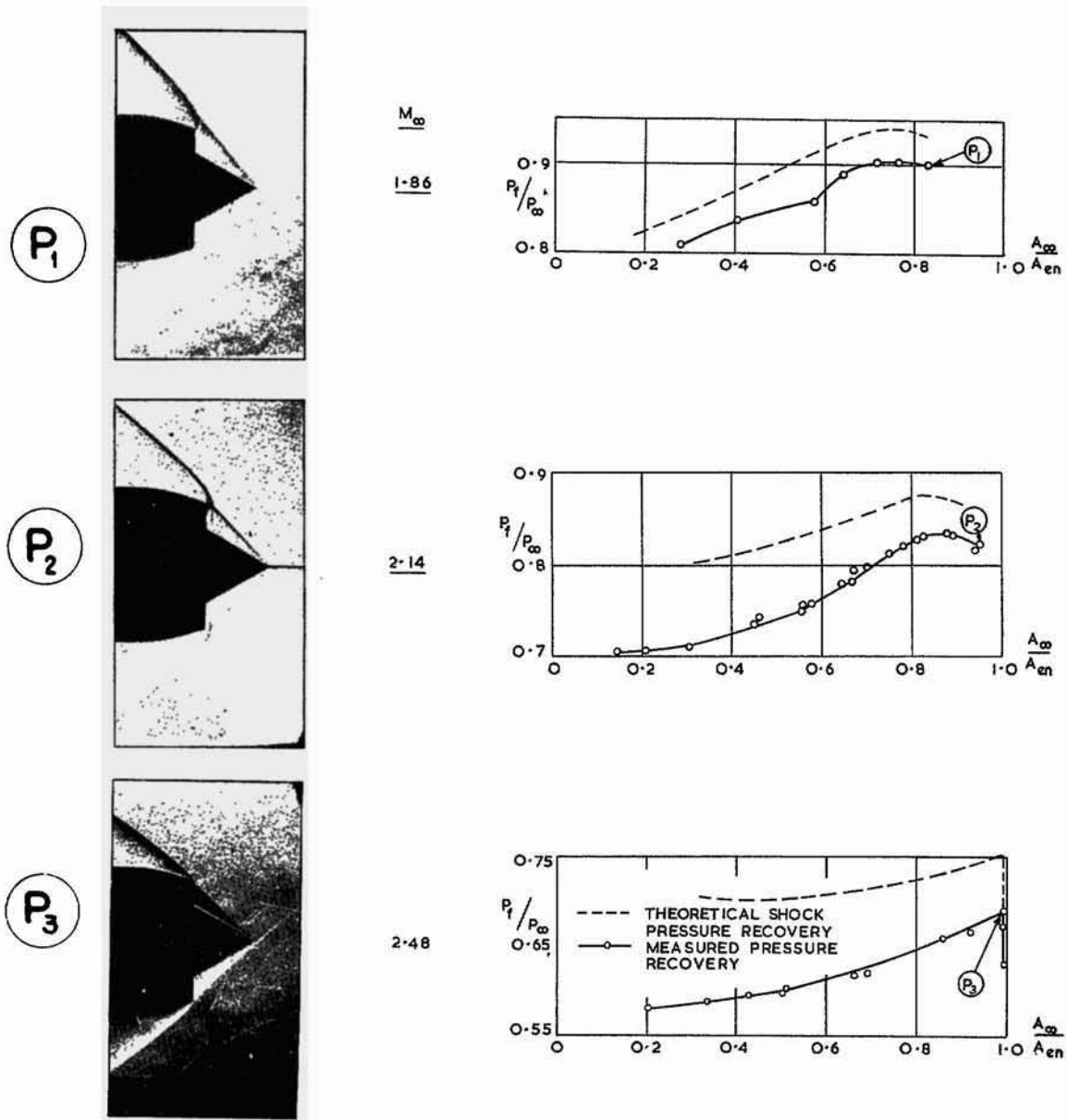
FIG. 15. Comparison of theoretical and experimental pressure recovery for model SD2 ($\theta_c = 30$ deg. $\theta_l = \theta_w$ at $M_\infty = 2 \cdot 34$).
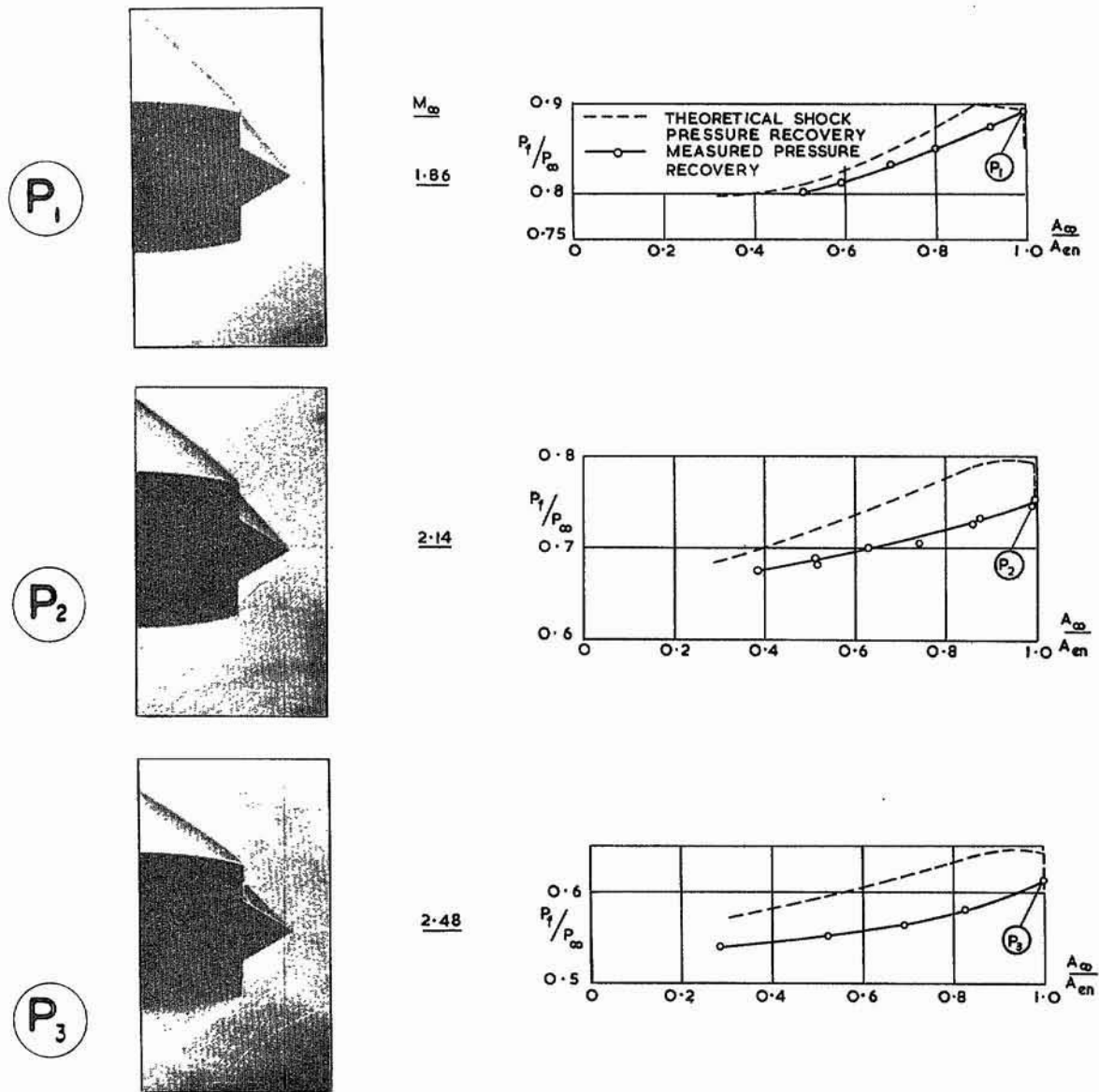
Fig. 16. Comparison of theoretical and experimental pressure recovery for model SD3
($\theta_c = 30$ deg. $\theta_l = \theta_w$ at $M_\infty = 1\cdot86$).
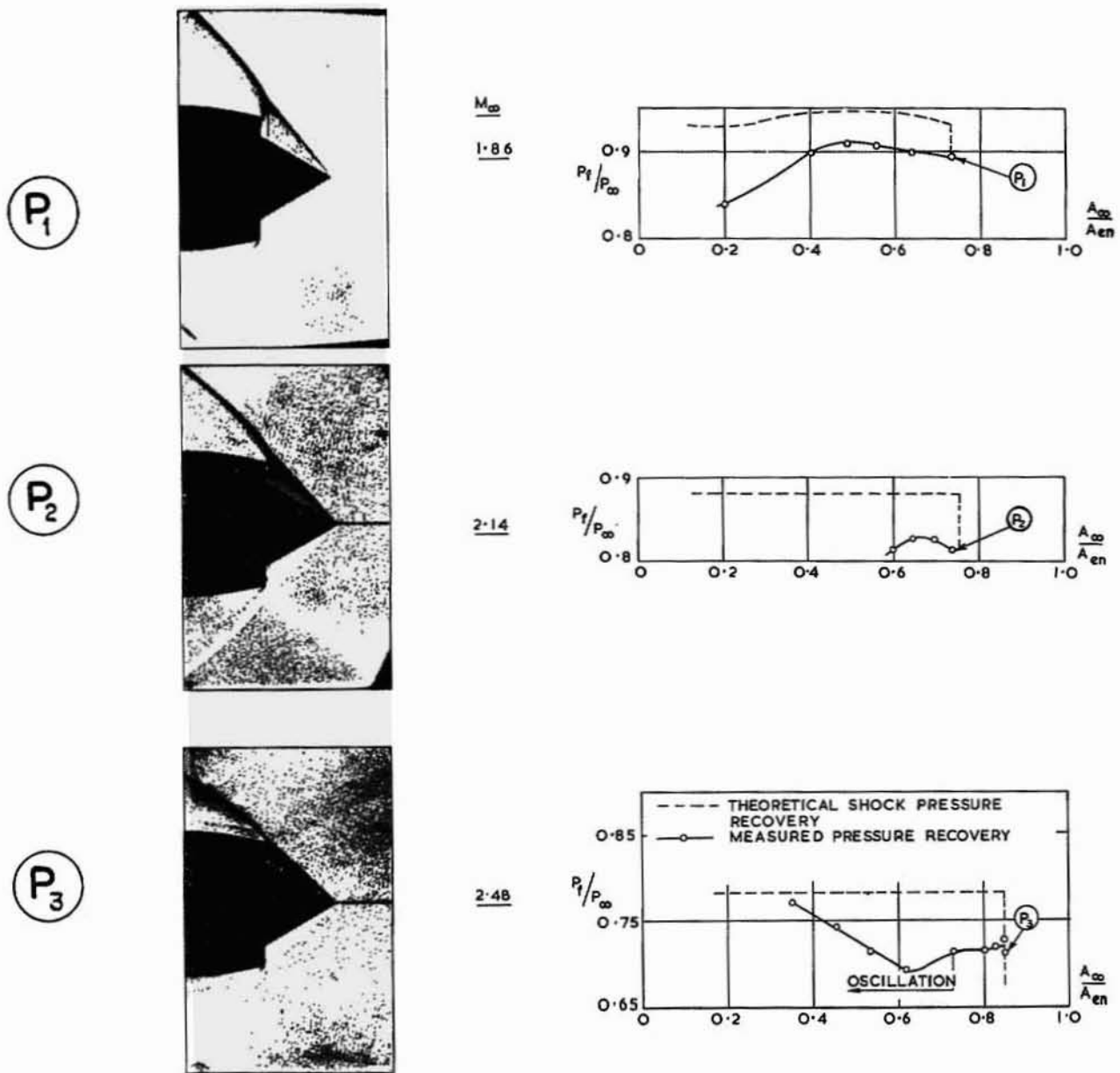
FIG. 17.   Comparison of theoretical and experimental pressure recovery for model SD6
$(\theta_c = 30$ deg. $\theta_l = \theta_w$ at $M_\infty = 2\cdot9)$.
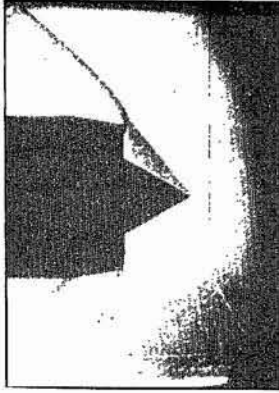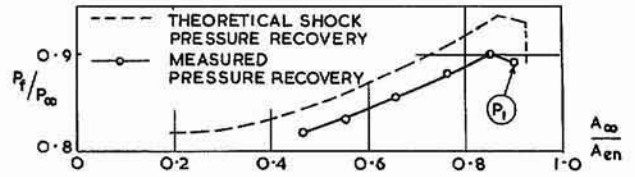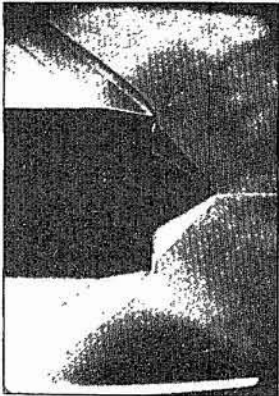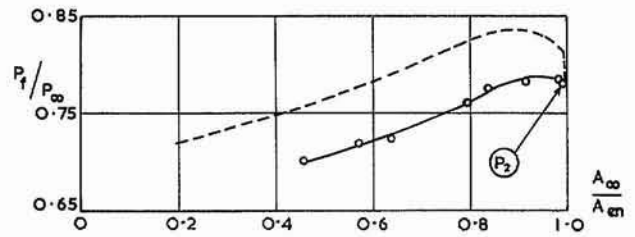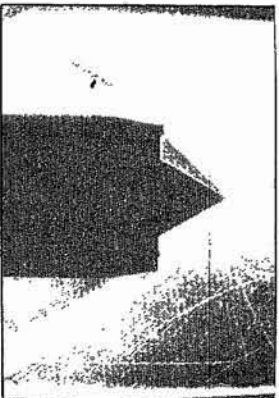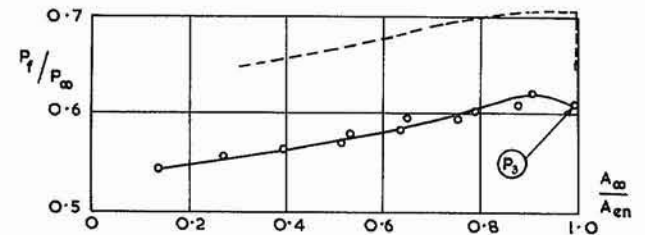
FIG. 18.   Comparison of theoretical and experimental pressure recovery for model ST0
($\theta_c = 30$ deg. $\theta_l = \theta_w$ at $M_\infty = 2 \cdot 05$).
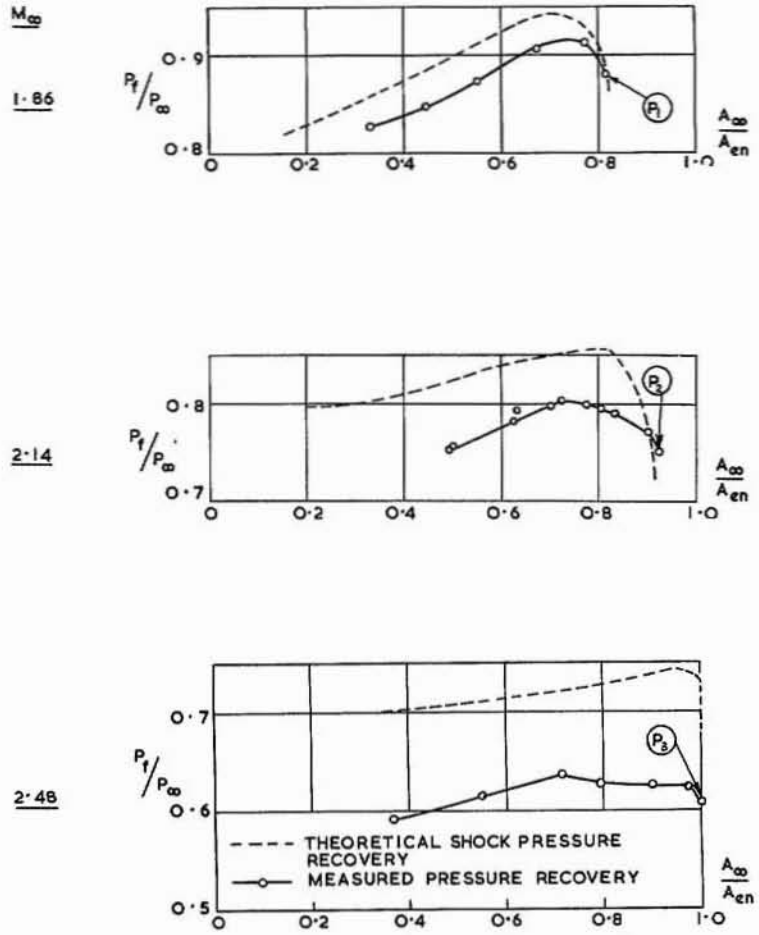
FIG. 19. Comparison of theoretical and experimental pressure recovery for model ST4
$(\theta_c = 30$ deg. $\theta_l = \theta_w$ at $M_\infty = 2 \cdot 34)$.
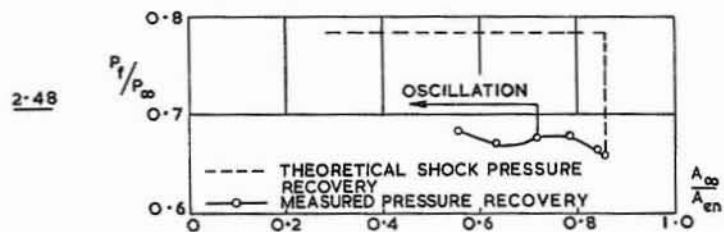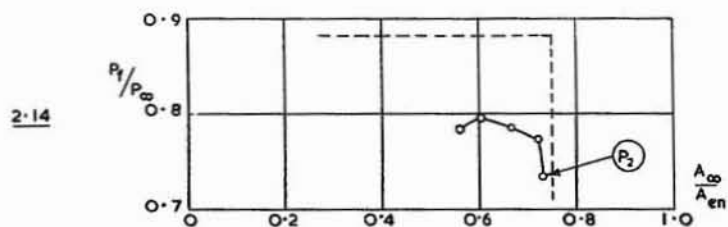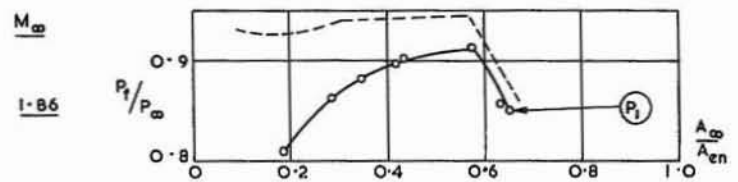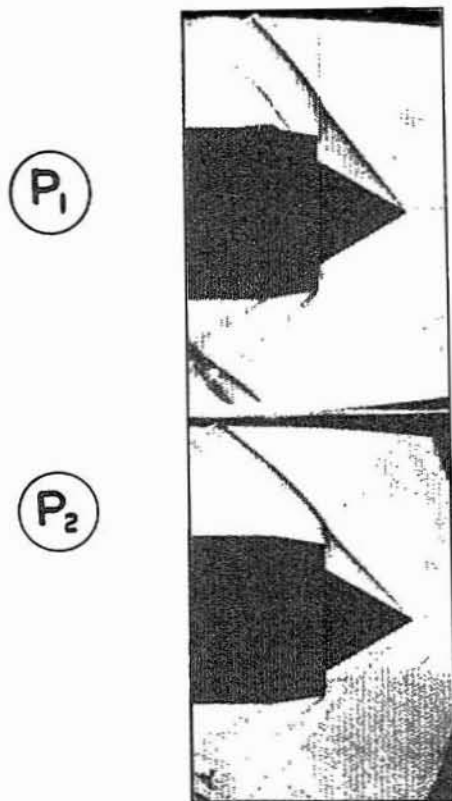
FIG. 20. Comparison of theoretical and experimental pressure recovery for model ST3
$(\theta_c = 30 \text{ deg. } \theta_l = \theta_w \text{ at } M_\infty = 2\cdot9)$.
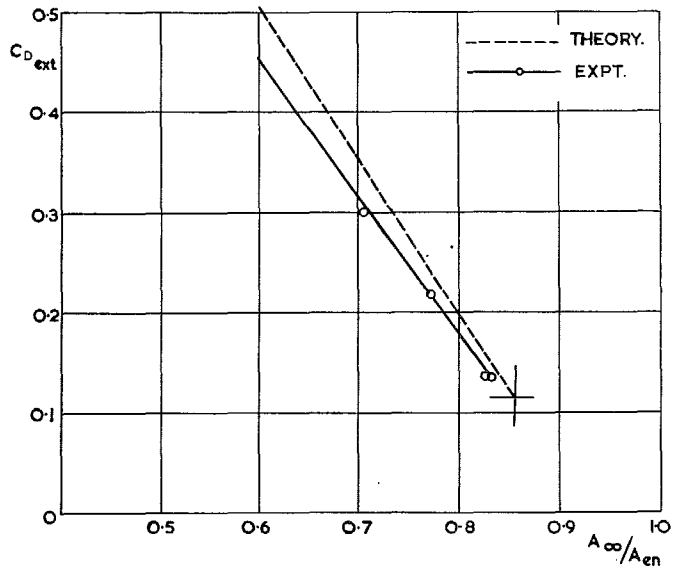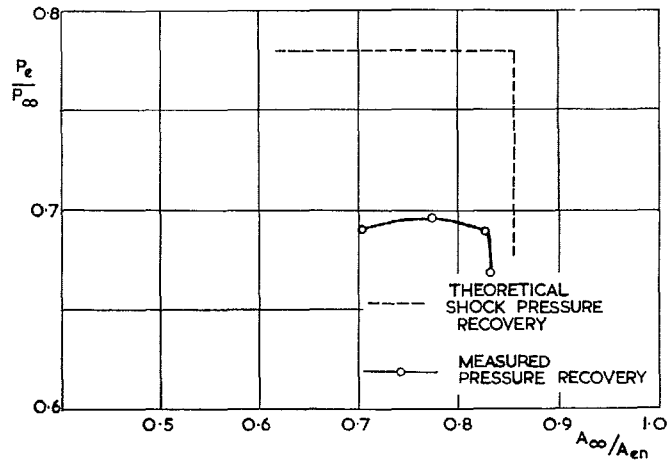
FIG. 21. Pressure recovery and drag of SD6 at $M_x = 2 \cdot 14$.
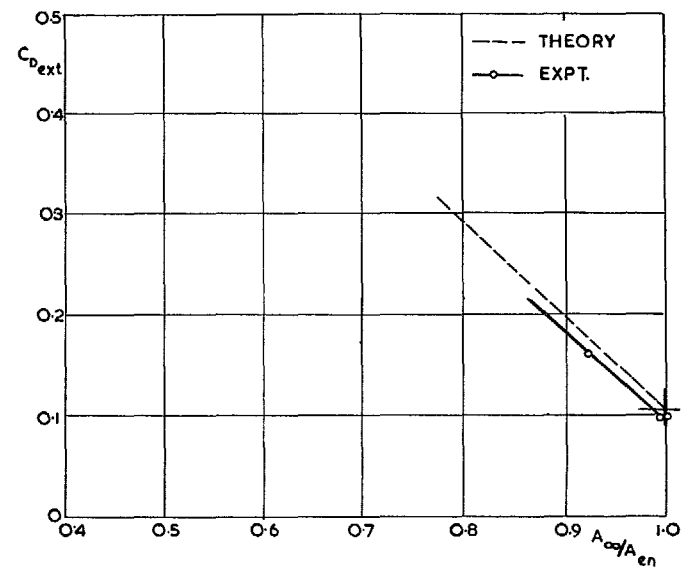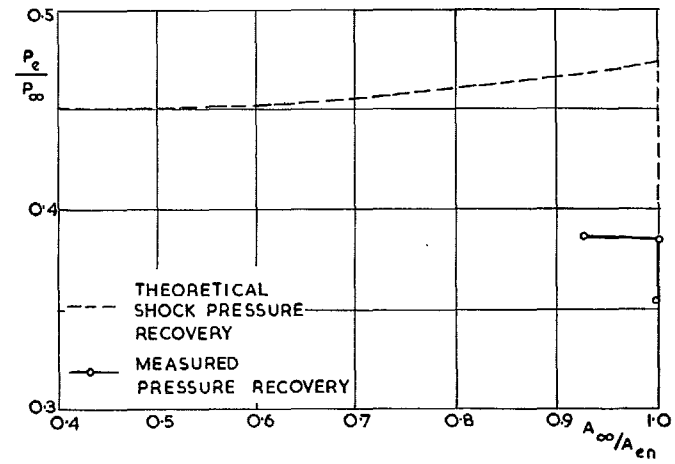
FIG. 22. Pressure recovery and drag of SD6 at $M_\infty = 2 \cdot 48$.
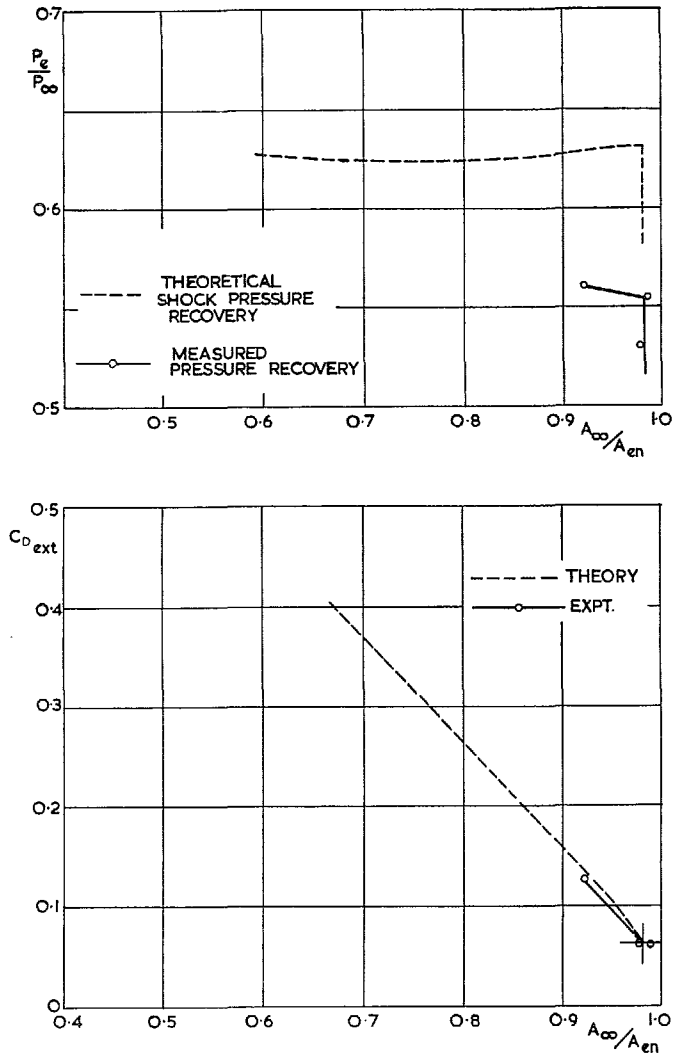
FIG. 23.   Pressure recovery and drag of SD6 at $M_\infty = 2 \cdot 90$.
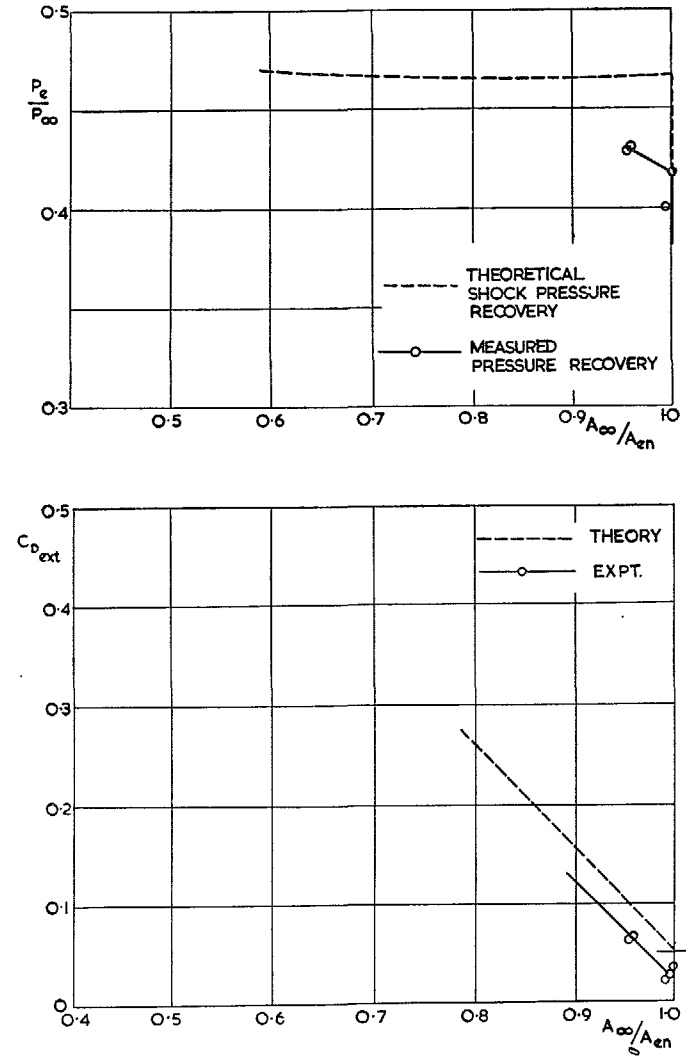
FIG. 24.   Pressure recovery and drag of SD6 at $M_\infty = 3 \cdot 27$.
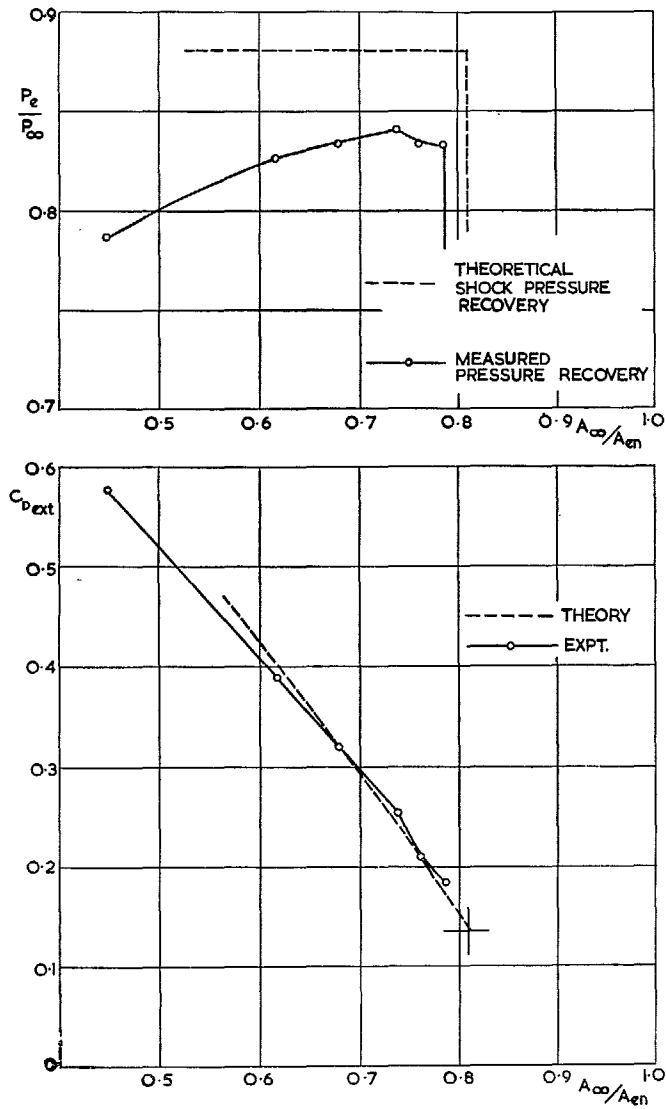
FIG. 25.   Pressure recovery and drag of
SD6 (— 0·05 in.) at $M_\infty = 2·14$.
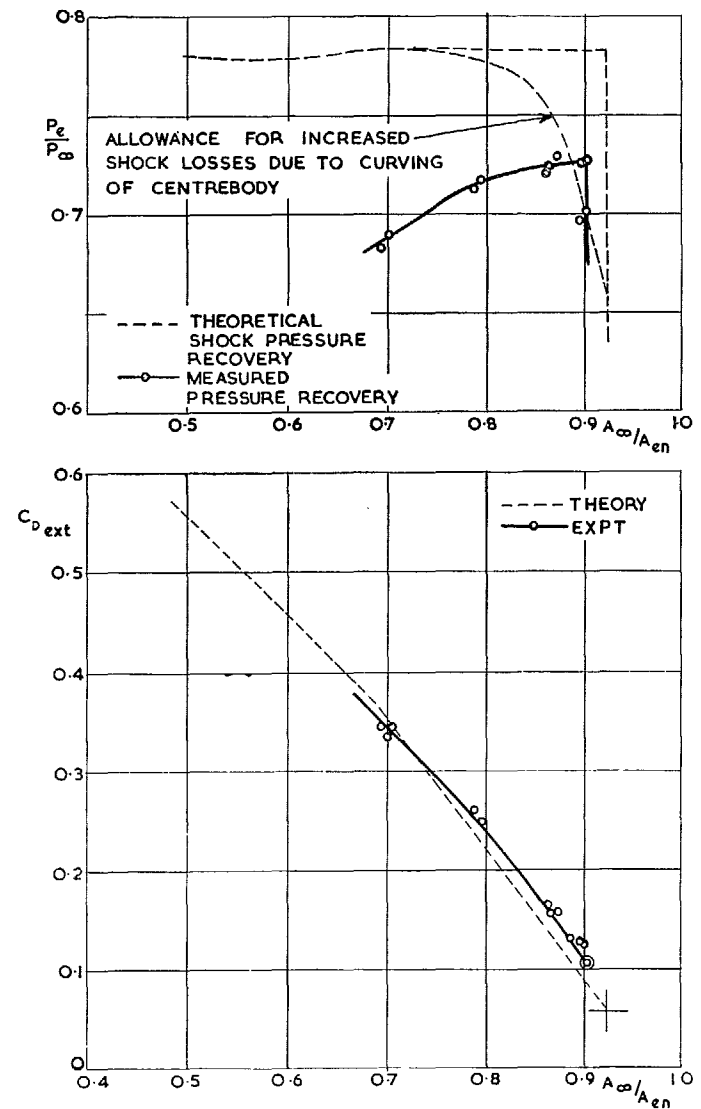
FIG. 26.   Pressure recovery and drag of
SD6 (— 0·05 in.) at $M_\infty = 2·48$.
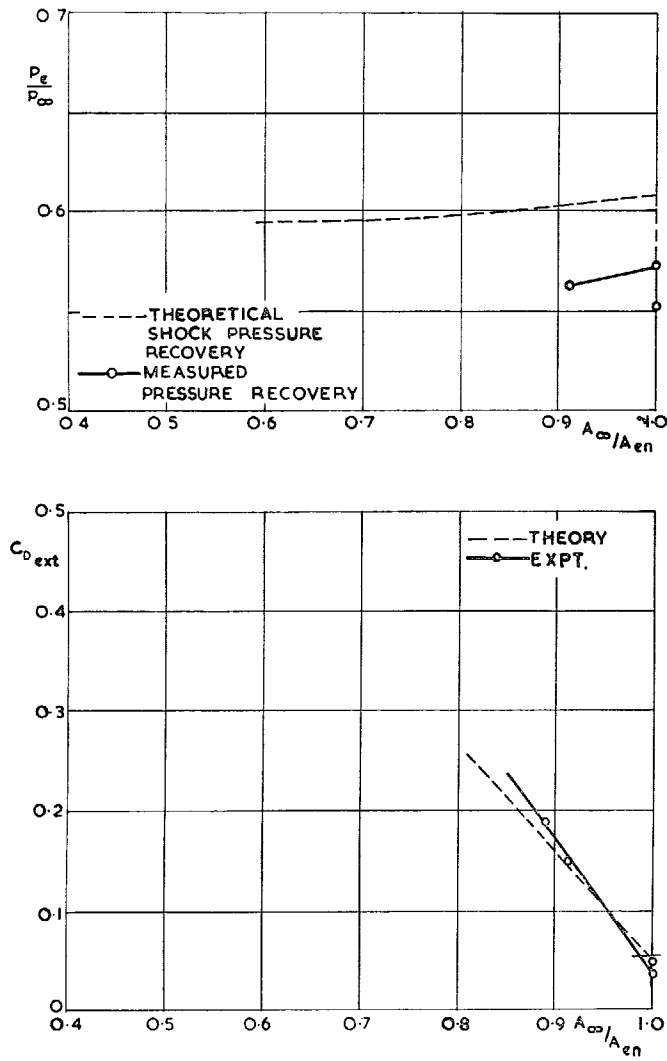
FIG. 27.   Pressure recovery and drag of
SD6 (— 0·05 in.) at $M_x = 2·90$.
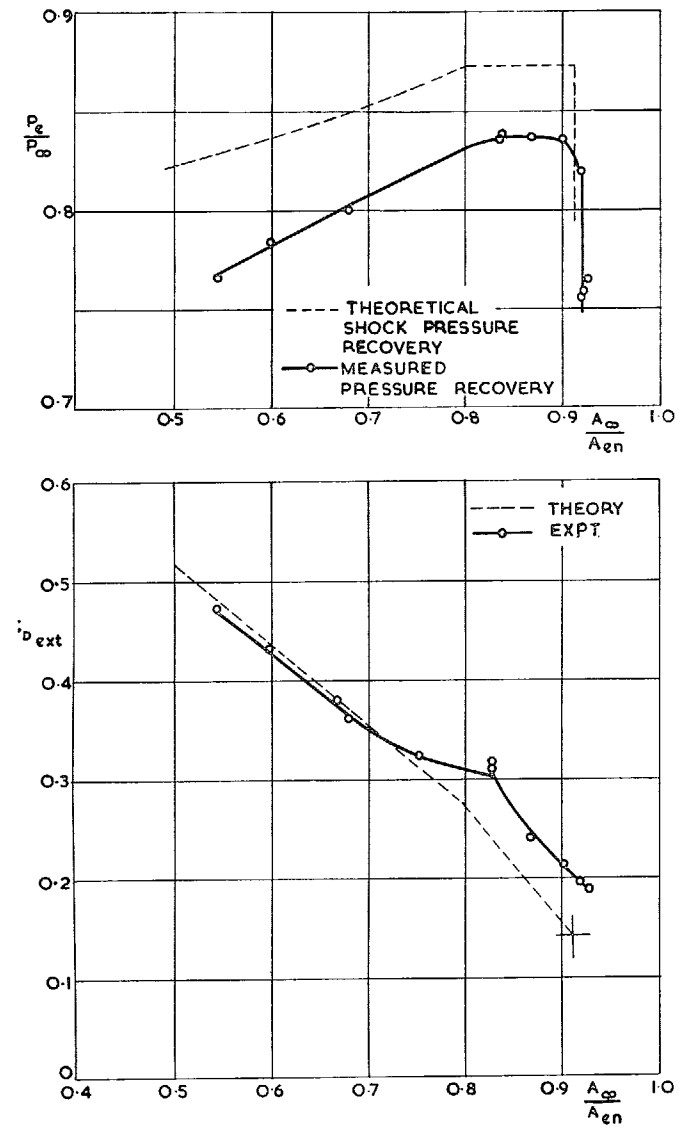
FIG. 28.   Pressure recovery and drag of SD2 at $M_x = 2·14$.
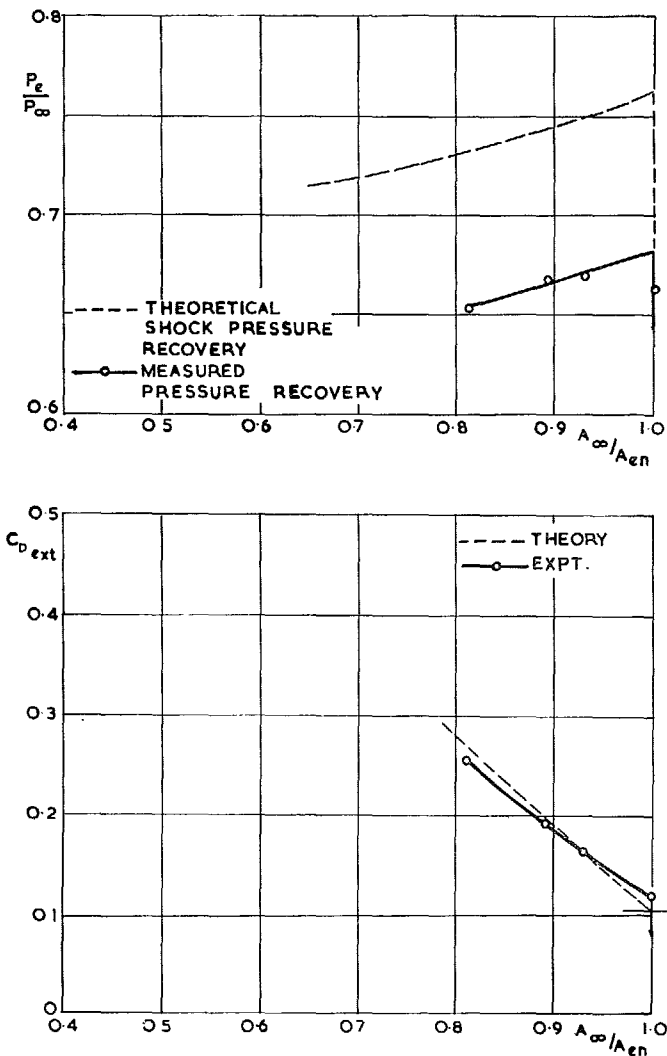
FIG. 29.   Pressure recovery and drag of SD2 at $M_\infty = 2\cdot48$.
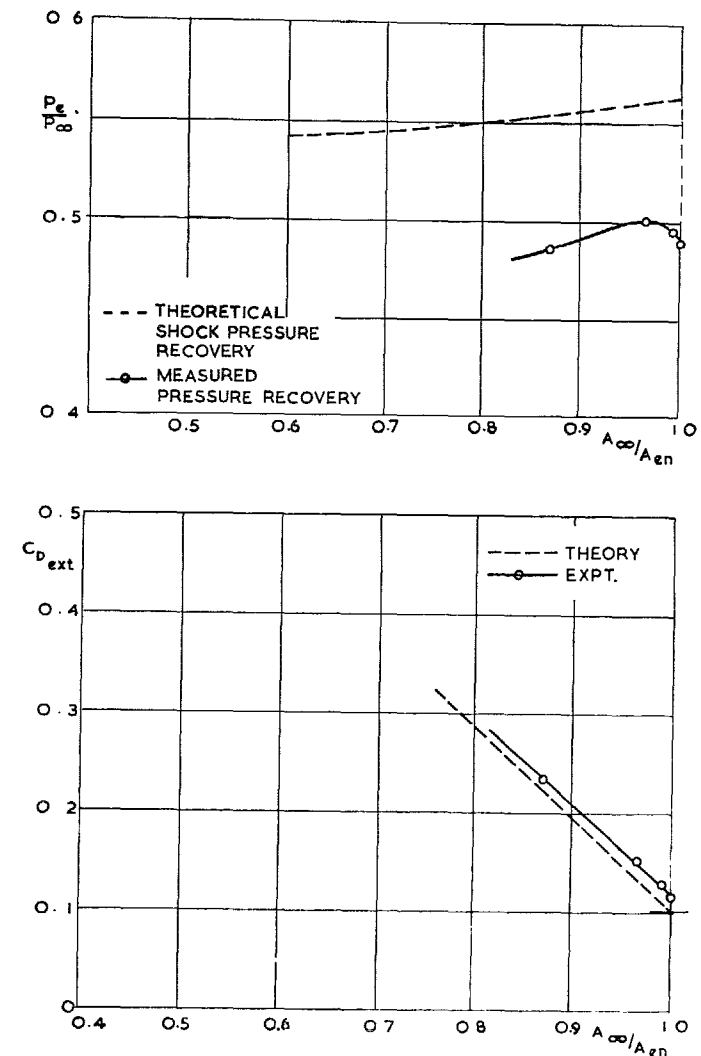
FIG. 30.   Pressure recovery and drag of SD2 at $M_\infty = 2\cdot90$.

37
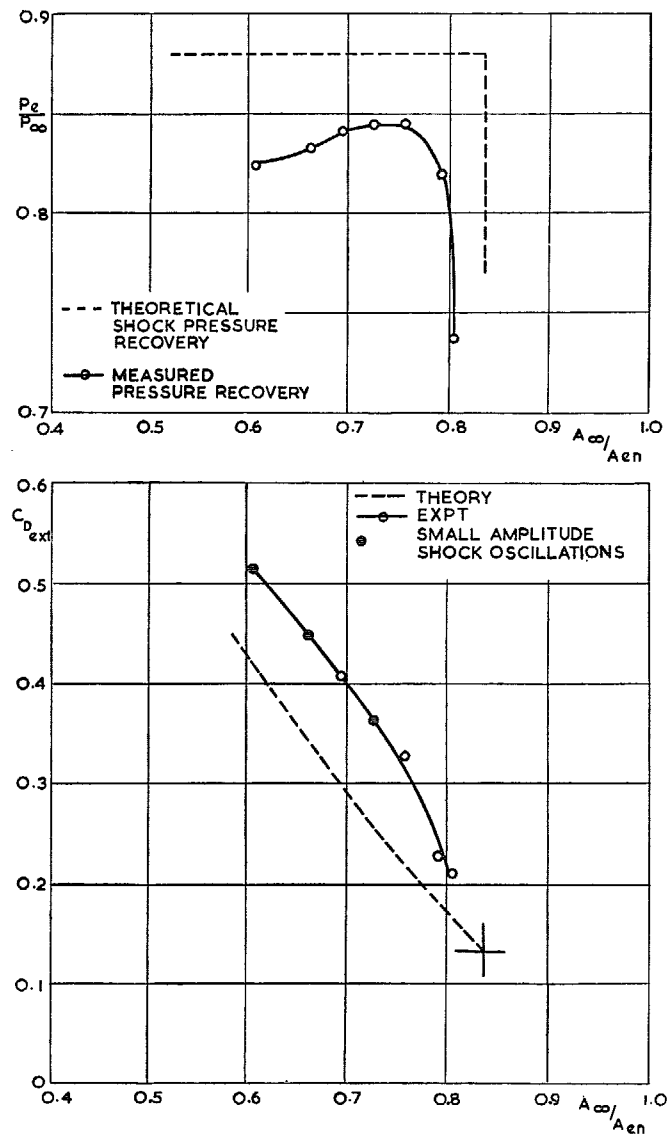
FIG. 31.   Pressure recovery and drag of
ST3 (— 0·05 in.) at $M_\infty = 2·14$.
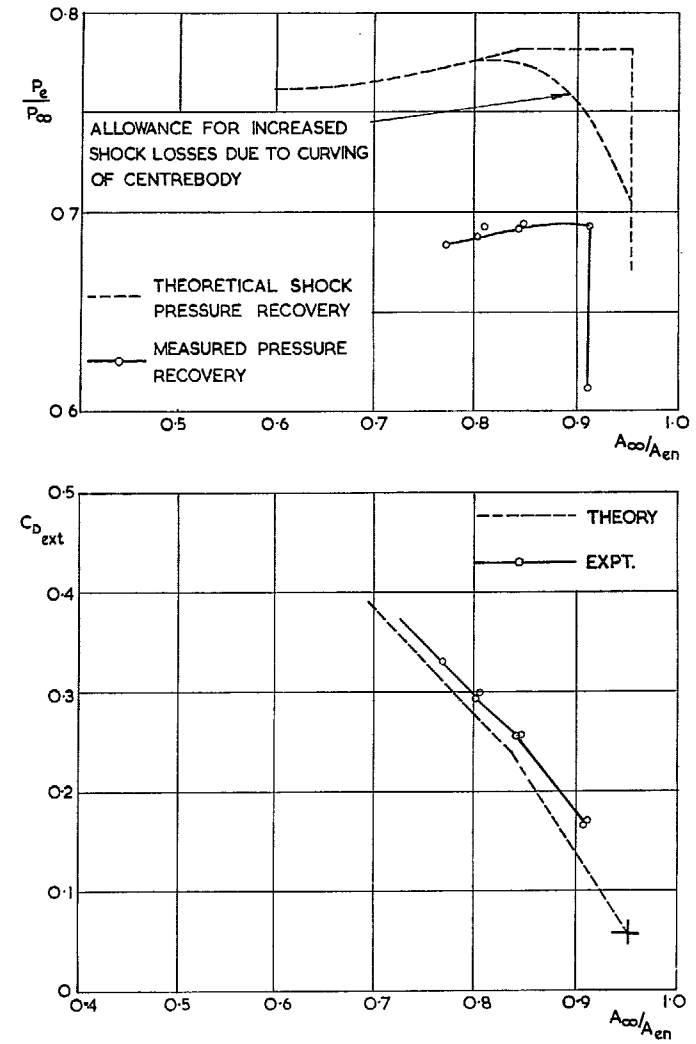
FIG. 32.   Pressure recovery and drag of
ST3 (— 0·05 in.) at $M_x = 2·48$.
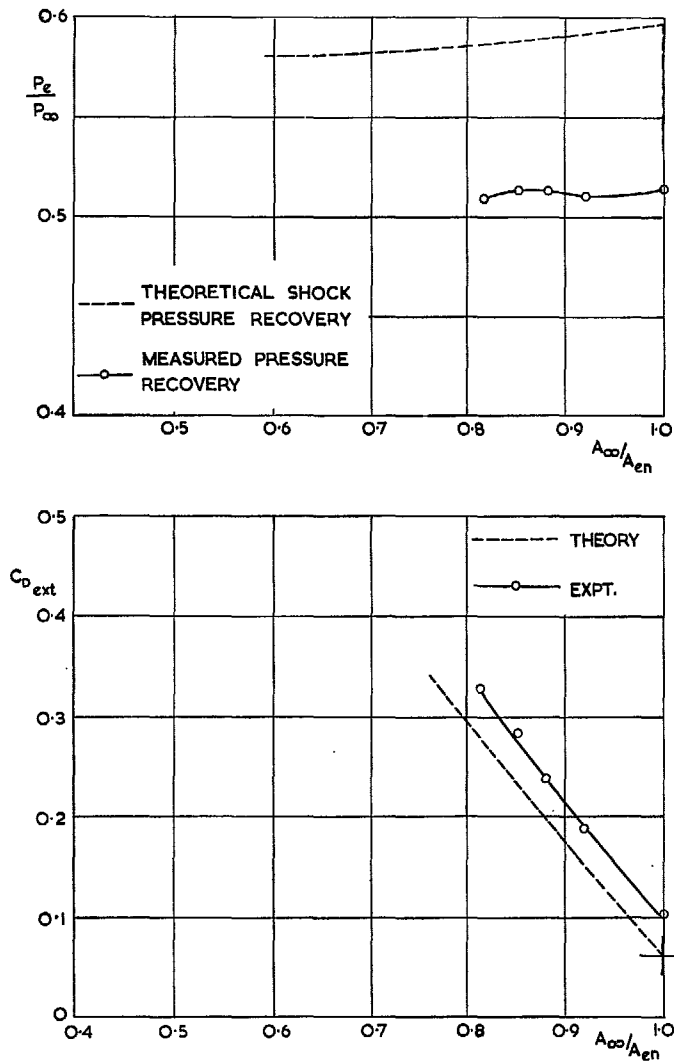
FIG. 33.   Pressure recovery and drag of
ST3 (— 0·05 in.) at $M_x = 2·90$.
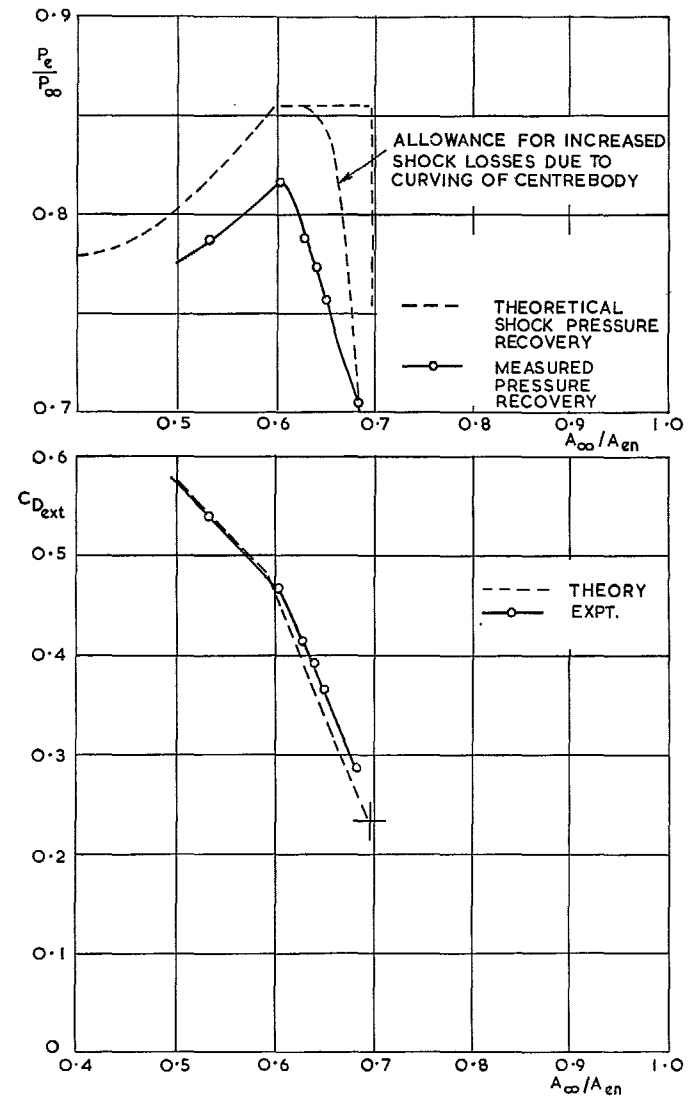
FIG. 34.   Pressure recovery and drag of
35 deg III at $M_\infty = 2·14$.
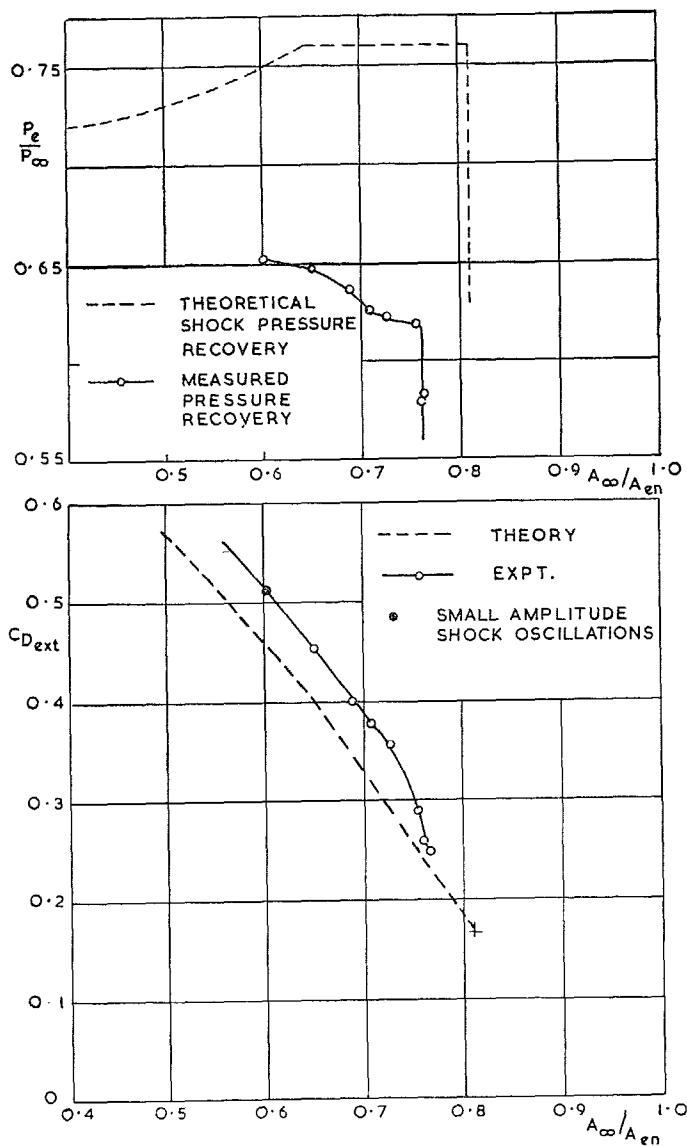
FIG. 35. Pressure recovery and drag of
35 deg III at $M_\infty = 2 \cdot 48$.
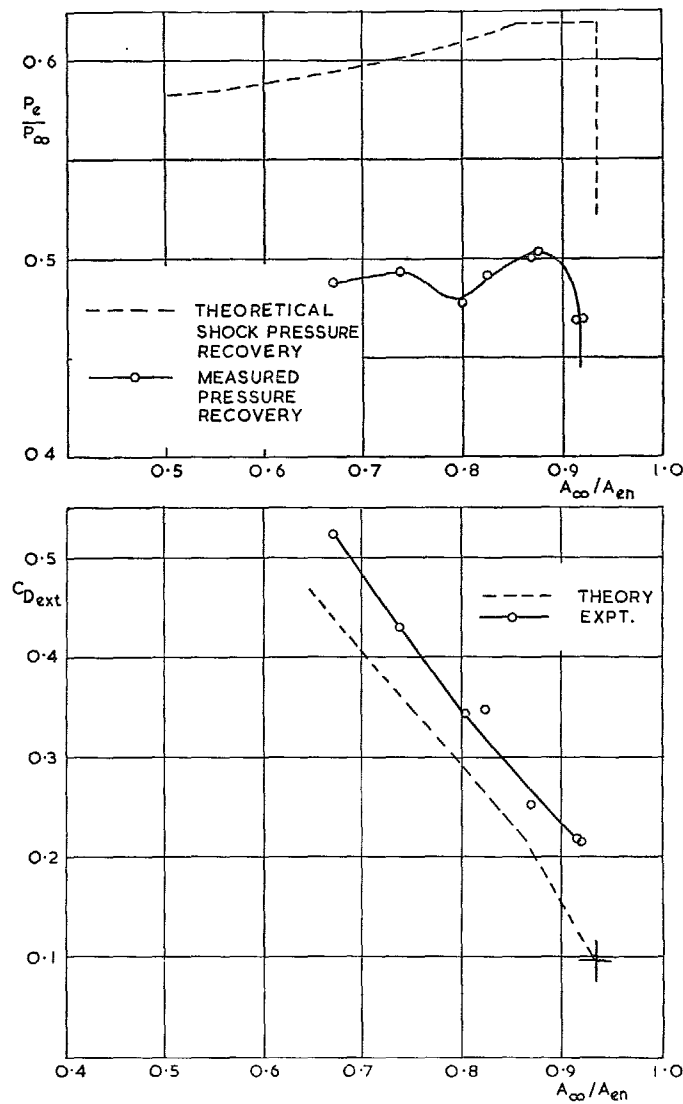
FIG. 36. Pressure recovery and drag of
35 deg III at $M_\infty = 2 \cdot 90$.
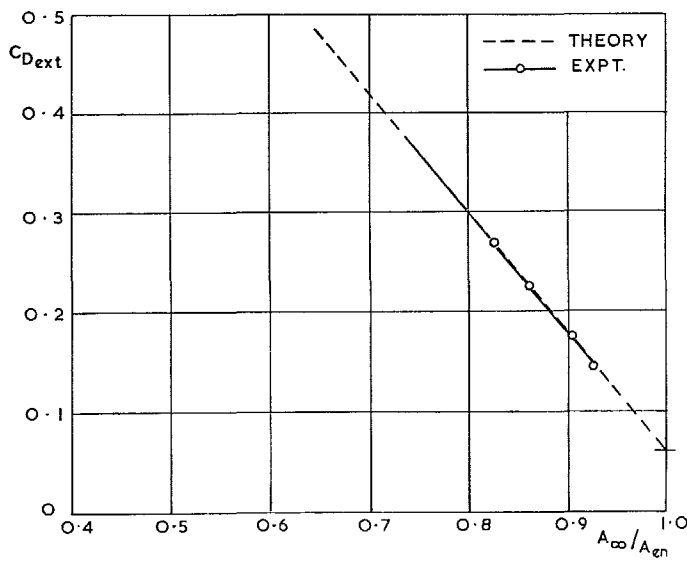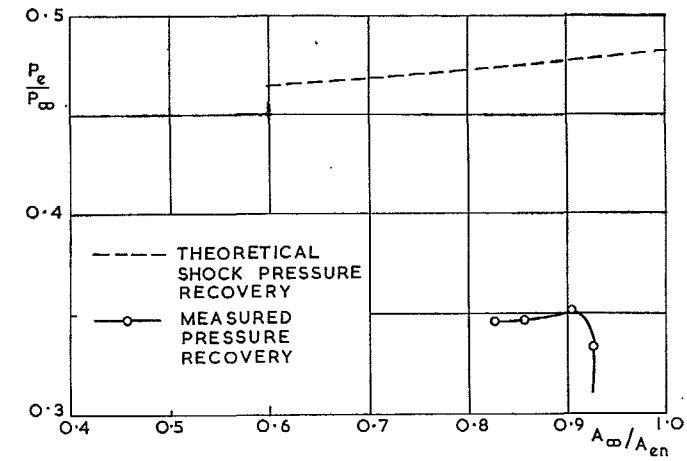
FIG. 37. Pressure recovery and drag of
35 deg III at $M_\infty = 3\cdot27$.
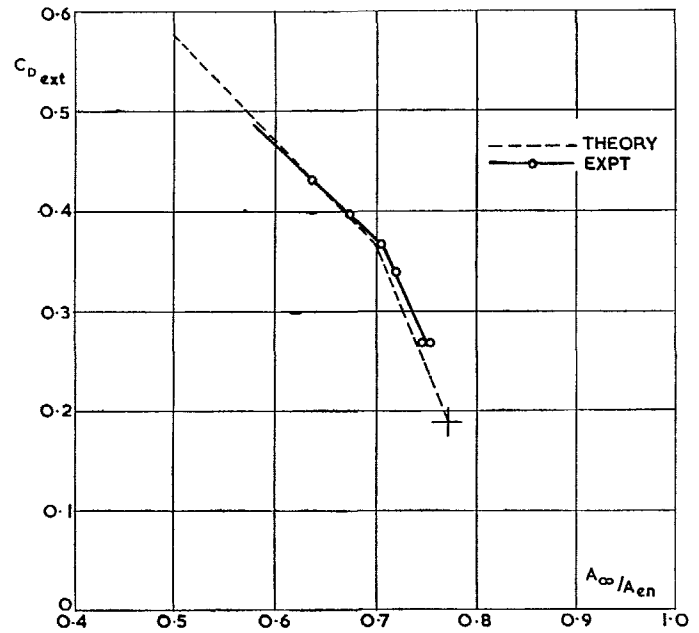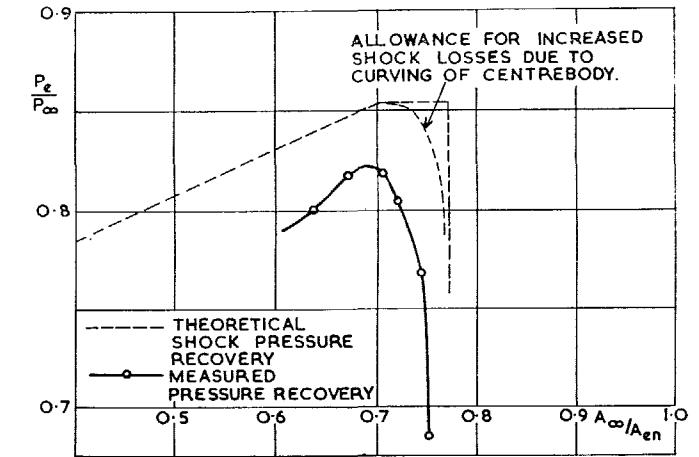
FIG. 38. Pressure recovery and drag of 35 deg III
(— 0·05 in.) at $M_\infty = 2\cdot14$.
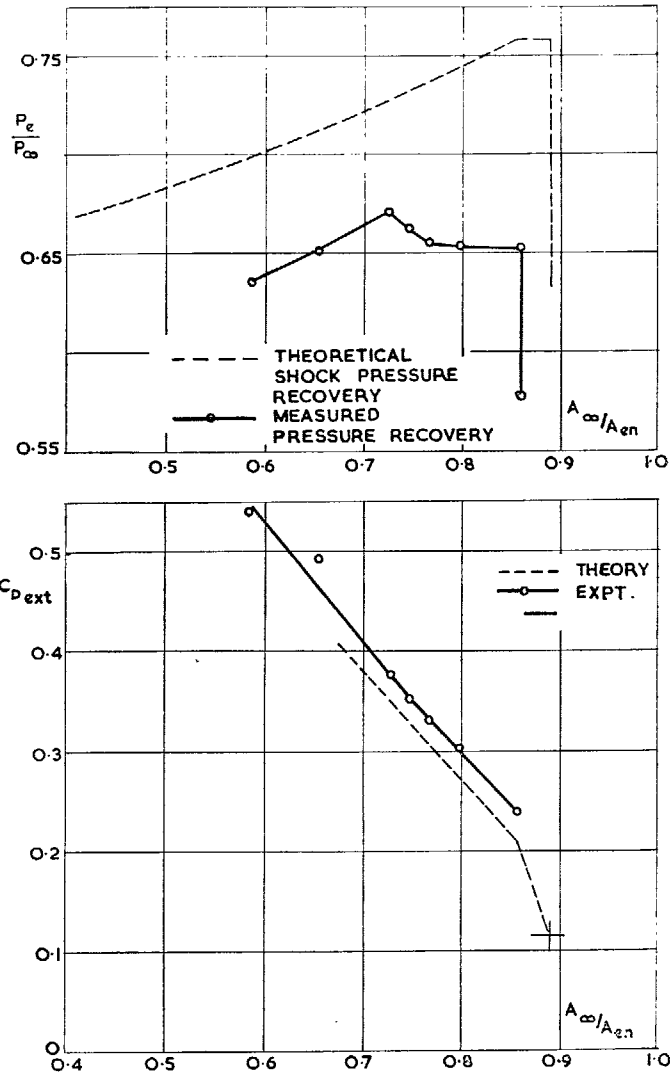
FIG. 39. Pressure recovery and drag of 35 deg III
(— 0·05 in.) at $M_\infty = 2·48$.
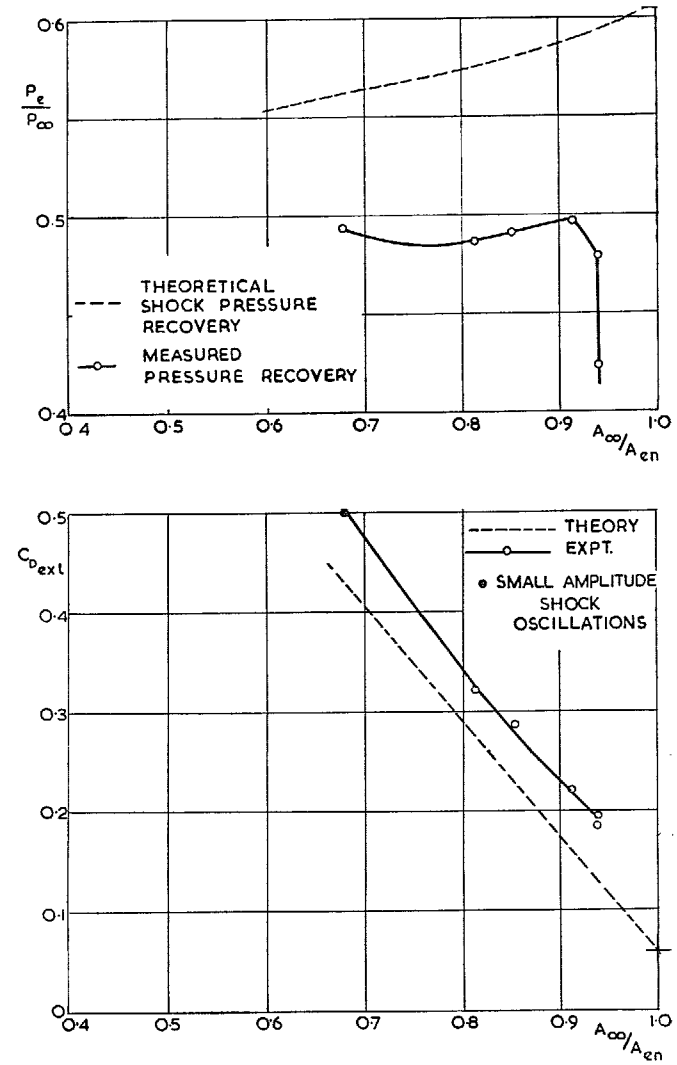
FIG. 40. Pressure recovery and drag of
35 deg III (— 0·05 in.) at $M_\infty = 2·90$.
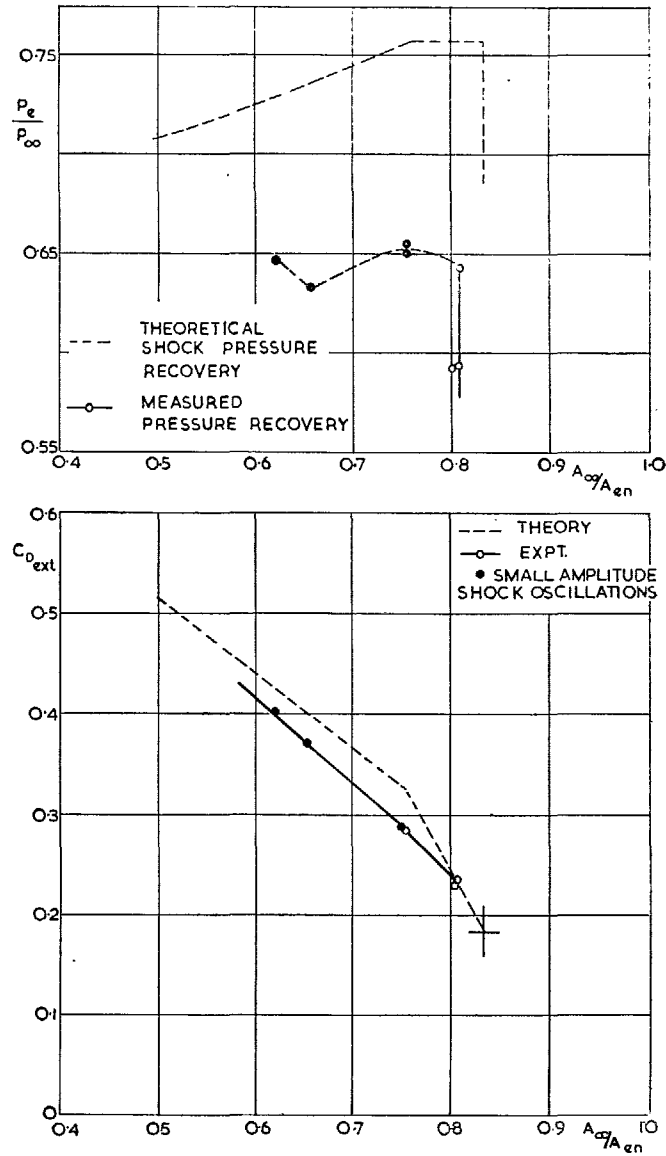
FIG. 41. Pressure recovery and drag of
35 deg I at $M_\infty = 2 \cdot 48$.
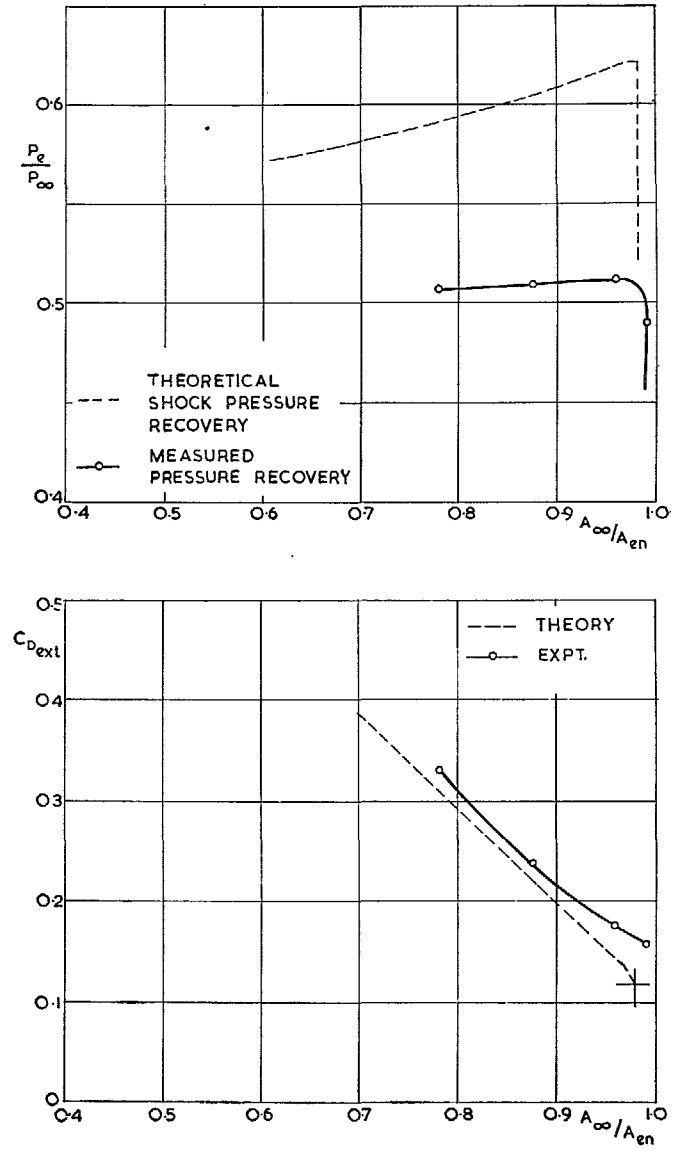
FIG. 42. Pressure recovery and drag of
35 deg I at $M_x = 2 \cdot 90$.
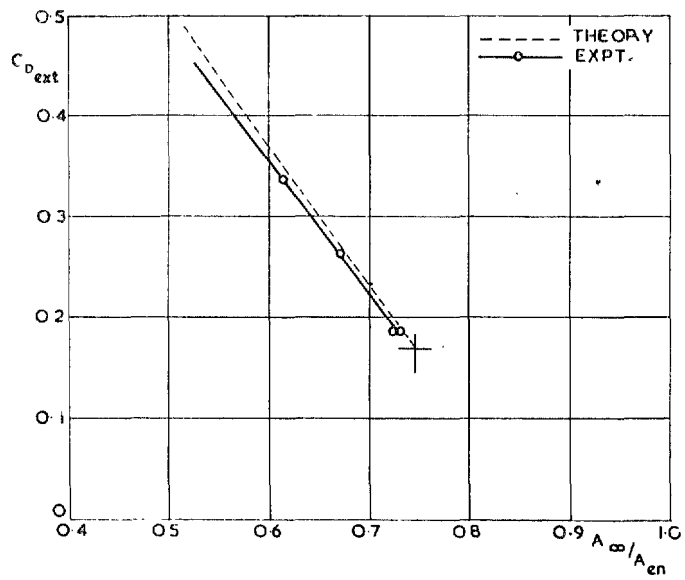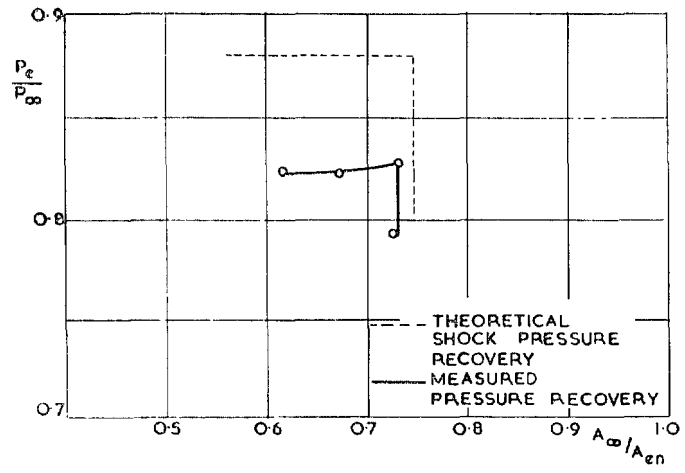
FIG. 43. Pressure recovery and drag of 35 deg I at $M_\infty = 3\cdot27$.
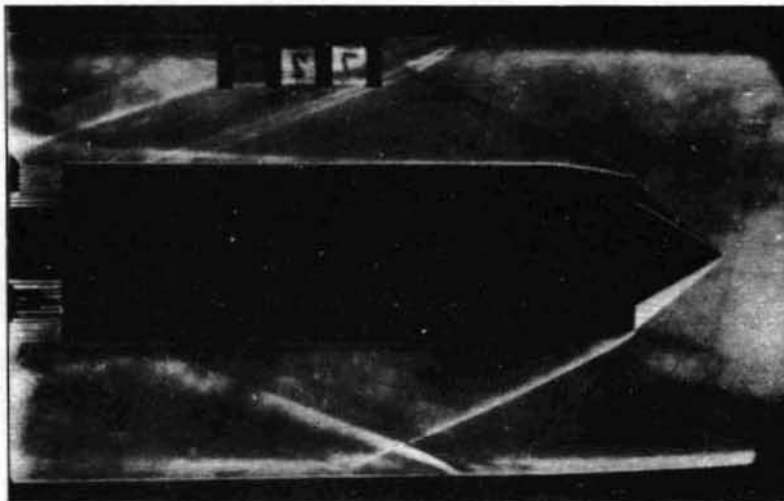
SD6

$M_\infty = 3.27$

$\dfrac{A_\infty}{A_{en}} = 1.00$

$\dfrac{P_e}{P_\infty} = 0.4005$

a
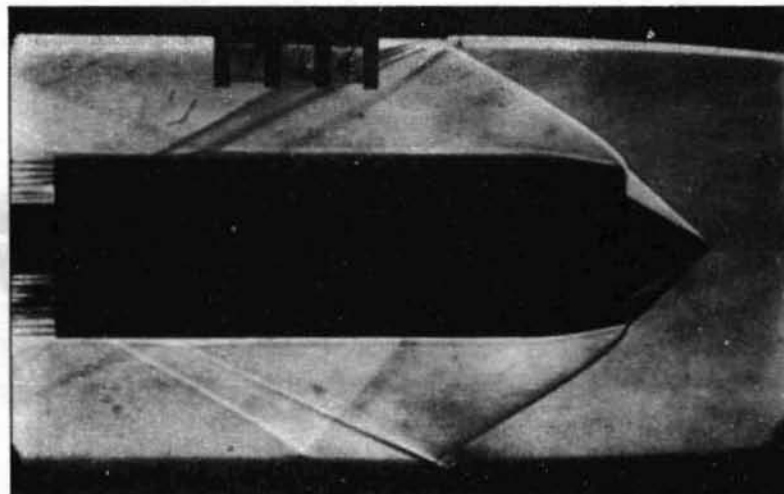
SD6 $(-0.05")$

$M_\infty = 2.48$

$\dfrac{A_\infty}{A_{en}} = 0.9019$

$\dfrac{P_e}{P_\infty} = 0.7269$

b
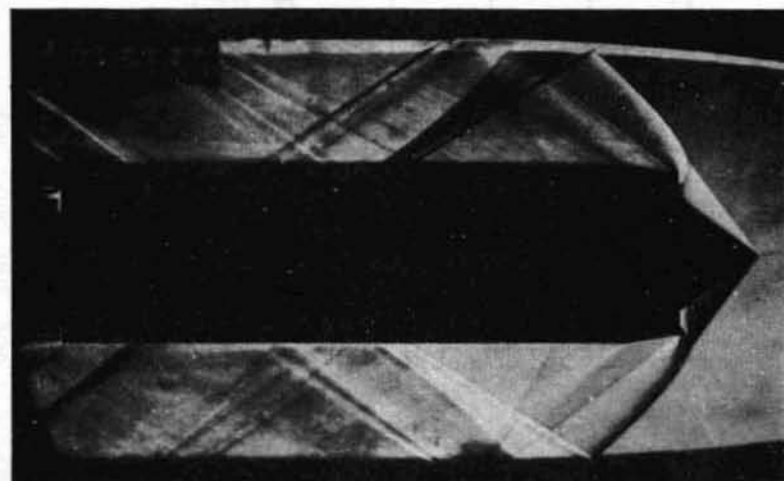
$35°$ III

$M_\infty = 2.14$

$\dfrac{A_\infty}{A_{en}} = 0.6811$

$\dfrac{P_e}{P_\infty} = 0.7054$

c

FIG. 44. Schlieren photographs.
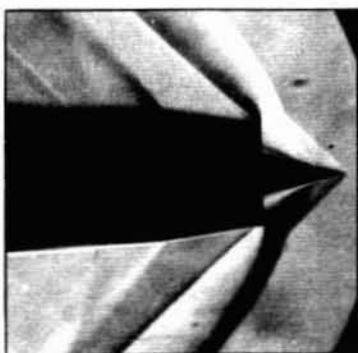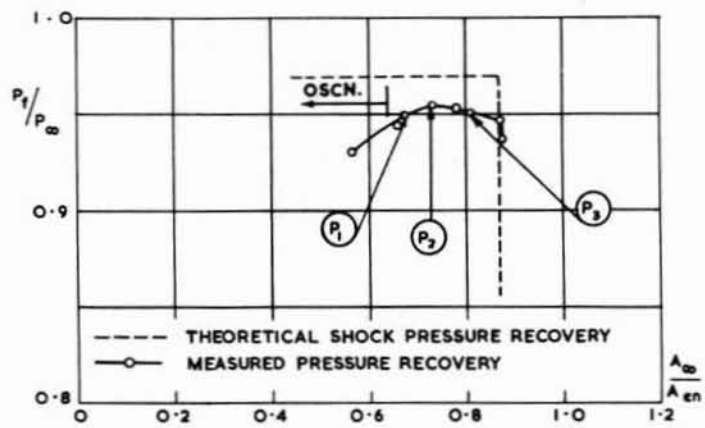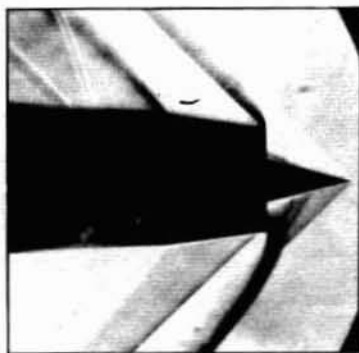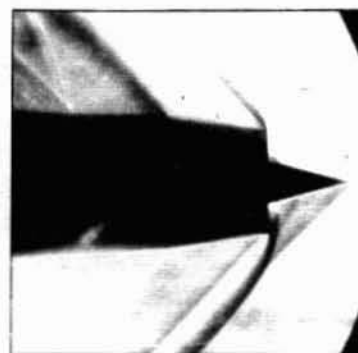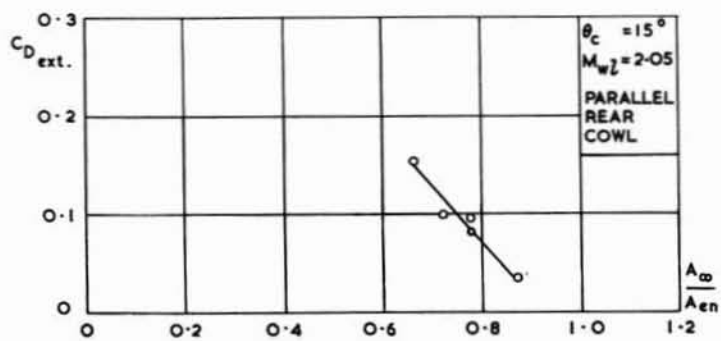
FIG. 45. Pressure recovery and drag at $M_\infty = 1 \cdot 51$ ($\theta_c = 15$ deg).
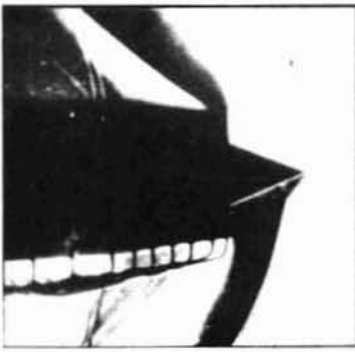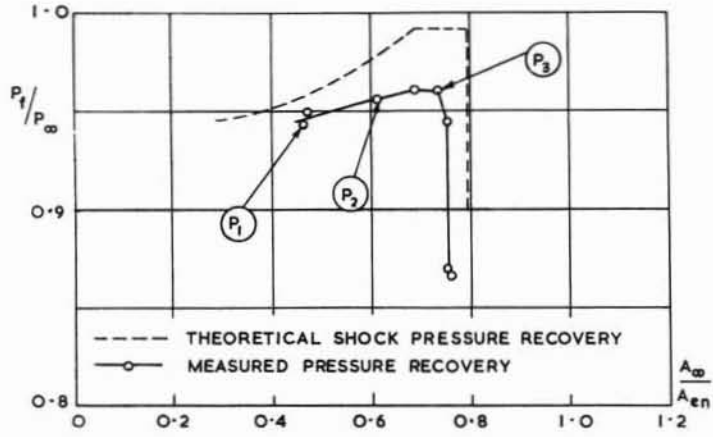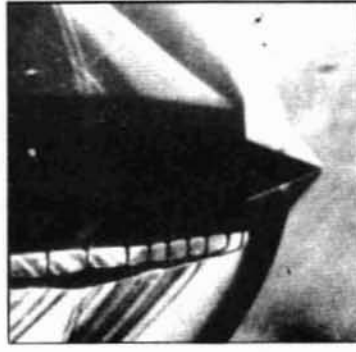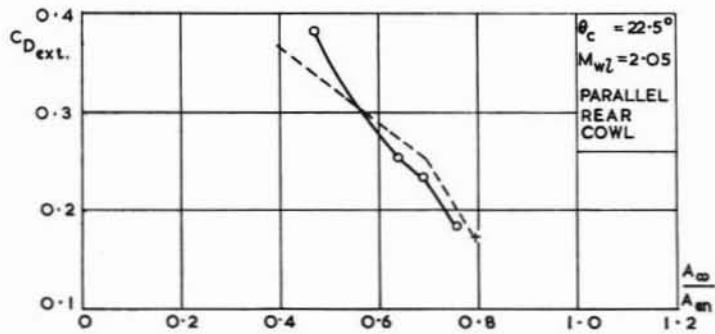
FIG. 46. Pressure recovery and drag at $M_\infty = 1\cdot51$ ($\theta_c = 22\cdot5$ deg).
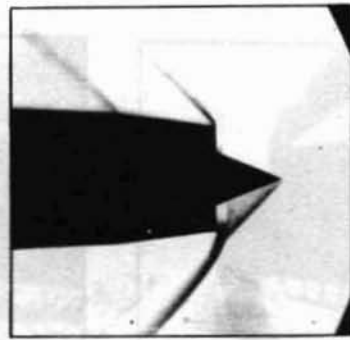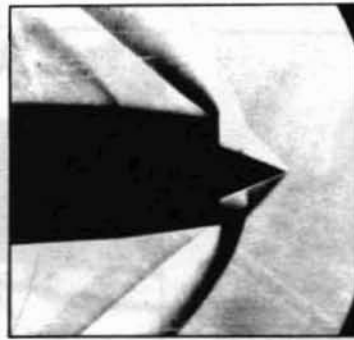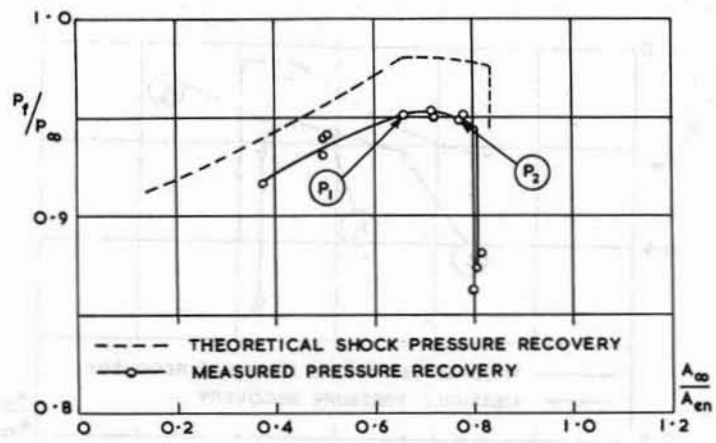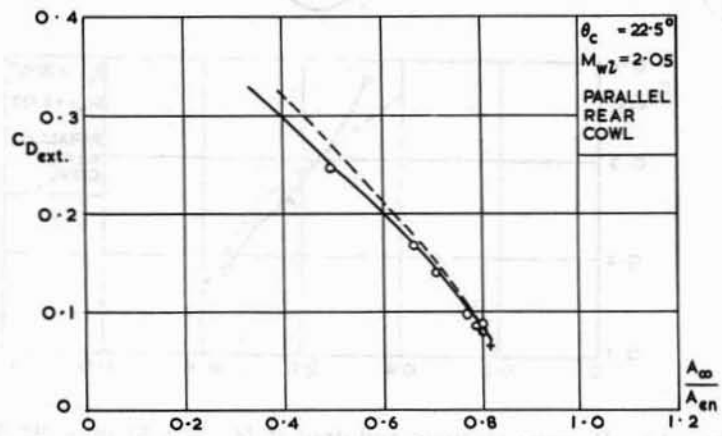
FIG. 47. Pressure recovery and drag at $M_\infty = 1 \cdot 61$ ($\theta_c = 22 \cdot 5$ deg).
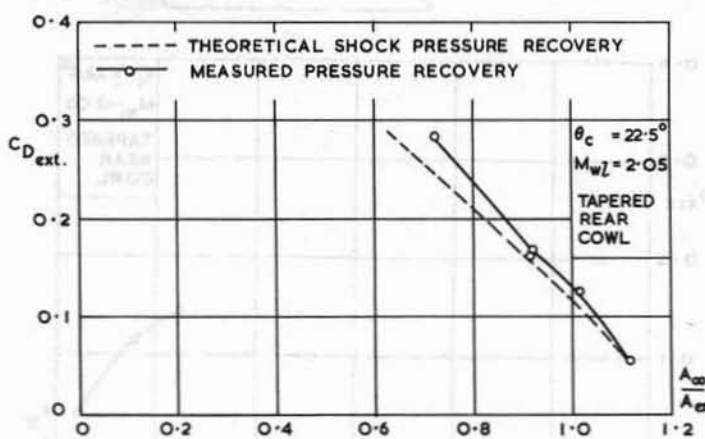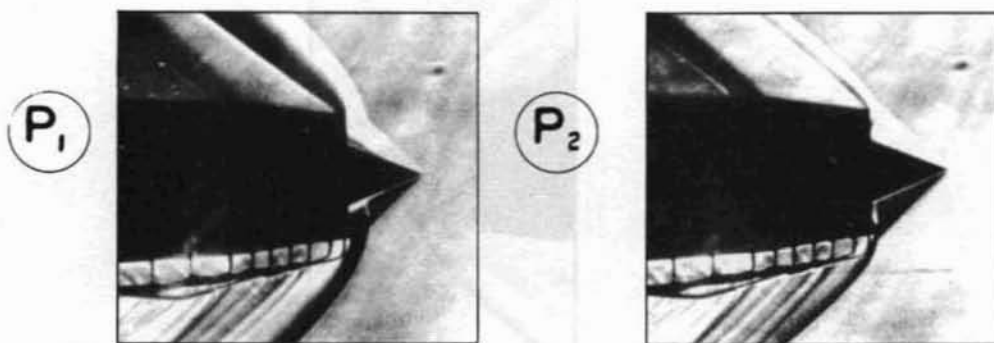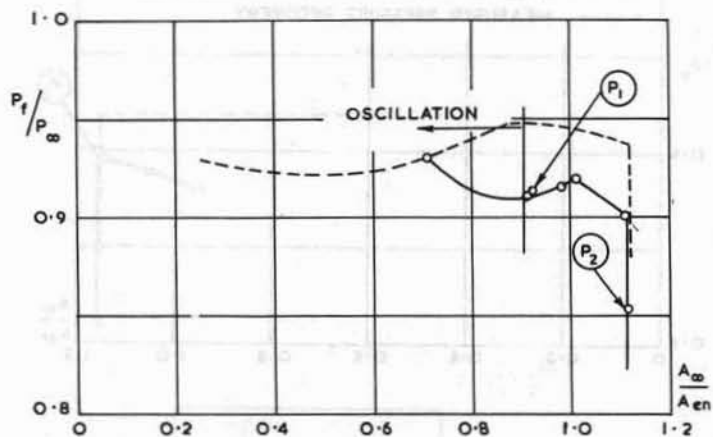
FIG. 48. Pressure recovery and drag at $M_\infty = 1\cdot82$ ($\theta_c = 22\cdot5$ deg).
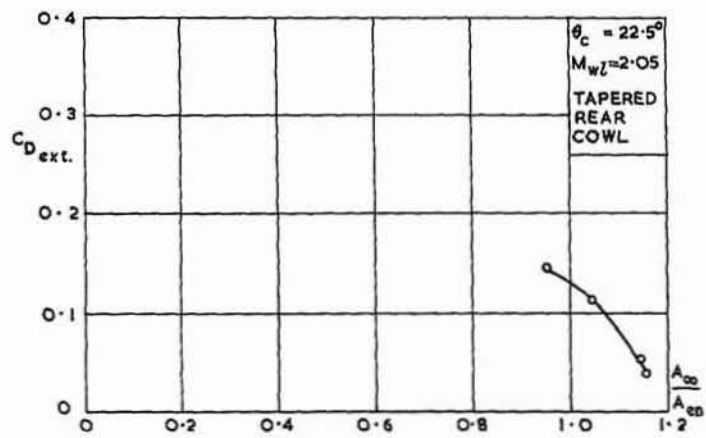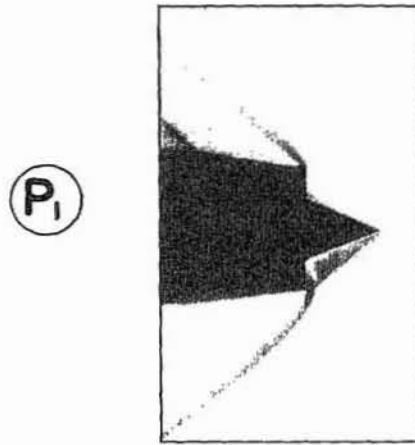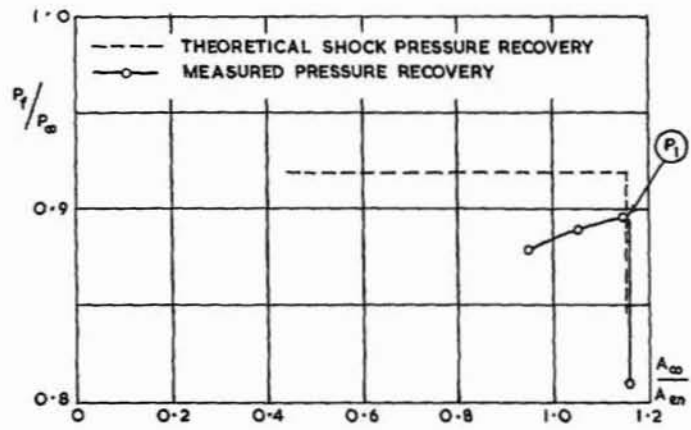
FIG. 49.   Pressure recovery and drag at $M_\infty = 1\cdot91$ ($\theta_c = 22\cdot5$ deg).
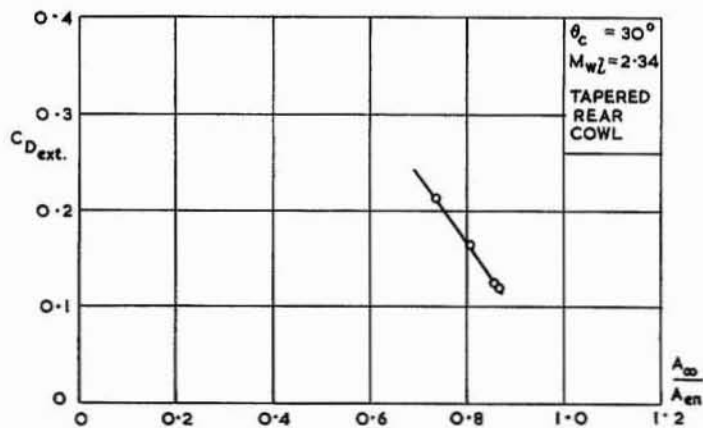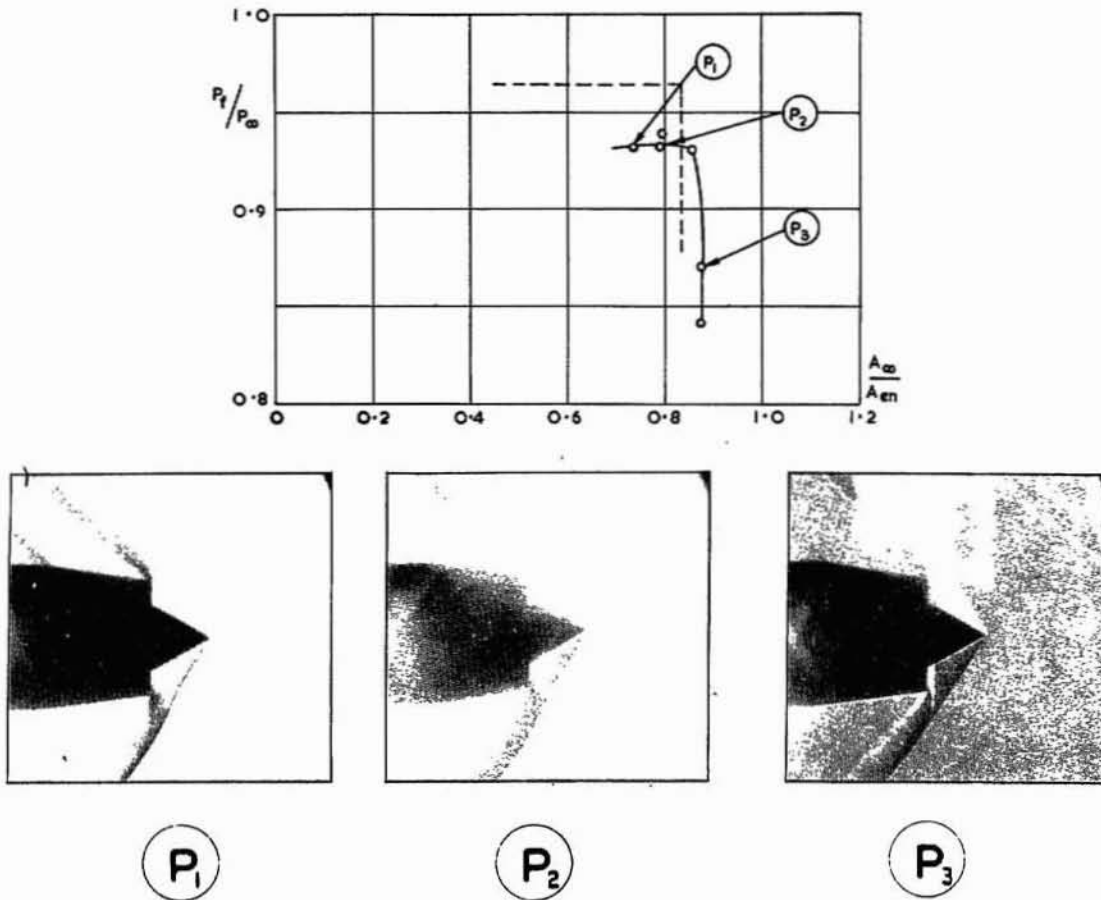
FIG. 50. Pressure recovery and drag at $M_\infty = 1 \cdot 61$ ($\theta_c = 30$ deg).
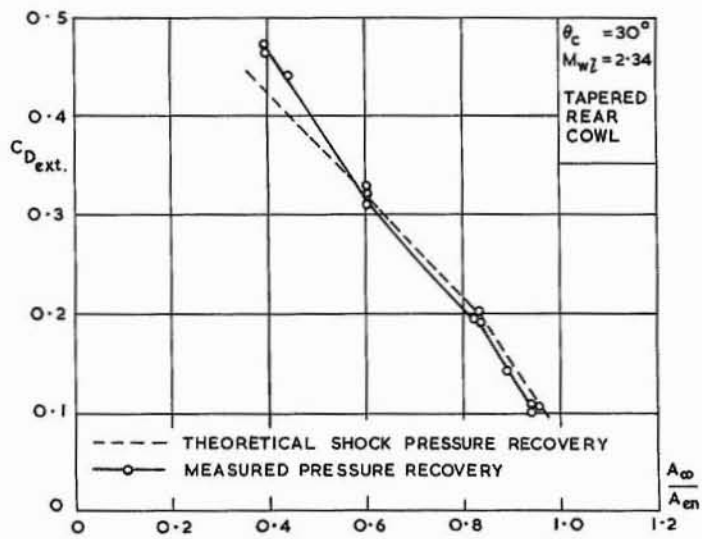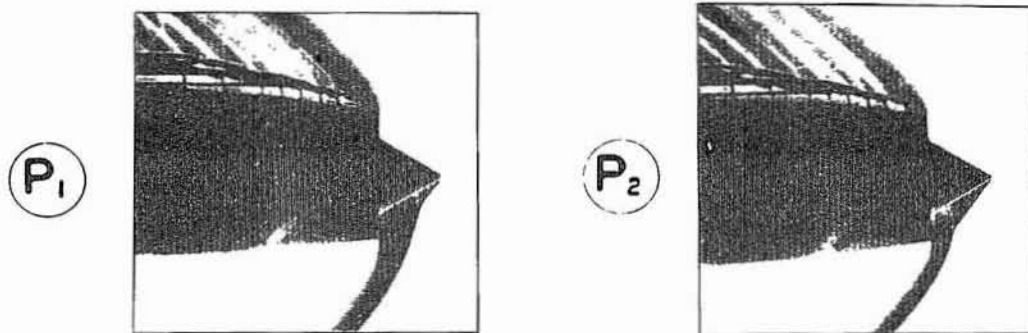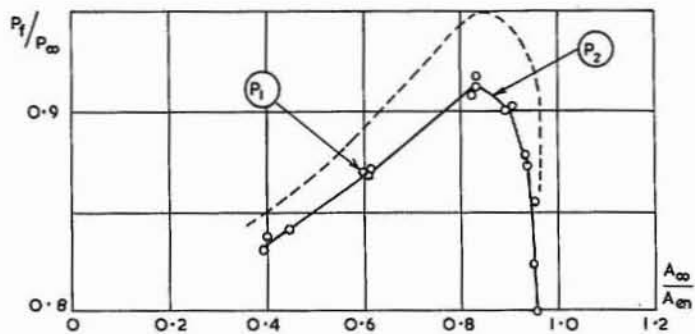
FIG. 51. Pressure recovery and drag at $M_\infty = 1\cdot82$ ($\theta_c = 30$ deg).
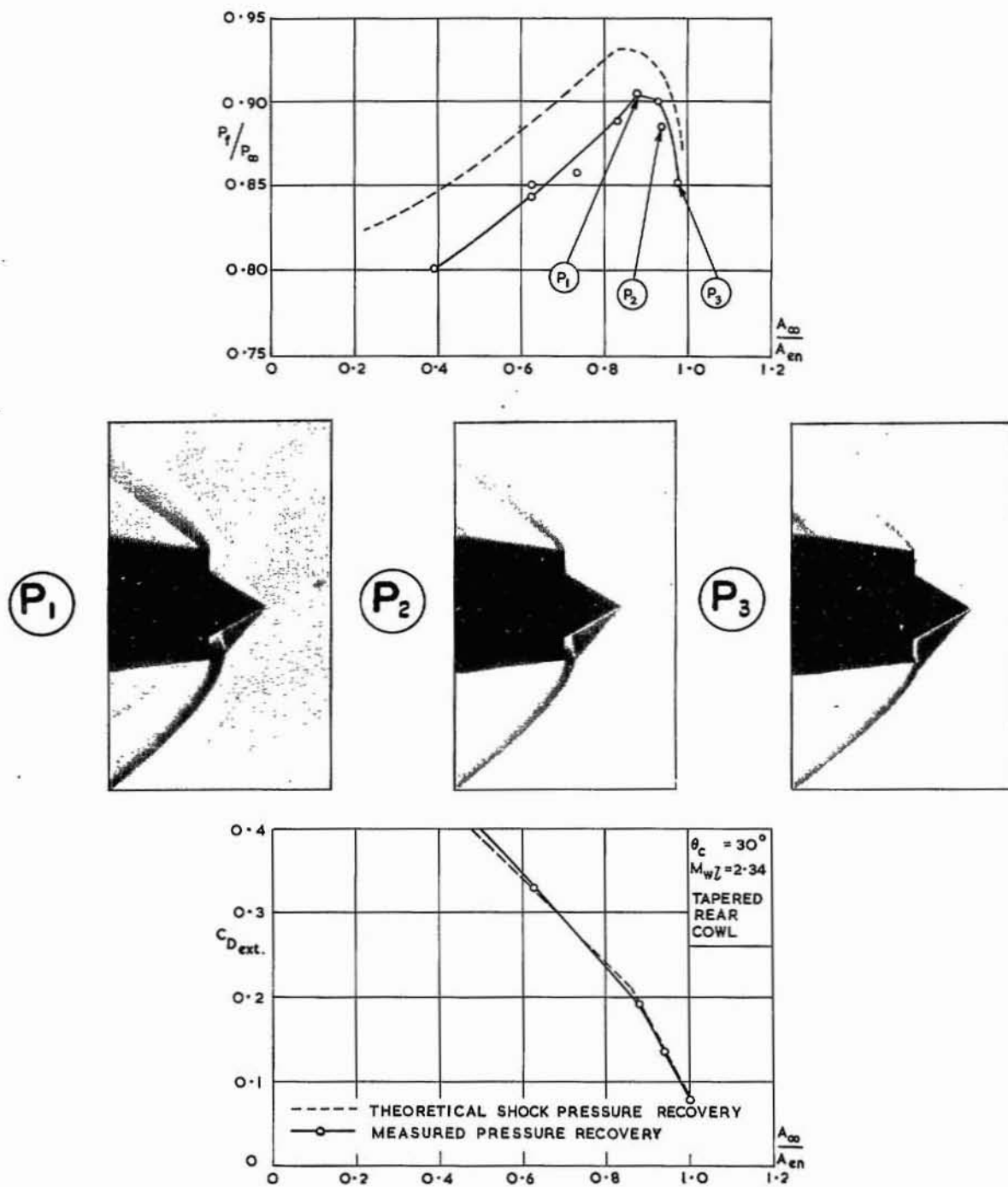
FIG. 52. Pressure recovery and drag at $M_\infty = 1\cdot91$ ($\theta_c = 30$ deg).
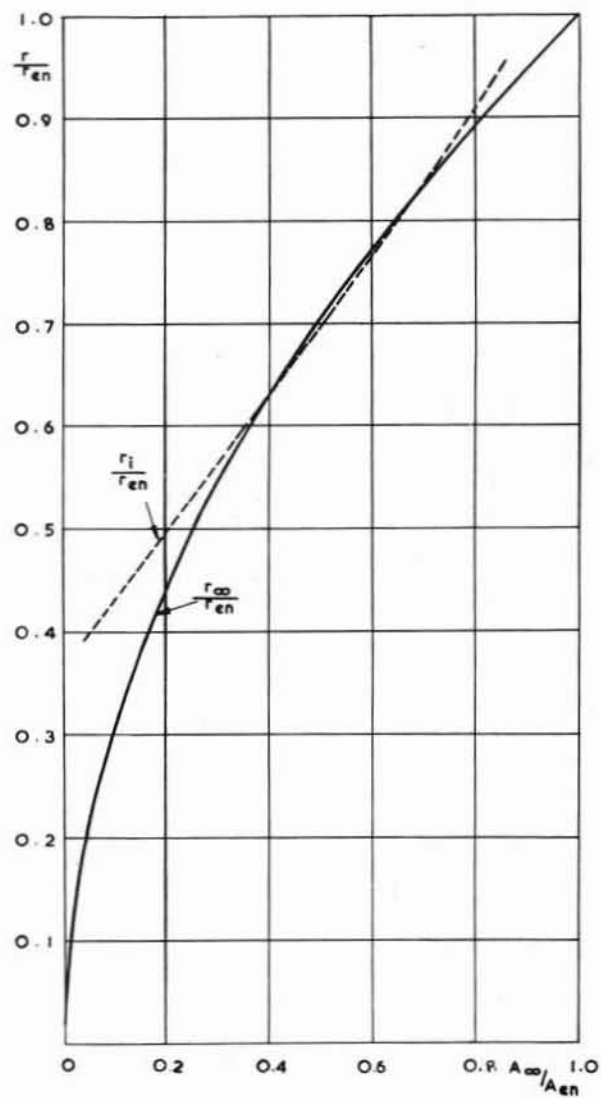
FIG. 54. Variation of r_i/r_{en} with relative mass flow for SD6 (− 0·05 in.) at $M_\infty = 2·48$.
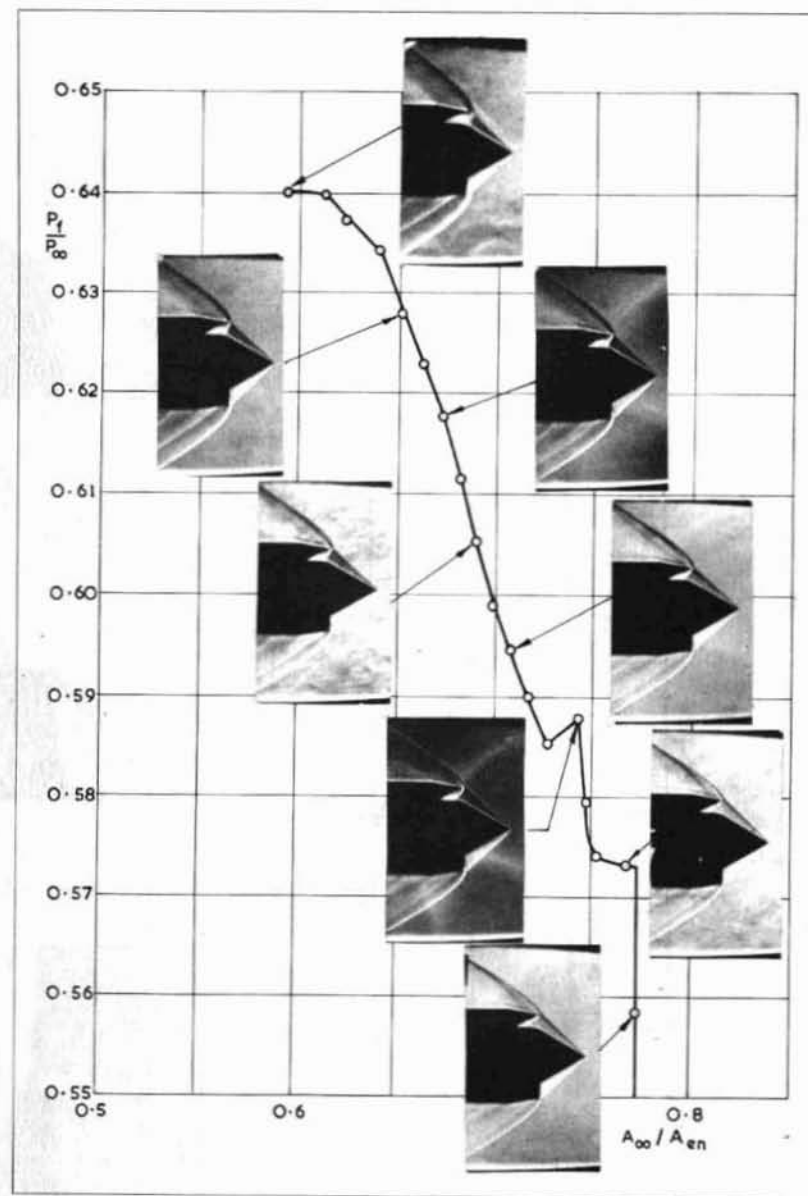
FIG. 53. Schlieren photographs of shock-boundary boundary-layer interaction on centre-body surface and associated pressure-recovery mass-flow curve.
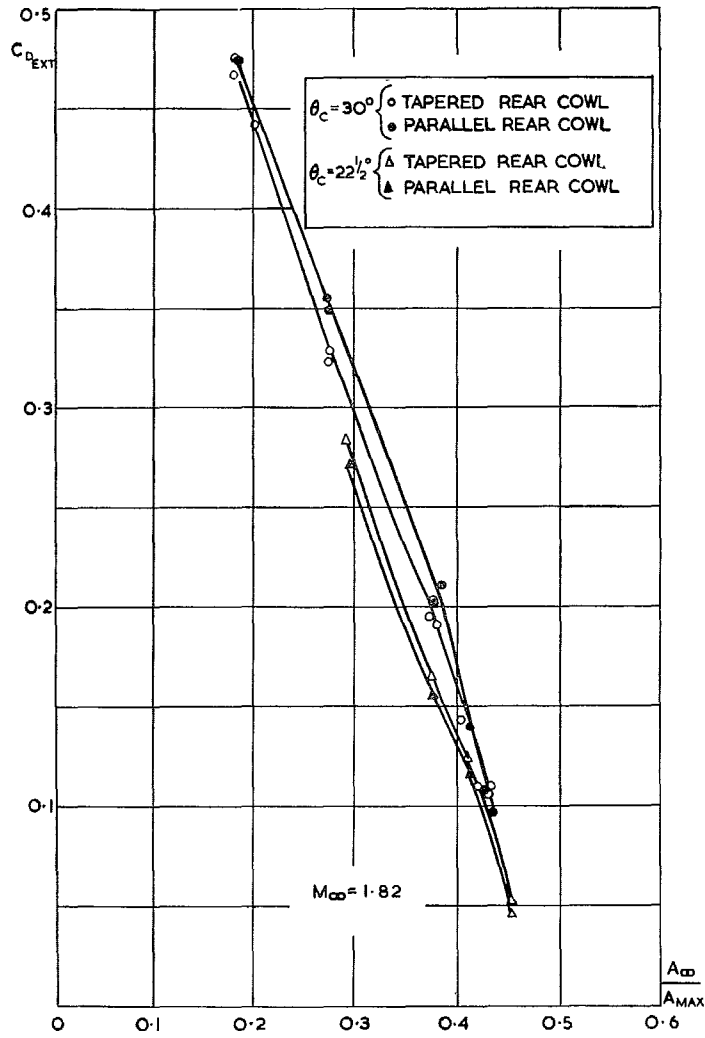
FIG. 55. Comparison of drags obtained with tapered and parallel rear cowls.

FIG. 56. Results of 3-shock-intersection calculations.
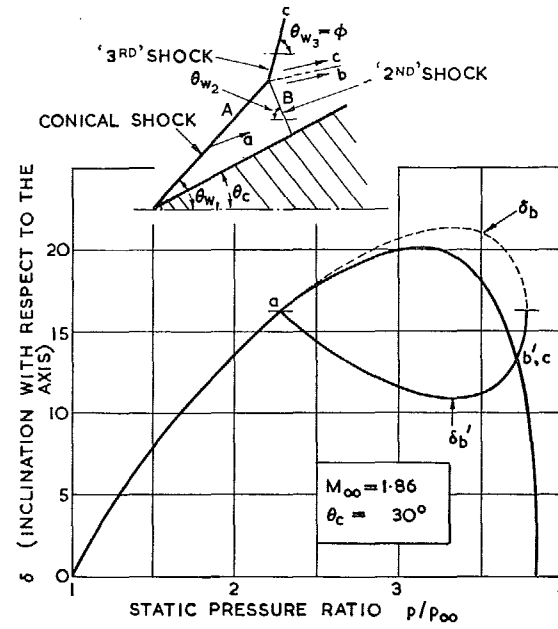
θ_c°	M_∞	$\theta_{w_1}^\circ$	$\theta_{w_2}^{\circ\,*}$	$\theta_{w_3}^\circ = \phi^*$
30	1·82	51·5	69·5	78·9
	1·86	50·6	65·8	80·8
	1·91	49·6	62·2	82·1
	2·14	46·2	51·5	86·3
	2·48	42·9	41·3	88·0
22·5	1·51	51·4	72·5	73·9
	1·61	47·9	59·8	80·5
	1·82	43·1	33·33	90·0
15	1·51	44·8	86·98	86·4

* NOTE:– THESE SHOCKS ARE SHOWN EXTENDING SOME WAY INTO THE FLOW FIELD. VALUES QUOTED ARE FOR THE ANGLE JUST AT THE INTERSECTION POINT.
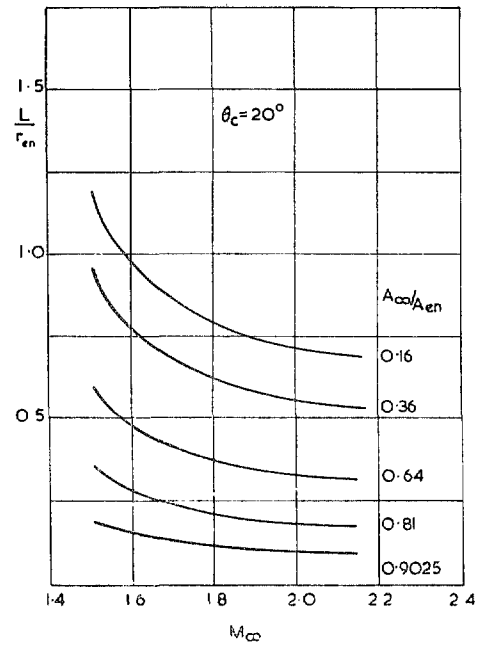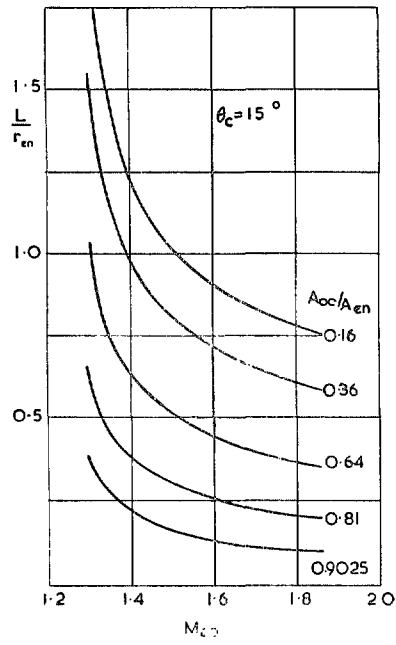
FIG. 62. L/r_{en} vs. M_∞ for $\theta_c = 15$ deg and 20 deg.
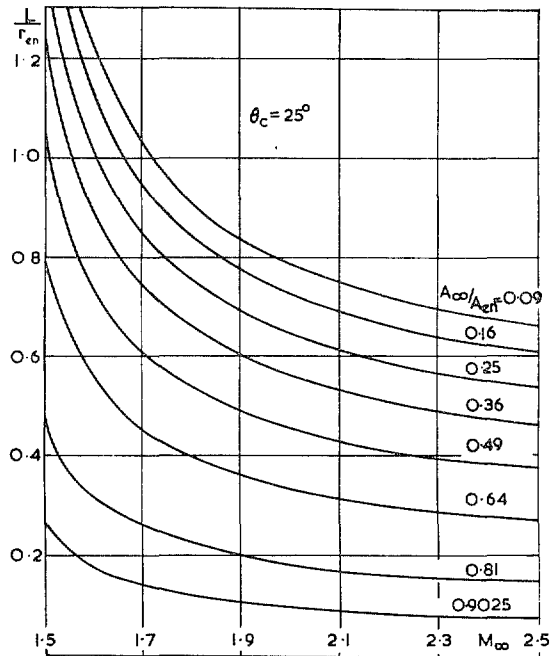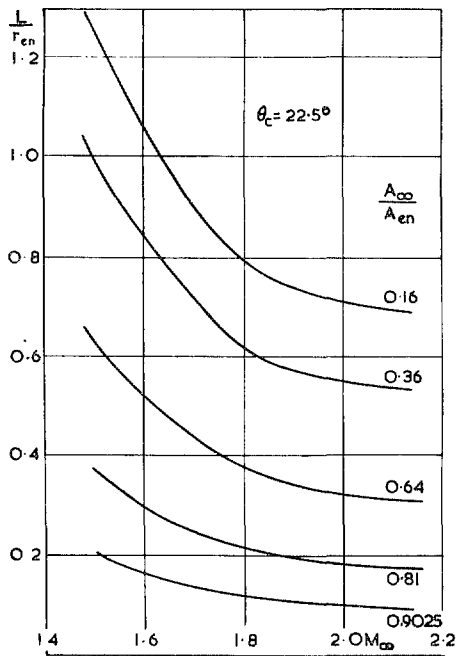
FIG. 63. L/r_{en} vs. M_∞ for $\theta_c = 22\cdot 5$ deg and 25 deg.
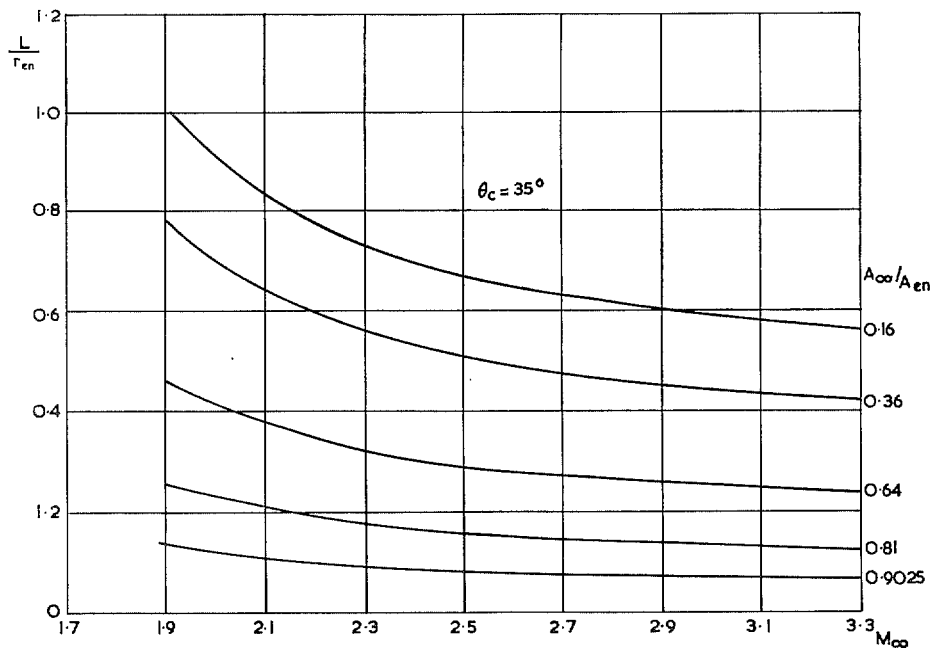
58
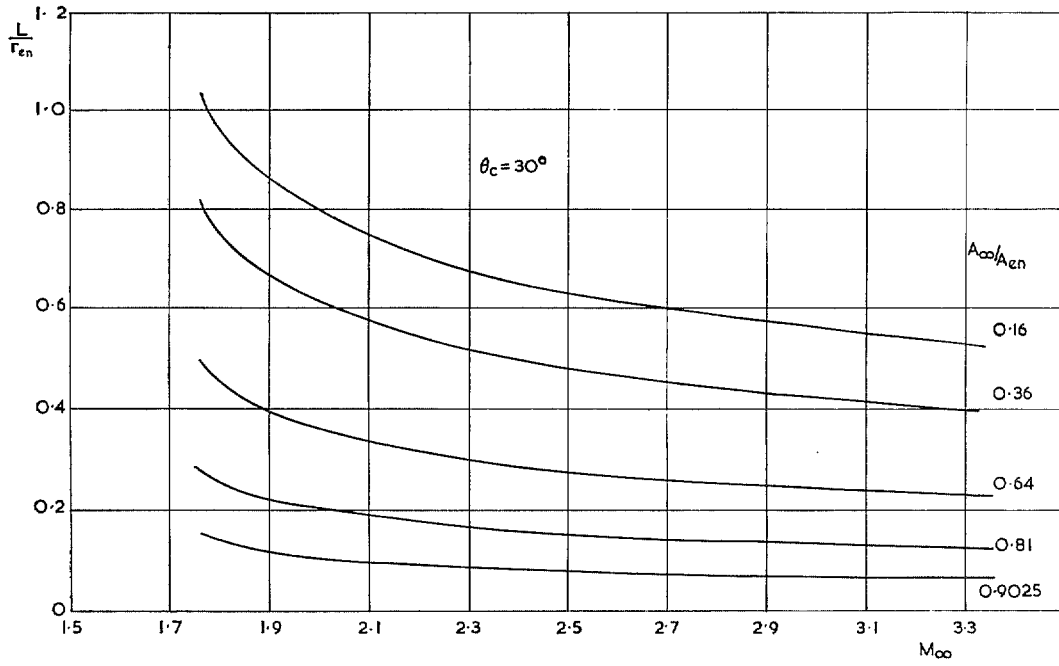
FIG. 64. L/r_{en} vs. M_∞ for $\theta_c = 30$ deg.

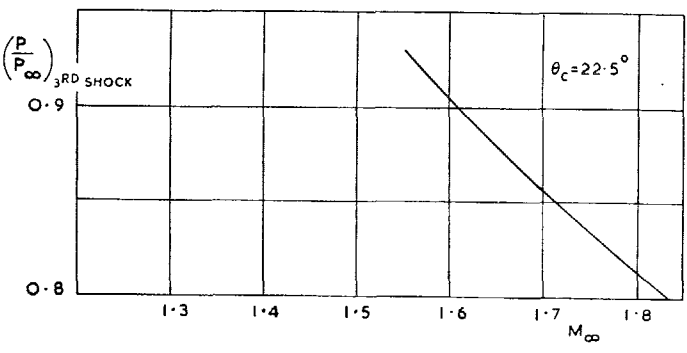FIG. 65. L/r_{en} vs. M_∞ for $\theta_c = 35$ deg.

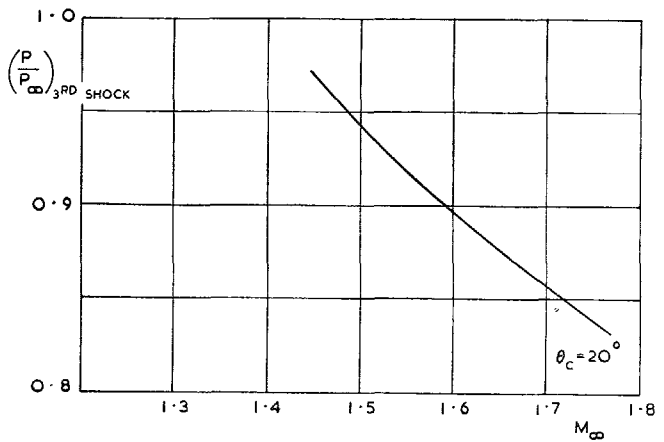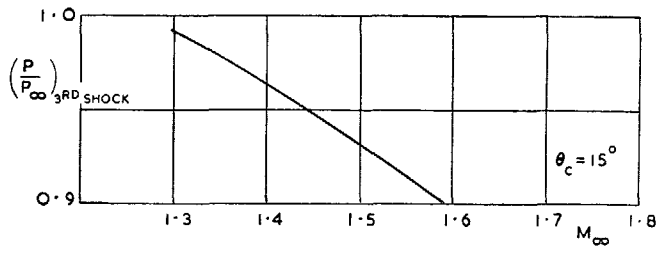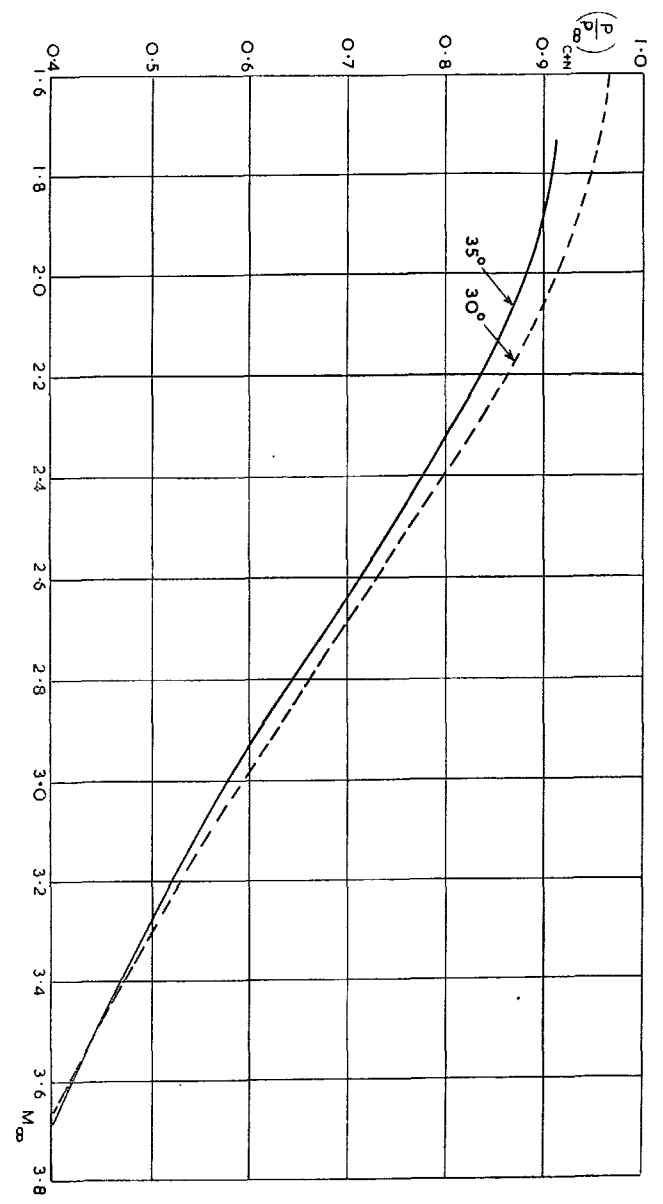FIG. 70. Pressure recovery through a cone shock followed by a normal shock
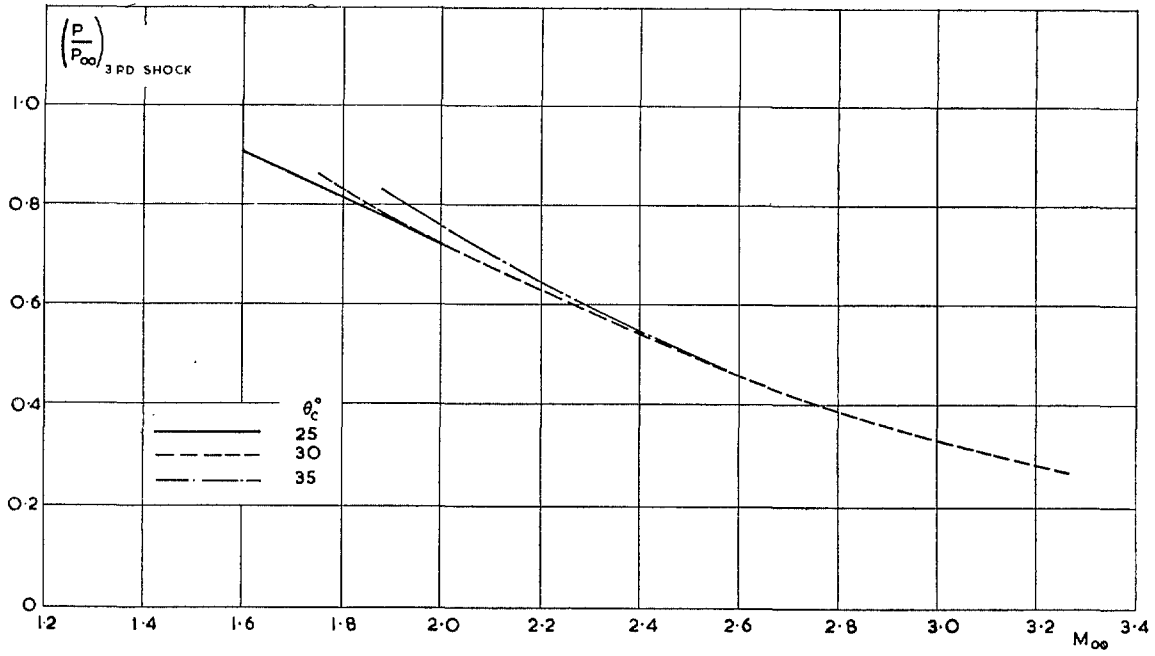$[(P/P_\infty)_{C+N}$ vs. M_c for $\theta_c = 30$ and 35 deg].

FIG. 71. Pressure recovery through the 'third' shock
$[(P/P_\infty)_{\text{3rd shock}}$ vs. M_c for $\theta_c = 15$, 20 and $22\cdot5$ deg].

FIG. 72. Pressure recovery through the 'third' shock
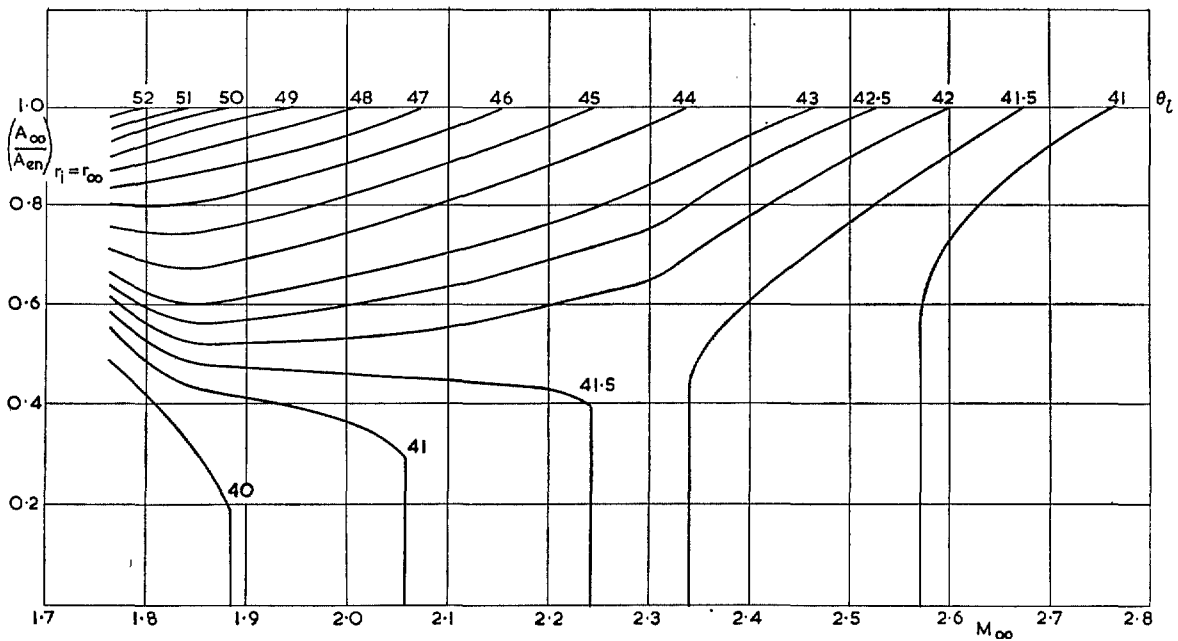[$(P/P_\infty)_{\text{3rd shock}}$ vs. M_∞ for $\theta_c = 25$, 30 and 35 deg].

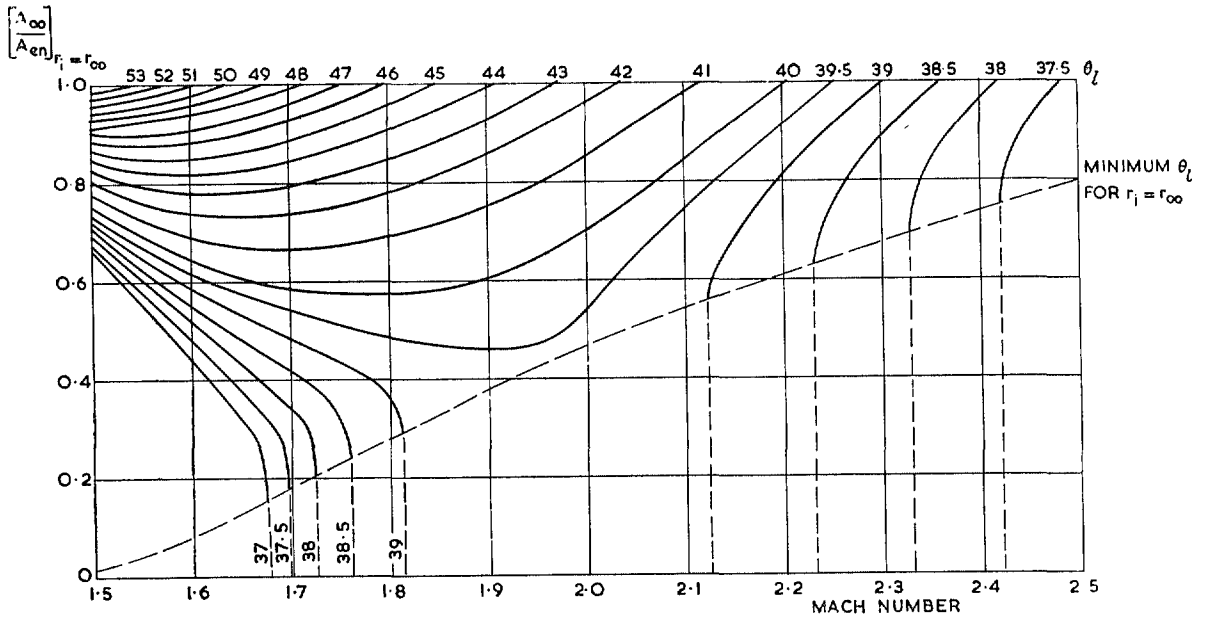FIG. 73. $(A_\infty/A_{en})_{r\,i\,=\,r\,\infty}$ vs. M_∞ for $\theta_c = 30$ deg.

63

FIG. 74. $(A_\infty/A_{en})_{r\,i\,=\,r\,\infty}$ vs. M_∞ for $\theta_c = 25$ deg.

FIG. 75. $(A_\infty/A_{en})_{r\,i\,=\,r\,\infty}$ vs. M_∞ for $\theta_c = 22\cdot5$ deg.

64

FIG. 76. $(A_\infty/A_{\infty\max})_{ri} = \infty$ vs. M_∞ for $\theta_c = 30$ deg.

FIG. 77. $(A_\infty/A_{\infty\max})_{ri} = r_\infty$ vs. M_∞ for $\theta_c = 25$ deg.
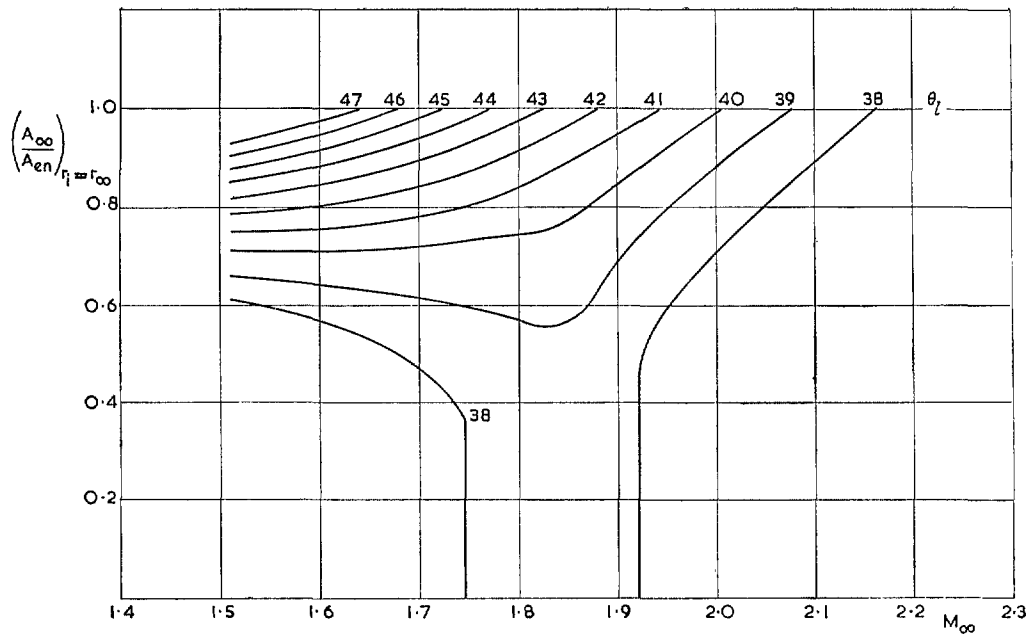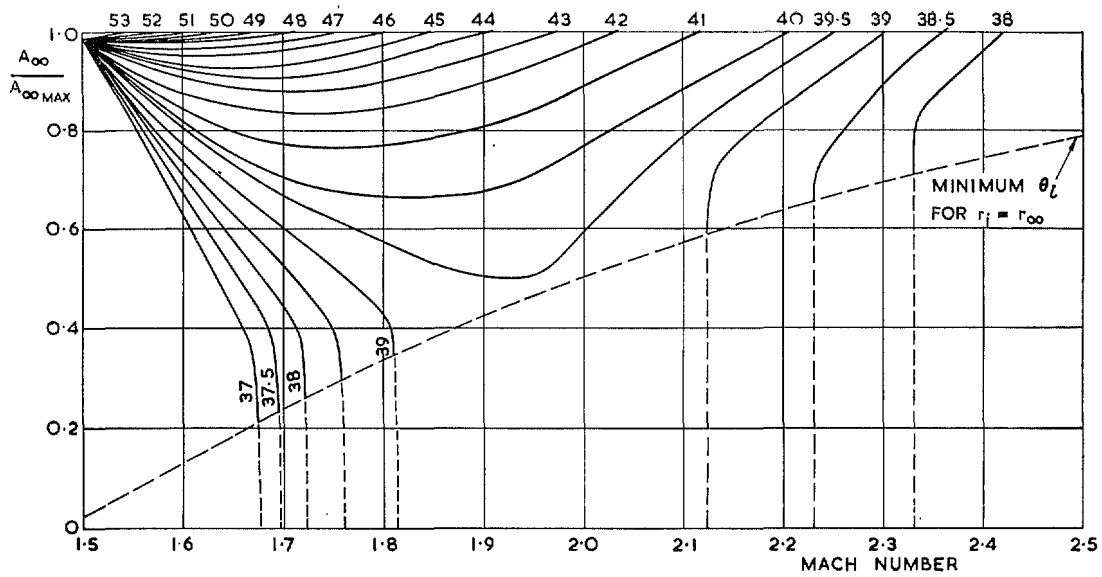
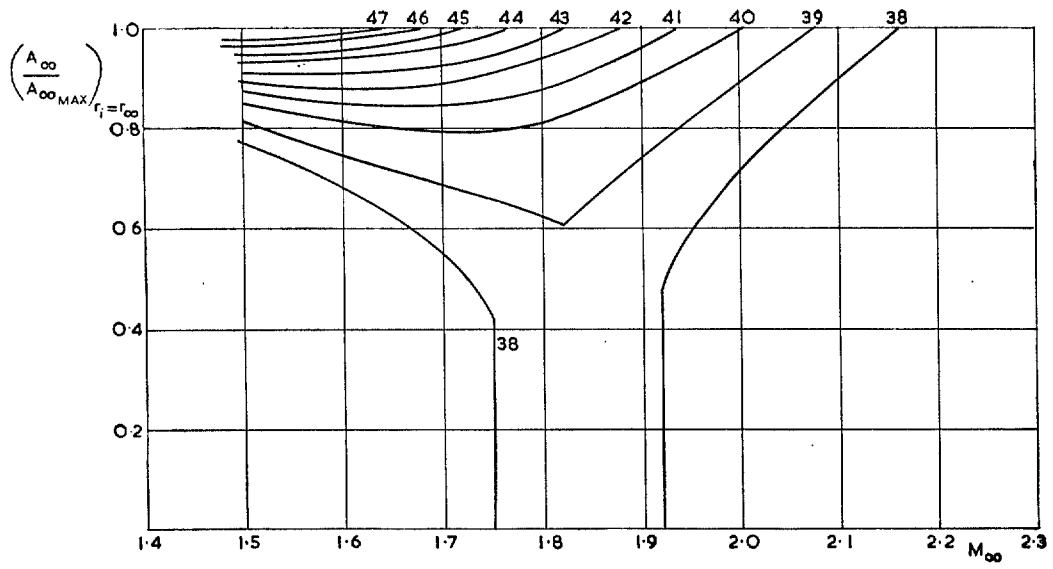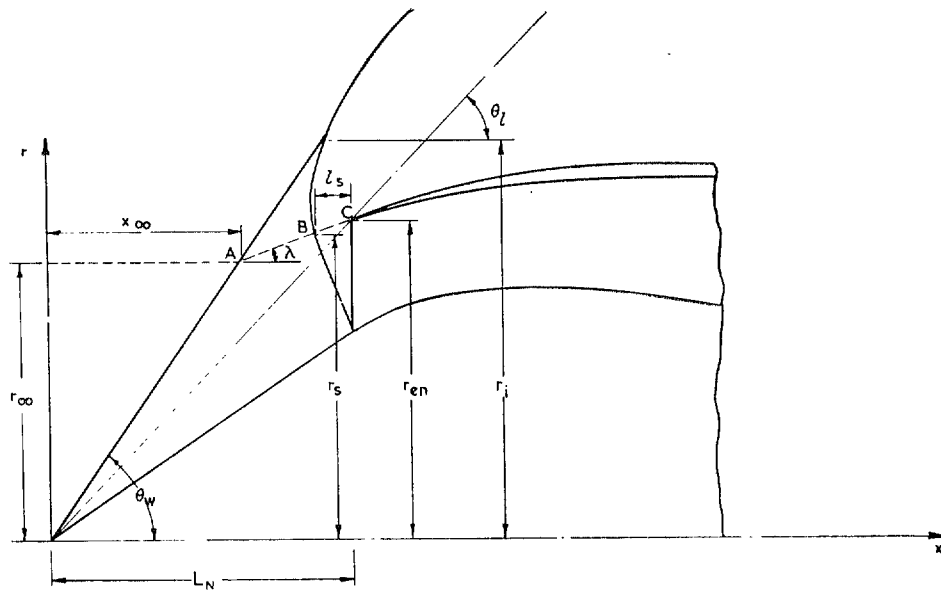FIG. 78. $(A_\infty/A_{\infty \, max})_{r\, i \, = \, r\, \infty}$ vs. M_∞ for $\theta_c = 22 \cdot 5$ deg.

FIG. 79. Notation for location of 'second' shock and calculation of drag (r_i always greater than r_∞).

Publication of the Aeronautical Research Council

ANNUAL TECHNICAL REPORTS OF THE AERONAUTICAL RESEARCH COUNCIL (BOUND VOLUMES)

1939 Vol.   I. Aerodynamics General, Performance, Airscrews, Engines.   50s. (52s.)
     Vol. II. Stability and Control, Flutter and Vibration, Instruments, Structures, Sea-
            planes, etc.   63s. (65s.)

1940 Aero and Hydrodynamics, Aerofoils, Airscrews, Engines, Flutter, Icing, Stability and
            Control Structures, and a miscellaneous section.   50s. (52s.)

1941 Aero and Hydrodynamics, Aerofoils, Airscrews, Engines, Flutter, Stability and Con-
            trol Structures.   63s. (65s.)

1942 Vol.   I. Aero and Hydrodynamics, Aerofoils, Airscrews, Engines.   75s. (77s.)
     Vol. II. Noise, Parachutes, Stability and Control, Structures, Vibration, Wind
            Tunnels.   47s. 6d. (49s. 6d.)

1943 Vol.   I. Aerodynamics, Aerofoils, Airscrews.   80s. (82s.)
     Vol. II. Engines, Flutter, Materials, Parachutes, Performance, Stability and Con-
            trol, Structures.   90s. (92s. 9d.)

1944 Vol.   I. Aero and Hydrodynamics, Aerofoils, Aircraft, Airscrews, Controls.   84s.
            (86s. 6d.)
     Vol. II. Flutter and Vibration, Materials, Miscellaneous, Navigation, Parachutes,
            Performance, Plates and Panels, Stability, Structures, Test Equipment,
            Wind Tunnels.   84s. (86s. 6d.)

1945 Vol.   I. Aero and Hydrodynamics, Aerofoils.   130s. (132s. 9d.)
     Vol. II. Aircraft, Airscrews, Controls.   130s. (132s. 9d.)
     Vol. III. Flutter and Vibration, Instruments, Miscellaneous, Parachutes, Plates and
            Panels, Propulsion.   130s. (132s. 6d.)
     Vol. IV. Stability, Structures, Wind Tunnels, Wind Tunnel Technique.   130s.
            (132s. 6d.)

Annual Reports of the Aeronautical Research Council—

      1937   2s. (2s. 2d.)   1938   1s. 6d. (1s. 8d.)   1939–48   3s. (3s. 5d.)

Index to all Reports and Memoranda published in the Annual Technical Reports, and separately—

     April, 1950   -   -   -   -   R. & M. 2600   2s. 6d. (2s. 10d.)

Author Index to all Reports and Memoranda of the Aeronautical Research Council—

     1909—January, 1954   R. & M. No. 2570   15s. (15s. 8d.)

Indexes to the Technical Reports of the Aeronautical Research Council—

     December 1, 1936—June 30, 1939   R. & M. No. 1850   1s. 3d. (1s. 5d.)
     July 1, 1939–June 30, 1945   R. & M. No. 1950   1s. (1s. 2d.)
     July 1, 1945—June 30, 1946   R. & M. No. 2050   1s. (1s. 2d.)
     July 1, 1946—December 31, 1946   R. & M. No. 2150   1s. 3d. (1s. 5d.)
     January 1, 1947—June 30, 1947   R. & M. No. 2250   1s. 3d. (1s. 5d.)

Published Reports and Memoranda of the Aeronautical Research Council—

     Between Nos. 2251–2349   R. & M. No. 2350   1s. 9d. (1s. 11d.)
     Between Nos. 2351–2449   R. & M. No. 2450   2s. (2s. 2d.)
     Between Nos. 2451–2549   R. & M. No. 2550   2s. 6d. (2s. 10d.)
     Between Nos. 2551–2649   R. & M. No. 2650   2s. 6d. (2s. 10d.)
     Between Nos. 2651–2749   R. & M. No. 2750   2s. 6d. (2s. 10d.)

Prices in brackets include postage

HER MAJESTY'S STATIONERY OFFICE